



Pretargeting in nuclear imaging and radionuclide therapy

Improving efficacy of theranostics and nanomedicines

Stéen, E Johanna L; Edem, Patricia E; Nørregaard, Kamilla; Jørgensen, Jesper T; Shalgunov, Vladimir; Kjaer, Andreas; Herth, Matthias M

Published in:
Biomaterials

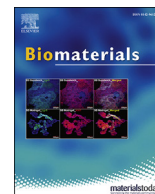
DOI:
[10.1016/j.biomaterials.2018.06.021](https://doi.org/10.1016/j.biomaterials.2018.06.021)

Publication date:
2018

Document version
Publisher's PDF, also known as Version of record

Document license:
[CC BY-NC-ND](https://creativecommons.org/licenses/by-nc-nd/4.0/)

Citation for published version (APA):
Stéen, E. J. L., Edem, P. E., Nørregaard, K., Jørgensen, J. T., Shalgunov, V., Kjaer, A., & Herth, M. M. (2018). Pretargeting in nuclear imaging and radionuclide therapy: Improving efficacy of theranostics and nanomedicines. *Biomaterials*, 179, 209-245. <https://doi.org/10.1016/j.biomaterials.2018.06.021>



Pretargeting in nuclear imaging and radionuclide therapy: Improving efficacy of theranostics and nanomedicines

E. Johanna L. Stéen^{a, b}, Patricia E. Edem^{a, b, c}, Kamilla Nørregaard^{b, c},
Jesper T. Jørgensen^{b, c}, Vladimir Shalgunov^a, Andreas Kjaer^{b, c}, Matthias M. Herth^{a, b, *}

^a Department of Drug Design and Pharmacology, Faculty of Health and Medical Sciences, University of Copenhagen, Jagtvej 160, DK-2100 Copenhagen, Denmark

^b Department of Clinical Physiology, Nuclear Medicine & PET, Rigshospitalet, Blegdamsvej 9, DK-2100 Copenhagen, Denmark

^c Cluster for Molecular Imaging, Department of Biomedical Sciences, University of Copenhagen, Blegdamsvej 3, DK-2100 Copenhagen, Denmark

ARTICLE INFO

Article history:

Received 1 April 2018

Received in revised form

13 June 2018

Accepted 14 June 2018

Available online 22 June 2018

Keywords:

Pretargeted imaging

Pretargeted radionuclide therapy

EPR effect

Nanomedicines

Bispecific antibody and hapten recognition

(strept)avidin–biotin interaction

Hybridization of complementary

oligonucleotides

SPAAC

Tetrazine ligation

ABSTRACT

Pretargeted nuclear imaging and radiotherapy have recently attracted increasing attention for diagnosis and treatment of cancer with nanomedicines. This is because it conceptually offers better imaging contrast and therapeutic efficiency while reducing the dose to radiosensitive tissues compared to conventional strategies. In conventional imaging and radiotherapy, a directly radiolabeled nano-sized vector is administered and allowed to accumulate in the tumor, typically on a timescale of several days. In contrast, pretargeting is based on a two-step approach. First, a tumor-accumulating vector carrying a tag is administered followed by injection of a fast clearing radiolabeled agent that rapidly recognizes the tag of the tumor-bound vector *in vivo*. Therefore, pretargeting circumvents the use of long-lived radionuclides that is a necessity for sufficient tumor accumulation and target-to-background ratios using conventional approaches.

In this review, we give an overview of recent advances in pretargeted imaging strategies. We will critically reflect on the advantages and disadvantages of current state-of-the-art conventional imaging approaches and compare them to pretargeted strategies. We will discuss the pretargeted imaging concept and the involved chemistry. Finally, we will discuss the steps forward in respect to clinical translation, and how pretargeted strategies could be applied to improve state-of-the-art radiotherapeutic approaches.

© 2018 The Authors. Published by Elsevier Ltd. This is an open access article under the CC BY-NC-ND license (<http://creativecommons.org/licenses/by-nc-nd/4.0/>).

1. Introduction

1.1. Nanomedicines in modern medicine

The emergence of nanomedicines for use in the treatment of cancer has been rapidly increasing over the past decades since their application has great potential to improve current cancer diagnosis and therapy. In general, a wide range of materials ranging from inorganic particles to proteins and organic structures such as polymers and liposomes can be used as nanomedicines. In this review, nanomedicines are defined as nano-sized targeting vectors that accumulate via passive targeting into tumors (Fig. 1) [1,2]. The mode of action for these nanomedicines can vary widely. Some nanomedicines have been designed to act as therapeutics

themselves, e.g. as thermal agents in photothermal therapy [3,4], others have been developed to be used as drug carriers [5–7]. These carriers have great promise in delivering and releasing chemotherapeutics more selectively to tumors [5,6,8]. For example, liposomal encapsulated chemotherapeutic drug formulations (e.g. Doxil (liposomal doxorubicin), MM-302 (HER2 antibody-targeted liposomal doxorubicin) or MM-398 (nanoliposomal irinotecan) are three examples of such delivery systems [9–11].

1.2. The enhanced permeability and retention effect

The enhanced permeability and retention (EPR) effect is responsible for the passive accumulation of nanomedicines into tumor tissue [12]. The effect is a result of the rapid and abnormal growth of tumor blood vessels, which leads to increased fenestrations between cells and poor lymphatic drainage. These circumstances enable nanomedicines to extravasate from the blood pool into the tumor tissue and being retained there (Fig. 1B) [13–15].

* Corresponding author. Jagtvej 160, DK-2100 Copenhagen, Denmark.
E-mail address: matthias.herth@sund.ku.dk (M.M. Herth).

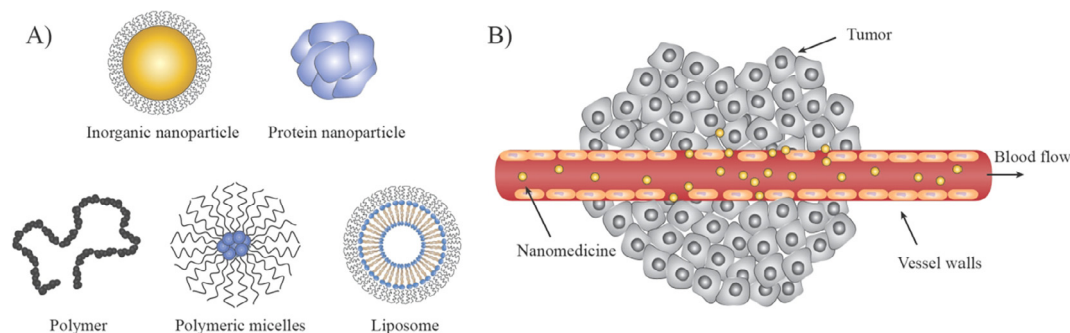


Fig. 1. (A) Schematic illustration of different types of nanomedicines used in modern medicine. The inorganic nanoparticle and liposome is shown with a poly (ethylene glycol) (PEG) layer that is used in vivo to increase circulation time. (B) The EPR effect: Leaky vasculature and impaired lymphatic drainage allows nanomedicines in the blood to extravasate into the tumor microenvironment.

Overall, prolonging circulation time in the blood increases the likelihood of tumor accumulation via the EPR effect, simply because more nanomedicines pass through the leaky tumor vasculature over time.

Tumor accumulation via EPR is, among other things, dependent on the physicochemical characteristics of the nanomedicine itself. In particular the size, surface properties, shape and charge can alter accumulation [5,16]. Besides matching the gap sizes of the leaky tumor vessels, the dimensions of the nanomedicine should also be such that early clearance from the blood is avoided [17,18]. To prevent renal excretion, nanomedicines should typically be larger than ~6 nm. On the other hand, nanomedicines larger than ~200 nm are rapidly recognized and sequestered by the reticulo-endothelial system (RES) (mainly consisting of the liver and the spleen). Furthermore, the surface of the nanomedicine has also an influence on RES recognition. Neutrally charged nanomedicines tend to be better shielded from recognition and therefore have longer circulation times. A common strategy to prevent RES recognition of nanomedicines is shielding them from RES-facilitating proteins (opsonins) by decorating the surface with neutralizing molecules such as poly(ethylene glycol) (PEG) [17].

The tumor microenvironment can also affect the accumulation of passively targeting nanomedicines [8,19]. For example, the vascular density is commonly unevenly distributed throughout solid tumors with the highest abundance in the periphery at the host interface and lowest in hypoxic and adjacent necrotic regions. Abnormal vessel structure causes irregular blood flow within tumors and impaired lymphatic drainage can lead to high interstitial pressure gradients in the tumor microenvironment. Moreover, the gap sizes in the vessel walls are commonly heterogeneous distributed throughout the tumor [15,20]. Therefore, it is not surprising that the EPR effect is strongly affected by the tumor microenvironment and consequently, the accumulation of passively targeting nanomedicines is variable.

So far, no clear relationship between tumor type, size or stage and EPR has been established neither in animal models nor in cancer patients [21–23]. In fact, considerable variations in tumor uptake of radiolabeled liposomes between different tumor types and even between patients with the same tumor type have been observed [9,10,24].

1.3. Personalized medicine

Personalized medicine, where medical decisions, practices, and/or products are being tailored to the individual patient, is a concept based on the application of companion diagnostics. It is used to identify which patients will likely benefit from a particular therapy, or conversely and often as important, which patients are likely non-

responders and should receive a different treatment strategy (Fig. 2A).

In general, patient to patient variations in EPR-mediated tumor uptake represents a challenge for the overall application of passively accumulating nanomedicines. However, accumulation of up to 50% injected dose per kg (ID/kg) has been observed in patients¹ [24] and as such, the application of nanomedicines is still promising for clinical use. Therefore, screening methods with the ability to select patients that would benefit from EPR based treatment strategies would be of great value. Diagnostic imaging with Positron Emission Tomography (PET) or Single Photon Emission Computed Tomography (SPECT) are routinely used in the clinic for identification of patient cohorts and monitoring of treatment response [25,26]. This is because PET and SPECT are highly sensitive (the level of detection approaches 10^{-12} M of tracer) and offer isotropism (i.e. ability to detect organ accumulation accurately, regardless of tissue depth) [27]. Furthermore, with PET, it is possible to get a quantitative measure for the amount of nanomedicine delivered to the tumor, making this modality especially suited for personalized medicine [28].

In 2017, Lee and colleagues published the first PET study quantifying the variability of the EPR-mediated accumulation of nanomedicines in relation to the treatment response in patients with metastatic breast cancer [9]. In this study, the treatment response of human epidermal growth factor 2 (HER2)-targeted liposomal doxorubicin (MM-302) correlated positively with the extent of EPR-mediated uptake of ⁶⁴Cu-MM-302 (Fig. 2B). Similarly, Perez-Medina et al. reported a correlation between uptake of a⁸⁹Zr-labeled PEGylated liposome and the effect of Doxil, liposome encapsulated doxorubicin, on tumor growth in a xenograft model of breast cancer [29,30].

1.4. Imaging of nanomedicines during the drug development process

Considering the increasing amount of knowledge in the area of drug delivery and the number of novel nanomedicines that are continuously being developed, only a few compounds make it into clinical trials. In fact, in a recent publication surveying the literature from 2005 until 2015, it was found that there has been no improvement in the median accumulation of nanomedicines within this time

¹ In comparison, monoclonal antibodies typically show ID/kg around the same magnitude as nanomedicines do (0.001%–0.01% of the injected dose per gram of tumor [Goldenberg, D. M., Cancer imaging with radiolabeled antibodies, Kluwer Academic Publishers 1990, ISBN: 978-0-7923-0631-3] [Scott et al., Nat Rev Cancer, 2012, 12:278–87] [Maccucci F. et al., MABs, 2013, 5: 34–46].

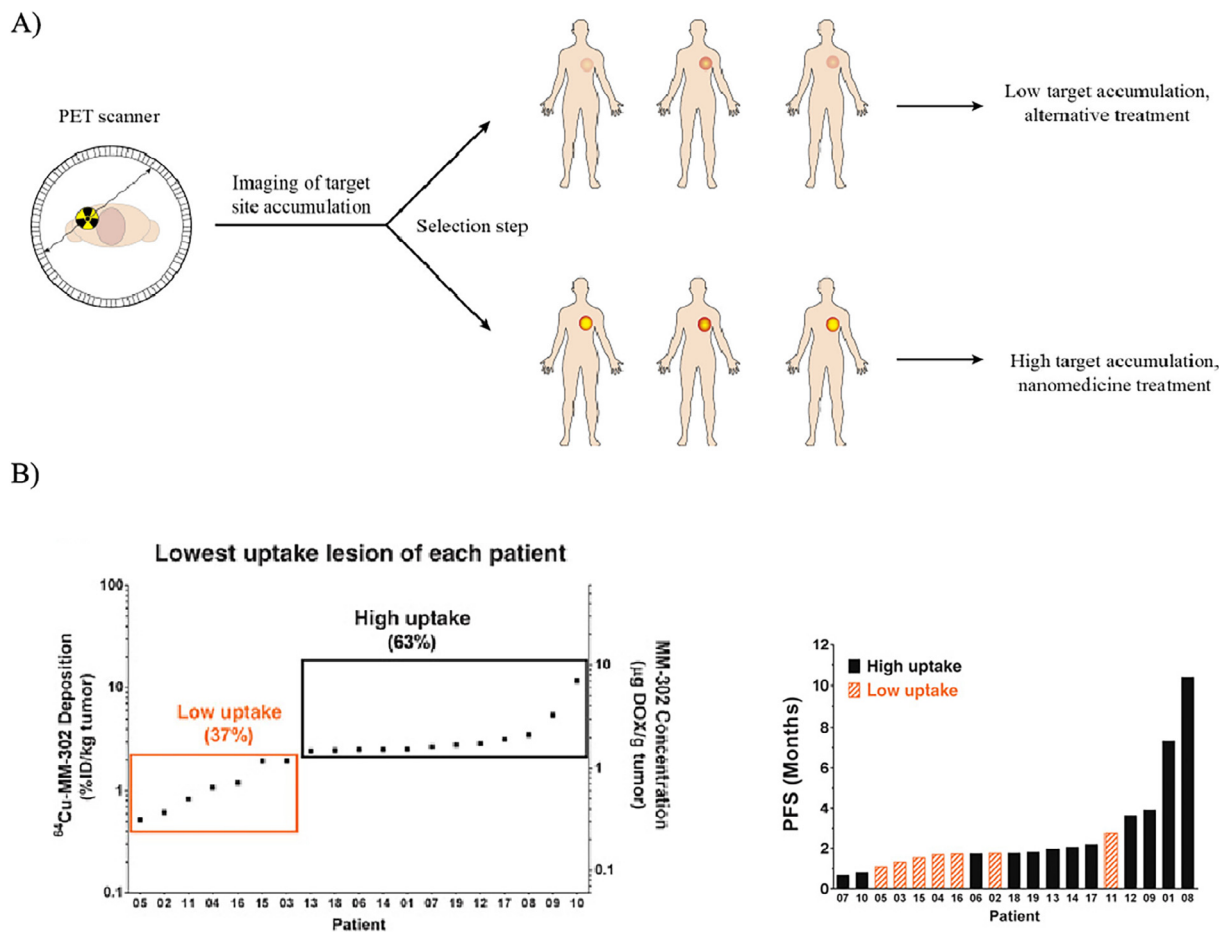


Fig. 2. Personalized medicine. (A) As a general principle, patients are prescreened, e.g. using PET imaging, prior to therapy with a radiolabeled version of the nanomedicine formulation (selection step). This allows identifying individuals showing sufficiently high target accumulation that are more likely to respond to treatment with the nanomedicine formulation whereas patients with low target accumulation should receive or be changed to an alternative treatment strategy. (B) Correlation between EPR effect and treatment: ^{64}Cu -MM-302 deposition uptake lesions are shown for individual patients. A threshold was selected to divide patients into "low uptake" patients and "high uptake" (left). Median progression-free survival (PFS) of the patients is shown. "High uptake" patients have a higher probability to be sensitive to treatment with MM-302 (right). The accumulation profile of MM-302 is independent of the targeting ligand, hence dictated primarily by the EPR effect. Figure modified from Ref. [9].

frame (0.7% of the administered dose) [31]. Lammers and colleagues identified several pitfalls that could lead to the observed statistics: I) overinterpretation of the EPR effect, II) poor tumor and tissue penetration of nanomedicines, III) misunderstanding of the potential usefulness of active drug targeting, IV) irrational formulation design, V) lack of proper animal models, which are physiologically more relevant and predictive for the clinical situation,² and VI) insufficient integration of non-invasive imaging techniques [5].

The possibility to use nuclear imaging techniques to quantify the EPR effect on an individual basis and thereby select patient groups likely to respond to nanomedicines has been discussed in the previous section (see 1.3, Personalized medicine). However, nuclear imaging techniques can also be used during drug development. It can be applied to study the biodistribution of nanomedicines, to quantify drug release, to find the optimal dose within clinical trials and to assess the therapeutic efficacy in real-time [5,29,32]. For instance, nuclear imaging has been used to study the circulation

time of liposomes and to identify which liposome has the highest potential to be used for passive drug delivery [24]. In vivo biodistribution studies can also efficiently show if the respective nanomedicine is being deposited in tissues that could result in toxicological concerns. A prominent example, which shows that nuclear imaging should be included early in nanomedicine drug development, is the study published by Seymour and colleagues [33]. They studied the biodistribution of *N*-(2-Hydroxypropyl) methacrylamide (HPMA) copolymer-bound doxorubicin (PK2) in 31 patients with primary or metastatic liver cancer. In phase I/II clinical trials, they found that the treatment efficacy was low. Detailed imaging analysis revealed retrospectively that PK2 targets healthy liver tissue rather than the tumor. Earlier implementation of this study could have prevented expensive phase I/II trials.

2. State of the art labeling strategies for non-targeted nanomedicinal drug delivery systems

2.1. Pharmacokinetics of nanomedicines and the choice of radionuclide for imaging

In order to conduct PET or SPECT imaging of long-circulating nanomedicines, suitable radionuclides have to be attached to the corresponding structure (see section 2.2). Table 1 summarizes key

² The EPR effect is generally rather high in most small animal tumor models compared to patient tumors. This leads to discrepancies in efficacy between pre-clinical and clinical trials [Shi J et al., Nat. Rev. Cancer, 2017, 17: 20–37] [Lammers T et al., J Control Release, 2012, 161: 175–187].

properties of radionuclides used for PET and SPECT imaging. The most commonly used PET and SPECT radionuclides such as carbon-11 (20.4 min), fluorine-18 (110 min) and technetium-99m (6.01 h) have rather short half-lives, ranging from minutes to a couple of hours (see Table 1). However, these half-lives are too short to be compatible with the slow pharmacokinetics of nanomedicines, as accumulation at the tumor-site via the EPR effect usually takes several days [9,24,34–36]. This necessitates the use of radionuclides with longer half-lives e.g. indium-111 (2.8 days), zirconium-89 (3.3 days) or iodine-124 (4.2 days).

Although both PET and SPECT radionuclides can be used to image the pharmacokinetic properties of nanomedicines [37], clinical PET cameras typically have greater sensitivity and higher spatial and temporal resolution than clinical SPECT cameras [38,39]. Therefore, PET imaging offers better image quality at lower injected radioactivity doses. In contrast to SPECT, PET measurements are quantitative, which makes PET the preferred imaging method in clinical settings if a suitable labeling strategy exists.

2.2. Conventional strategies for nanomedicines radiolabeling

Numerous methods for the labeling of nanomedicines have been reported [52–56]. In general, they fall into two categories, namely surface labeling and core labeling (Table 2).

1) Surface labeling

Classically, nanomedicines are radiolabeled by attaching a radionuclide onto their surface [57,58]. This type of surface labeling can be further divided into two broad categories, direct and indirect labeling (Table 2A). In direct labeling, the radionuclide is incorporated or attached to the nanomedicine of interest without any additional reaction steps. Not all nanomedicines can efficiently be labeled using this direct approach. For example, some radiolabeling reactions require harsh conditions (e.g. high temperatures and strong bases), that the nanomedicine cannot withstand. In such cases, the radionuclide can be introduced via an indirect labeling strategy. In indirect labeling, the radionuclide is first introduced into a smaller synthon called a prosthetic group, which is thereafter attached to the nanomedicine of interest. This approach is much

more versatile than direct labeling since the prosthetic group can be chosen to fit best the surface chemistry of the nanomedicine [59–61]. Commonly used methods used for introducing prosthetic groups include amide coupling, thiol-maleimide coupling, click chemistry, glycosylation or oxime coupling. Very often, the surface of nanomedicines has to be decorated with reactive groups that enable indirect labeling [62,63].

2) Core labeling

Achieving stable attachment of radionuclides to the surface of nanomedicines can be problematic. Enzymatic cleavage of covalent bonds or sequestering of radiometals by endogenous metal-binding proteins may result in a release of radionuclides from the nanomedicine [93]. As a consequence, the observed biodistribution of radioactive signal would no longer represent the actual distribution of the nanomedicine [94,95]. A solution to this problem is to introduce the label into the core of the nanomedicine. In this instance, release of radionuclide from the nanomedicine is prevented unless the nanomedicine has degraded. Encapsulation (for organic polymers, nanotubes or liposomes) or doping (for inorganic nanoparticles) are commonly applied strategies (Table 2B).

In addition to these common strategies an elegant, but also exotic method of core labeling for nanomedicines was reported by Perez-Campaña et al. [91,92]. In this method, [$^{18/16}\text{O}$]Al₂O₃ nanoparticles were irradiated with a proton beam, which converted the stable nuclides oxygen-18 and oxygen-16 within the nanoparticle into the positron-emitting radionuclides fluorine-18 and nitrogen-13, respectively. So far, the work of Perez-Campaña et al. remains the only example of radiolabeling of nanoparticles by particle beam activation. Although conceptually interesting, this approach is unlikely to see widespread use in neither preclinical nor clinical settings since the procedure is time-consuming, expensive and only applicable to a certain type of nanoparticles.

2.3. The radionuclide dilemma

As previously mentioned, the slow pharmacokinetics of nanomedicines is only compatible with long-lived radionuclides, such as iodine-124, zirconium-89, or indium-111. All of these radionuclides

Table 1
Nuclear properties of radionuclides used in SPECT and PET imaging [40–42].

	Radionuclide	Modality	Half-life ^a	Branching fraction (β^+) ^b (%)	Maximum (average) positron range ^c in water (mm)	Gamma-photon energy ^d (keV)	Effective dose ^e [mSv/MBq]
Radionuclides suitable for imaging slow clearing agents	^{123}I	SPECT	13.3 h	—	—	159	0.017 [43]
	^{111}In	SPECT	67.3 h	—	—	171 and 245	0.346 [44]
	^{64}Cu	PET	12.7 h	17.5	2.9 (0.6)	—	0.032 [45]
	^{72}As	PET	25.9 h	88	18.2 (5.2)	—	n.d. ^f
	^{89}Zr	PET	78.4 h	22.7	4.2 (1.3)	—	0.660 [46]
Conventional PET/SPECT nuclides in the clinic	^{124}I	PET	100.2 h	22.8	11.7 (3.4)	—	0.580 [47]
	$^{99\text{m}}\text{Tc}$	SPECT	6.01 h	—	—	140	0.010 [48]
	^{11}C	PET	20.4 min	99.8	4.5 (1.3)	—	0.004 [49]
	^{68}Ga	PET	67.8 min	89.1	10.3 (3.6)	—	0.017 [50]
	^{18}F	PET	110 min	96.7	2.6 (0.6)	—	0.019 [51]

Notes:

^a Half-life is the time required for the activity to decrease to half of the original amount.

^b Fraction of radionuclide atoms that decay through positron emission.

^c Range that the positron travels before it annihilates with an electron in the surrounding matter; living tissue mostly consists of water.

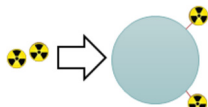
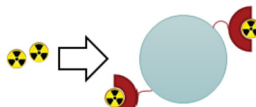
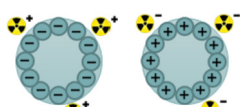




^d Energies of emitted gamma photons that are used for SPECT imaging.

^e Effective dose values represents the probability of cancer induction of low levels of ionising radiation. Presented values are taken from human dosimetry studies carried out and represent typical values using the radionuclide in request (However, the value can vary from tracer to tracer since the effective dose is depending on the used radionuclide as well as the biodistribution of the tracer).

^f n.d. = not determined.

Table 2

A general overview of commonly applied strategies for nanoparticle radiolabeling. (A) Surface labeling strategies. (B) Core labeling strategies.

Labeling method			Examples of suitable radionuclides	References	
A) Surface labeling	Direct	Covalent labeling		^{72}As , ^{124}I , ^{18}F	[64–68]
		Chelator based labeling		^{64}Cu , ^{68}Ga , ^{11}In	[36,69–71]
	Indirect	Ionic/coordinate bond labeling		^{18}F , ^{89}Zr , ^{111}In , ^{64}Cu , ^{68}Ga	[72–77]
		Prosthetic group labeling		^{11}C , ^{18}F , ^{64}Cu , $^{99\text{m}}\text{Tc}$, ^{124}I	[59,60,78–84]
B) Core labeling	Encapsulation	Trapping of the radiolabel in the internal cavity		^{111}In , ^{64}Cu , $^{99\text{m}}\text{Tc}$	[85–87]
	Doping	Incorporating the radionuclide into the lattice		^{111}In , ^{64}Cu , ^{68}Ga	[88–90]
	Stable nuclide activation	Producing the imaging nuclide via an external beam		^{13}N , ^{18}F	[91,92]

have long enough half-lives for imaging the in vivo behavior of nanomedicines over several days, which usually is the required timeframe to achieve the necessary target-to-non-target ratios (see Figs. 3 and 4A). However, use of such radionuclides results in a substantial radiation dose for patients, which is commonly viewed as unacceptable. Effective dose values for these radionuclides are in the range of 0.3–0.7 mSv/MBq (see Table 1) and can easily result in patient doses of 40–50 mSv per scan [44,46,47]. The annual dose constraint recommended by the International Commission on Radiological Protection is 20 mSv for patients undergoing diagnostic or therapeutic procedures with radiopharmaceuticals [96]. Therefore, received doses using nanomedicines labeled with long-lived radionuclides restrict repeated applications and the absolute amount of radioactivity that can be administered. In addition, long-lived positron emitters (^{89}Zr , ^{124}I) also tend to have low β^+ -branching fractions, which can decrease quantitative accuracy and the quality of the obtained images. In comparison, conventional short-lived PET radionuclides like carbon-11, fluorine-18 and gallium-68 decay almost exclusively through positron emission and

their effective dose values are more than an order of magnitude lower, 0.005–0.02 mSv/MBq. However, radiolabeling of nanomedicines with these short-lived radionuclides will not provide high enough signal at the required imaging time. This represents the radionuclide dilemma.³ Finally, radionuclides such as copper-64 and iodine-123, with moderate half-life (12.7 h and 13.3 h, respectively) and a relatively low radiation burden (approx. 0.03 mSv/Bq) are also not capable of imaging nanomedicines beyond 2–3 days post-administration. This timeframe is typically insufficient to obtain optimal target-to-non-target contrast and consequently, the best imaging quality.

An elegant strategy to circumvent this dilemma is pretargeting. It allows the use of short-lived PET radionuclides with low effective dose values and beneficial radiophysical imaging properties. Therefore, the use of long-lived radionuclides can be circumvented, and better imaging contrast can be obtained at earlier timeframes [97].

In the following sections, the concept of pretargeting will be explained, as well as interactions and chemical reactions used for such a strategy. In addition, a demonstration of how the application of pretargeted imaging and therapy could facilitate the translation of nanomedicines from preclinical research into clinical practice will be given.

³ The radionuclide dilemma: Long-lived radionuclides have to be used to be able to image the slow pharmacokinetics of nanomedicines. These long-lived radionuclides result in high radiation doses. Short-lived radionuclides are not compatible with the slow pharmacokinetics of nanomedicines. As such, no perfectly suited radionuclides exist for this application.

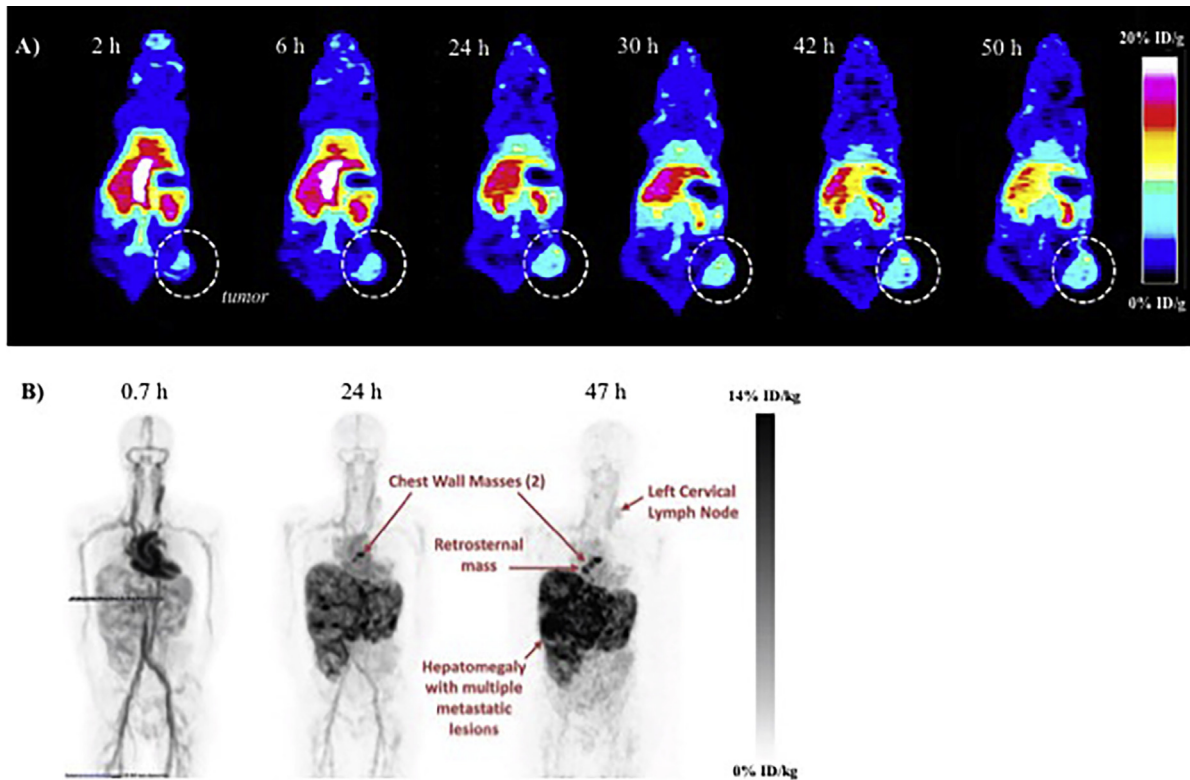


Fig. 3. Nanomedicines that passively accumulate into the tumor via the EPR effect need long timeframes to achieve good target-to-non-target contrast. (A) Time-dependency of the passive accumulation of ^{64}Cu -labeled glycol chitosan nanoparticles (^{64}Cu -CNPs) in SCC7 tumor bearing mice. At early time-points the contrast between tumor and background is low. However, the contrast increases over time as ^{64}Cu -CNPs are excreted. Figure modified from Ref. [9]. (B) Biodistribution profile of ^{64}Cu -MM-302 (^{64}Cu -labeled HER2-targeted PEGylated liposome containing doxorubicin) in patients with metastatic breast cancer. The accumulation profile of ^{64}Cu -MM-302 is independent of the targeting ligand, hence dictated primarily by the EPR effect. Immediately after administration, ^{64}Cu -MM-302 activity is primarily confined to the blood pool. Only after 24 h and 38 h, uptake of ^{64}Cu -MM-302 is evident in liver, as well as in various tumor lesions. Figure modified from Ref. [9].

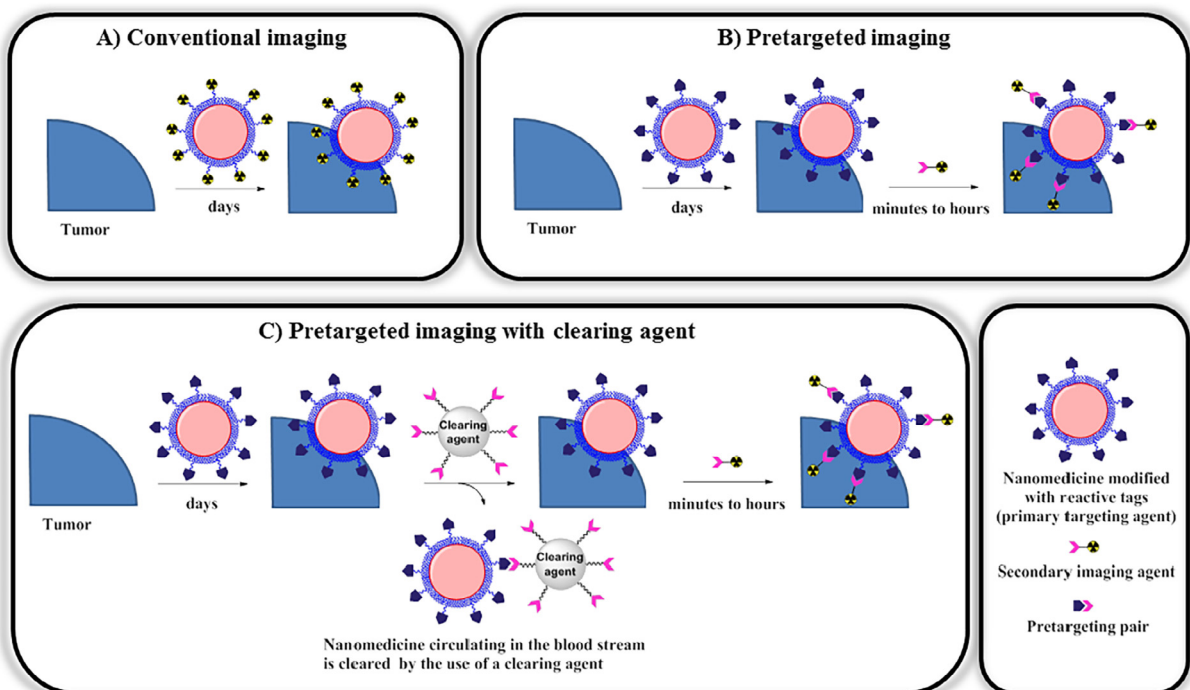


Fig. 4. Different approaches for nuclear imaging of nanomedicines. (A) Conventional imaging (B) Pretargeted imaging (C) Pretargeted imaging with clearing agent.

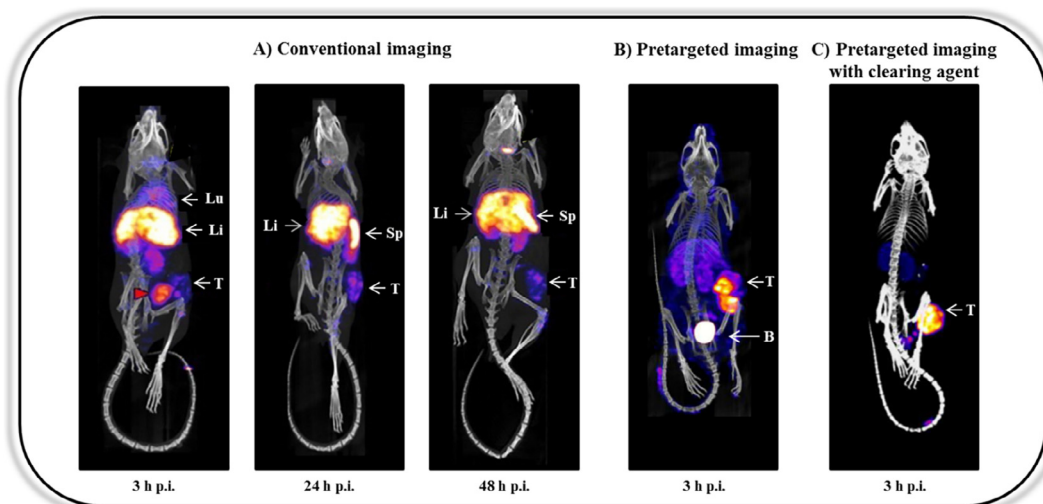


Fig. 5. SPECT/CT images from (A) Conventional imaging of ^{125}I -labeled anti-endoglin (CD105) mAbs targeting B16 tumors (B) Pretargeted imaging of a TAG-72 targeting mAb (CC49) with ^{111}In]In-DOTA-PEG₁₁-Tz **1** as a secondary agent in colon carcinoma xenografts (C) Pretargeted imaging with clearing agent for the mAb CC49/ ^{111}In]In-DOTA-PEG₁₂-Tz **1** pretargeting system (more than a 100-fold higher imaging contrast compared to B). Abbreviations of organs: B = bladder; Li = liver; Lu = Lungs; Sp = spleen; T = tumor. Images from Refs. [97,100,101].

3. Pretargeted nuclear imaging

3.1. The concept

A pretargeted imaging approach circumvents the drawbacks usually related with conventional imaging (see 2.3: The radionuclide dilemma) (Fig. 4A). This is possible since in pretargeted imaging, the slow passive targeting process of nanomedicines is separated from the actual imaging by using a so called pretargeting pair, which consists of a tagged nanomedicine (primary targeting agent) and a secondary imaging agent (Fig. 4B).

The approach is divided into two steps. In the first step, the nanomedicine is injected and allowed to accumulate in the target tissue over a sufficient period of time, usually days. In the second step, the imaging step, a radiolabeled secondary imaging agent is administered [98,99]. The secondary imaging agent will either interact or covalently bind to the compatible tag on the nanomedicine (depending on which type of pretargeting pair is used). As a result, the target accumulation of the nanomedicine can be imaged in an indirect fashion. Preferably, the secondary imaging agent should be designed so that it is rapidly cleared and radiolabeled with a short-lived, high positron-emitting radionuclide, e.g. carbon-11, fluorine-18 and gallium-68. Consequently, the absorbed radiation burden will be lower, and the imaging contrast higher. In order to reduce the period of time between the accumulation and the imaging step, a clearing agent step can be added (Fig. 4C). The clearing agent removes circulating nanomedicines from the blood stream and usually transports them to the liver or spleen within a few hours [97]. Fig. 5 compares the image quality that can be obtained using conventional (Fig. 5A), pretargeting (Fig. 5B) and pretargeting with clearing agent (Fig. 5C) strategies to image slow clearing monoclonal antibodies (mAbs). Monoclonal antibodies as nanomedicines have slow pharmacokinetic properties.

3.2. The potential of pretargeted imaging for nanomedicines

Drug delivery strategies based on passively targeted nanomedicines have the potential to improve current cancer therapy. Then again, the magnitude of the EPR effect varies between patients, and as such not all patients respond to nanomedicine

treatment approaches. Therefore, it is important to distinguish potential responders from likely non-responders (personalized medicine). In fact, the use of passively targeted nanomedicines on non-responders would not only be ineffective, but harmful. As discussed (see 3.1), pretargeting strategies hold great potential for imaging of long-circulating nanomedicines because they have the possibility to reduce the radiation burden for patients and increase imaging contrast. In the context of companion diagnostic imaging for mAb-based medicines, pretargeted imaging has already attracted a lot of interest [102,103].

However, only a few preclinical studies involving pretargeted imaging with passively targeting nanomedicines have been reported [104–107]. This is surprising considering the potential clinical impact of nanomedicines. In fact, nanomedicines are better suited for pretargeted imaging than mAbs because nanomedicines can carry more reactive tags. This is important since higher tag-loading increases the likelihood for pretargeting strategies to occur [103]. Typically, only 5–10 reactive tag groups can be introduced into mAbs without impairment of their targeting properties [97,108–110]. Higher numbers lead to aggregation [111–114] and aggregation, in turn, prevents the mAb from accumulating at the target-site.⁴ High reactive tag-loading of mAbs can also lead to interference with the target antigen recognition and prevent selective binding of the mAb. In contrast, nanomedicines can be designed in such a way that aggregation is prevented⁵ and consequently, higher loadings of reactive tags per nanomedicine can be realized (Fig. 6). The maximum number of reactive tags for a passively targeted nanomedicine has not been thoroughly investigated, but at least an 8-fold higher tag load compared to mAbs was reported to be achievable without aggregation [115].

⁴ Aggregation adducts of mAbs are more prone to be recognized by the reticulo-endothelial system due to their increased size. In addition, they can grow to such a size that they are stuck in small blood capillaries (e.g. in the lungs). Finally, aggregation of mAbs could influence the mAbs binding site, which can result in a loss of target affinity.

⁵ For instance, modifying the surface of the nanomedicine in order to make it hydrophilic and/or charged prevents inter-particle aggregation.

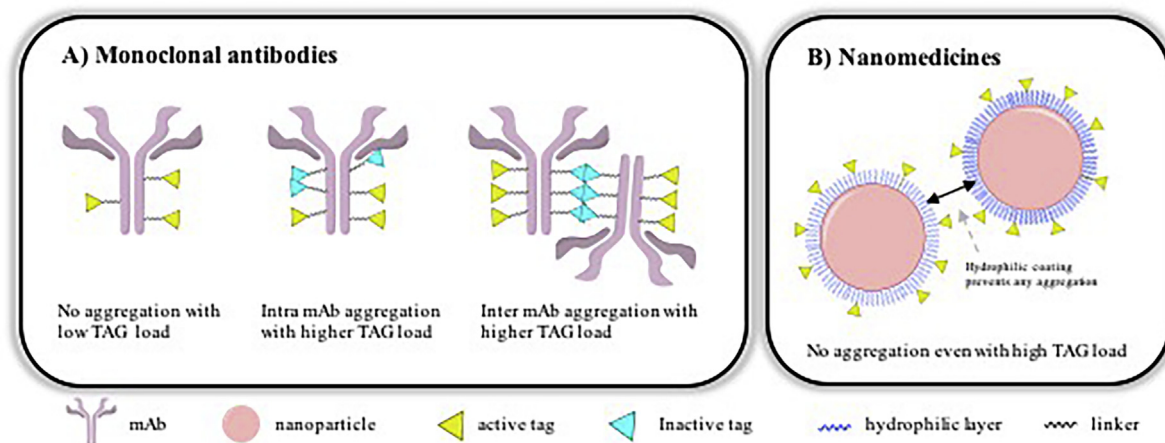


Fig. 6. Tag-load and aggregation probability. (A) In highly modified mAbs only a fraction of tags retains reactive. (B) Nanomedicines permit high tag-loadings without triggering aggregation.

3.3. Pretargeting strategies

In general, there are two types of pretargeting systems: (I) non-covalent high-affinity interactions and (II) covalent bond formations via bioorthogonal chemistry. The first pretargeting strategies developed fall within the first category. They rely on high-affinity interactions between biomolecules [102] such as the bispecific antibody (bsAb) and hapten recognition, the interaction between (strept)avidin and biotin, and the hybridization of complementary oligonucleotides. Modern pretargeting strategies rely on bioorthogonal chemical reactions between small molecule tags. Bioorthogonal reactions are defined as: “chemical reactions that neither interact nor interfere with a biological system.” – C.R. Bertozzi (2003) [116].

3.3.1. Non-covalent high-affinity interactions

Pretargeting strategies based on non-covalent high-affinity interactions involve biological molecules that tightly interact with each other. These interactions are governed by high affinity and highly specific hydrogen bonding interactions that occur in a biological medium.

3.3.1.1. Bispecific antibody and hapten recognition. One of the most extensively studied pretargeting strategies involves the use of bispecific antibodies (bsAbs) and radiolabeled haptens. A bsAb is an artificially produced antibody (Ab) that has been engineered to target two different antigens or epitopes (the area of antigen recognized by the immune system) [117], whereas a hapten is a non-immunogenic small molecule e.g. a peptide that binds specifically to an Ab with high affinity ($K_d = 10^{-5}$ – 10^{-10} M) [118,119]. Reported rate constants for the interaction have been within the range of 10^3 – $5 \text{ M}^{-1} \text{ s}^{-1}$ [120].

For pretargeted imaging, the hapten is radiolabeled and administered after the bsAb has localized at the target-site (using the tumor binding side of a bsAb). Afterwards, the radiolabeled hapten binds to the specific hapten binding-site of the bsAb. To ensure high target-to-background ratios, haptens have to be designed in such a manner that they possess an adequate circulation time before they are excreted. The combination of high selectivity, fast targeting and reasonable clearance allow haptens to be used for in vivo pretargeting strategies.

3.3.1.1.1. In vivo imaging applications. The first application of pretargeted tumor imaging was described in 1986 and made use of the bsAb and hapten recognition [121]. In this initial report, mice

bearing syngeneic KHJJ adenocarcinoma tumors were administered with the bsAb, WC3A11 IV. After 20 h, a cobalt ethylenediaminetetraacetic acid (EDTA) hapten chelate bound to human transferrin was administered as a clearing agent and the resulting aggregate was cleared through the liver [119]. In the final step (Fig. 7A), an ^{111}In -labeled EDTA-based hapten (^{111}In]In-BLEDTA IV 2) (Fig. 7B) was administered 1 h after the clearing agent. A tumor uptake of 1.4% injected dose per gram (ID/g) was observed 3 h post injection (p.i.) compared to 0.72% ID/g without bsAb pretreatment. Tumor accumulation without a clearing agent was much higher (4.07% ID/g), however the tumor-to-blood ratio was lower (0.68 without clearing agent compared to 8.72 with clearing agent). As a consequence, tumor visualization was best when the clearing agent was used. Despite the groundbreaking success of this initial study, the overall tumor uptake was quite low and imaging contrast was poor (Fig. 7C).

As an alternative, Stickney et al. developed a novel ^{111}In -labeled EDTA-based hapten, ^{111}In]In-EOTUBE 3 (Fig. 8A). This probe was evaluated in mice bearing human colon cancer xenografts and compared with the previously developed probe, ^{111}In]In-BLEDTA IV 2 (Fig. 7B). In this study, ^{111}In]In-BLEDTA IV 2 and ^{111}In]In-EOTUBE 3 were administered 24 h after intravenous administration (i.v.) of the bsAb (14 μg) [118]. The radioactivity was co-administered with a dose of 3 μg of the bsAb as a carrier. The carrier protein was included to prolong the plasma retention of the otherwise rapidly clearing ^{111}In -labeled hapten.⁶ This strategy is effective because the hapten and the bsAb bind reversibly. Therefore, over time the hapten is released from the circulating bsAb and made available to bind to the pretargeted bsAb in the tumor. As a consequence, the blood elimination half-life for the hapten is increased. Using this procedure, the original probe, ^{111}In]In-BLEDTA IV 2, showed an increased tumor uptake of 7% ID/g 24 h p.i. (determined by ex vivo biodistribution) and the novel probe, ^{111}In]In-EOTUBE 3, resulted in an even higher uptake (18.5% ID/g) using the same procedure. These results inspired Stickney et al. to advance ^{111}In]In-EOTUBE 3 to clinical studies, in which 14 patients between 62 and 82 years of age with metastatic or recurring adenocarcinoma of the colon were included. They were co-administered with ^{111}In]In-EOTUBE 3 (Fig. 8A), and a small

⁶ If the clearance of the secondary imaging agent is too rapid there is a lower probability for the pretargeted interaction to occur, resulting in lower target accumulation.

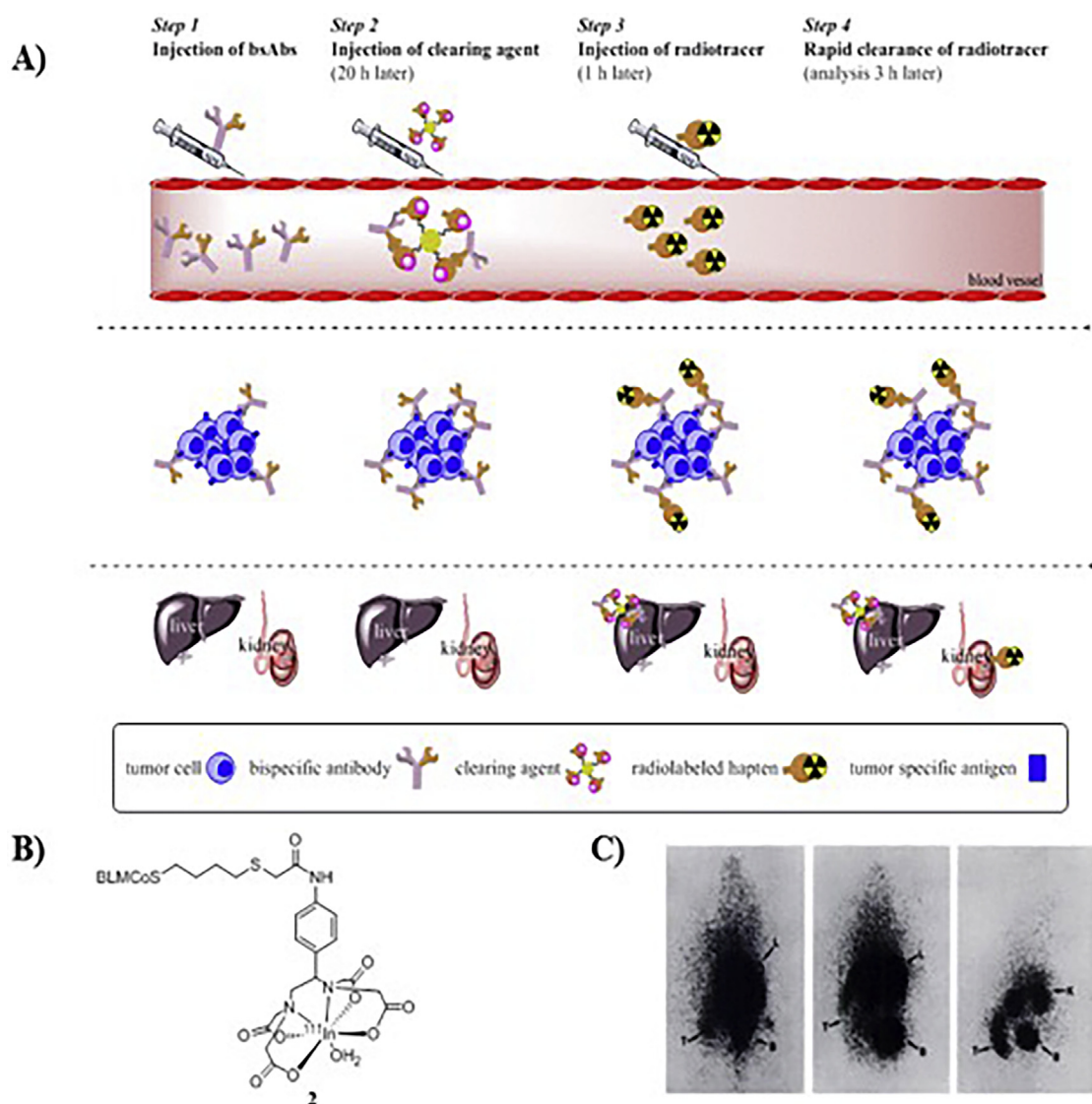


Fig. 7. (A) Representation of the pretargeting system using bsAbs and a radiolabeled hapten. In the first step, the bsAb was injected intravenously and allowed to reach maximal tumor accumulation. In the second step a clearing agent (human transferrin functionalized with the Co-chelated hapten) was administered to clear any remaining bsAb from the blood pool. In the third step the ^{111}In -labeled hapten was administered and allowed to accumulate at the target-site. The ^{111}In -labeled hapten rapidly cleared from the blood stream and imaging can proceed. (B) Structure of ^{111}In -BLEDTA IV 2, BLM = bleomycin. (C) Posterior gamma camera pinhole images of KH1J tumor bearing mice. Left Image: control mouse with ^{111}In -BLEDTA IV 2 21 h p.i. Middle image: mouse pretreated with WC3AI IV followed 21 h later by injection with ^{111}In -BLEDTA IV 2 Right image: mouse pretreated with WC3AI IV followed by injection of clearing agent 20 h later and then 1 h later injection of ^{111}In -BLEDTA IV 2 21 h p.i. Arrows indicate T = Tumor; L = Liver; K = Kidney; B = Bladder. Fig. 7C modified from Ref. [119].

amount (0.1–5 mg) of the bsAb as a carrier protein. Out of the 21 known lesions, 20 were detected [118].

3.3.1.1.2. Affinity enhancement strategy and state-of-the-art studies. The use of a bsAb as a carrier protein was successful in enhancing tumor uptake of the fast clearing radiolabeled hapten, however, it also resulted in longer circulations times. This is a problem for imaging purposes. Adequate uptake values were only observed after 24 h. In an attempt to solve this problem an alternative strategy was proposed using bivalent haptens. Bivalent haptens are capable of binding to two neighboring bsAbs at once. This increases the affinity between the hapten and the bsAb. Consequently, an increased retention at the target is expected and furthermore, this approach could eliminate the need for a clearing agent. In this respect, an ^{111}In -labeled bivalent hapten was developed and used to target an anti-CEA \times anti-diethylene-triaminepentaacetic acid (DTPA)-In-bsAb in a pretargeting

experiment using LS174T tumor bearing mice. Tumor-to-blood ratios were higher (7.9 ± 1.1) when compared to values obtained using monovalent haptens (4.5 ± 1.0) or directly labeled Abs (2.0 ± 0.3) [122]. The use of bivalent haptens made the bsAbs and hapten recognition strategy attractive for applying short lived radionuclides such as gallium-68 or fluorine-18 and several studies have been successfully published applying this strategy (Fig. 9) [123,124].

3.3.1.1.3. Application to nanomedicines. Due to the nature of the interaction, the bsAb and hapten recognition is limited to Ab-based nanomedicines. For example, Rauscher et al. reported a study in which the tumor accumulation of liposomes was increased using a pretargeting strategy. First, a liposome modified with a bsAb was administered and allowed to specifically bind. Afterwards, a radiolabeled liposome functionalized with multiple haptens was administered as the secondary imaging agent. A tumor uptake of

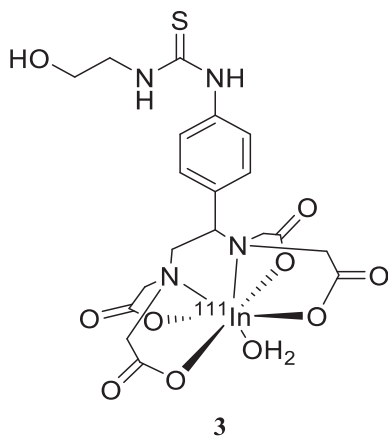


Fig. 8. Structure of [¹¹¹In]In-EOTUBE 3.

$7.5 \pm 2.4\%$ ID/g was obtained using this pretargeting approach. This uptake was higher compared to the uptake applying conventionally radiolabeled liposomes ($4.5 \pm 0.45\%$ ID/g) [125].

3.3.1.1.4. *Concluding remarks – bispecific antibodies and hapten recognition.* The bsAb and hapten recognition has been extensively studied in patients and clinical trials are ongoing [126–128]. Some

challenges that could hinder the widespread use of this system, especially for companion diagnostic imaging, include the immunogenic response towards the bsAb and challenges in producing them.

3.3.1.2. *(Strept)Avidin-biotin interaction.* Another extensively studied pretargeting approach is based on the (strept)avidin-biotin interaction. Avidin is a tetrameric 66-kDa glycoprotein commonly found in egg whites. Streptavidin is a non-glycosylated 60-kDa variant, which is found in *Streptomyces avidinii* culture [108]. Avidin and streptavidin are both comprised of four identical subunits that each bind to a single biotin unit. Biotin is a 244-Da water soluble small molecule that is also referred to as vitamin B7 (formerly vitamin H or coenzyme R) [102]. The affinity between (strept)avidin and biotin is one of the strongest known non-covalent interactions ($K_d = 10^{-15}$ M) (Fig. 10) with rate constants in the order of 10^7 M⁻¹ s⁻¹ [129–132]. The interaction has been applied in numerous aspects of biotechnology e.g. in immunological assays, electron microscopy, affinity chromatography, and nucleic acid hybridization [133].

3.3.1.2.1. *Pretargeting strategies. I) Streptavidin vs. avidin:* Although streptavidin and avidin have essentially identical binding affinity for biotin, their use is highly dependent on the intended application as they each have different in vivo pharmacokinetics. For example, avidin is often used as a clearing agent since it rapidly

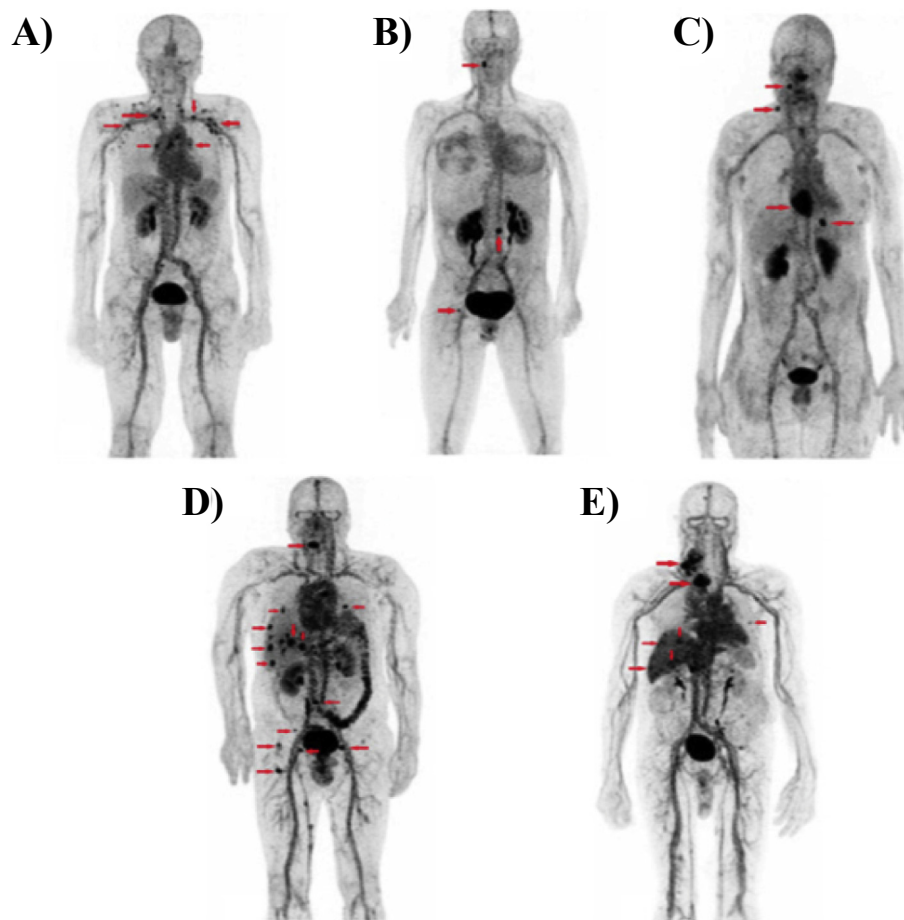


Fig. 9. PET maximum-intensity-projection images recorded in 1 patient of each cohort. Arrows showed foci considered as pathologic by immuno-PET. (A) Supradiaphragmatic nodes in patient 1. (B) Cervical node; lumbar and femoral bones foci in patient 2. (C) Supradiaphragmatic nodes and liver and heart lesions in patient 3. (D) Supradiaphragmatic nodes, lung, liver, and bone foci in patient 4. (E) Supradiaphragmatic nodes and liver foci in patient 5. Figure modified from Ref. [124].

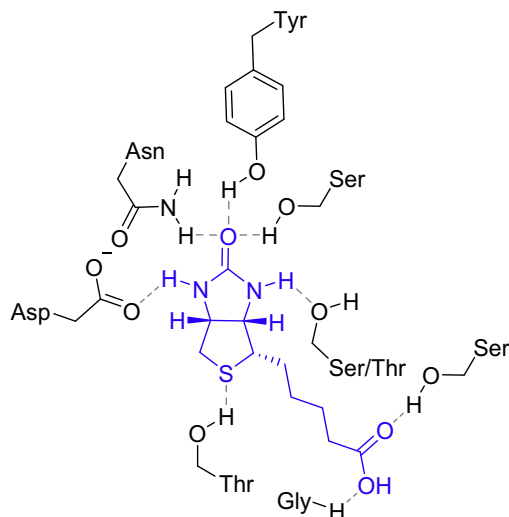


Fig. 10. Representation of the hydrogen bonding framework between biotin (blue) and streptavidin (Ser)/avidin (Thr) ($K_d = 10^{-15}$ M). Hydrophobic effects increase the bond strength between the hydrogen bond framework.

clears from the circulation via liver excretion [134]. Streptavidin is often used in mAb conjugates or as a radiolabeled secondary imaging agent because streptavidin displays higher *in vivo* stability and longer circulation times than avidin [135,136].

II) (Strept)avidin vs. biotin: The (strept)avidin-biotin interaction can in principle be applied in two ways for pretargeted imaging [108,135,137,138]. Either the primary targeting agent can be functionalized with (strept)avidin and biotin being used as the secondary imaging agent or the primary targeting agent can be functionalized with biotin and (strept)avidin being used as the secondary imaging agent. Usually, the first option is applied in pretargeted imaging because (strept)avidin circulates much longer than biotin. Shorter circulation time for the secondary imaging agent lead to higher imaging contrast. Of course, only if the secondary imaging agent is able to bind effectively to the tagged primary targeting agent in the respective timeframe. Therefore, biotin is better suited to be used as the secondary imaging agent [137]. Biotin can be radiolabeled by applying a wide variety of strategies, including chelators such EDTA, DTPA and 1,4,7,10-tetraazacyclododecane-1,4,7,10-tetraacetic acid (DOTA). These chelators can be used to incorporate a broad set of radiometals [108].

A concern in using radiolabeled biotin as a secondary imaging agent is that endogenous biotin can block the binding sites of (strept)avidin and thus prevent radiolabeled biotin to bind to the preadministered nanomedicine. This effect is observed and discussed in some studies, but not reported to be problematic in other studies [137,139,140].

3.3.1.2.2. Functionalization strategies. Standard conjugation methods can be used to functionalize nanomedicines with (strept)avidin. However, a more exotic, but frequently applied, strategy also exists. In this approach, biotin is first coupled to the primary targeting agent and then this conjugated biotin is functionalized with (strept)avidin (Fig. 11). (Strept)avidin has four biotin binding sites, therefore this approach leaves three biotin binding sites available. However, dimers and polymeric structures are usually formed using this approach, which have to be separated from the desired product [108].

Conjugation of biotin to the primary targeting agent can be achieved using biotinylating agents such as sulfosuccinimidyl 6-(biotinamido) hexanoate for amine groups, *p*-diazobenzoyl-

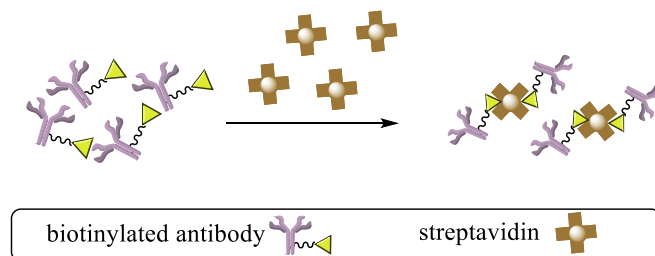


Fig. 11. Demonstration of antibody dimer formation following addition of streptavidin to biotinylated antibodies.

biocytin for tyrosyl and histidyl moieties or 3-(*N*-malimidopropionyl)biocytin for thiol groups [133].

3.3.1.2.3. *In vivo* imaging: proof-of-concept. The first successful *in vivo* pretargeting experiments using radiolabeled biotin was performed with implanted avidin coated beads in 1987 by Hnatowich et al. [135]. Only two mice were used in this initial study. The first mouse was injected intraperitoneal (i.p.) with ~120 000 particles (45–165 μ m) that were coated with avidin, while the second mouse received underivatized beads. Immediately after the administration of the particles, each mouse was given an 111 In-labeled biotin derivative. Imaging was performed 2 h p.i. High radioactive uptake corresponding to the location of the implanted avidin-coated beads was observed (Fig. 12A, right), whereas only kidney and bladder accumulation was detected in the control experiments (Fig. 12A, left).

This and follow-up studies encouraged Hnatowich and colleagues to translate the biotin-(strept)avidin based pretargeting approach to clinical application in 1990 [137]. Ten patients aged of 43–77 with squamous cell carcinoma were administered a streptavidin-functionalized HMFG1 mAb targeting this tumor type. After 2–3 days, an 111 In-labeled DTPA-functionalized biotin derivative was administered, and images were obtained 2 h p.i. As a negative control, the same patients were injected with the [111 In]DTPA-biotin in the absence of the streptavidin-conjugated mAb. The negative control study was carried out 2–3 weeks before the pretargeted imaging experiment. Only 3 patients displayed an observable improvement in image quality when pretreated with streptavidin-functionalized mAbs compared to the control experiments (Fig. 12B). No toxic effects were observed in this study. However, all patients did develop anti-streptavidin mAbs and thus showing an immunogenic response [142].

3.3.1.2.4. Clearing agents. The use of clearing agents to improve image contrast for mAb based strategies was first demonstrated using the (strept)avidin-biotin interaction on a conventionally 125 I-labeled IgG antibody. Up to 20% of the initial activity was still circulating 24 h p.i. In order to reduce this amount, the mAb was functionalized with biotin and the fast clearing avidin was used to clear the biotinylated mAb construct from circulation. After a single injection of avidin, the amount of radioactivity in the blood was reduced by 90–95% within 15 min. The majority (70%) of the radioactivity was cleared through the liver [134]. Although this strategy increases the imaging contrast and reduces the radiation dose that is received due to the slow clearance of the mAb, the strategy does not minimize the radiation dose that is received due to the slow target accumulation of the mAb.

This was addressed by Paganelli et al. in 1990 by applying a pretargeting strategy combined with a clearing agent step. However, Paganelli et al. used a slightly different variant of the clearing agent approach described in Fig. 4C [143–145]. In short, a biotinylated mAb was first administered and allowed to reach maximal target accumulation. Afterwards, avidin was administered. This

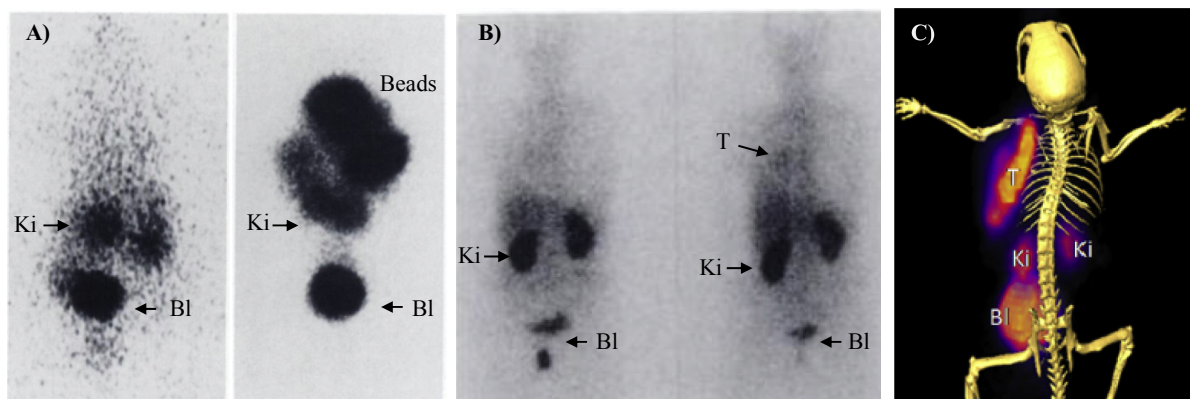


Fig. 12. (A) Whole body images of two mice injected i.p. with avidin-functionalized (right) and unfunctionalized (left) beads followed 2 h later with ^{111}In -labeled biotin. Signal in the upright corner of the left image represents the location of the avidin-coated beads. (B) Images of the anterior chest and upper abdomen of the same lung cancer patient administered with ^{111}In -labeled biotin after receiving a streptavidin-functionalized antibody 2 weeks (left) or 2 days (right) prior. (C) $\mu\text{PET/CT}$ images of ^{68}Ga -ATRIDAT-BIO (30 MBq) injected in avidin treated nude mice xenografted with A549 tumor cells. Abbreviations of organs: T = Tumor; Beats = avidin-coated beads; L = Liver; Ki = Kidney; Bl = Bladder. Figure modified from Refs. [135,137,141].

served two purposes: (I) Avidin should bind residual biotinylated mAbs circulating in the blood stream and clear it via liver excretion and (II) avidin should bind to the biotinylated mAb at the target and increase the number of binding sites (this is possible since only one of the four domains of avidin binds to the biotinylated mAb at the target). Finally, radiolabeled biotin was administered to target the avidin-functionalized biotinylated mAb (Fig. 13). Compared to the standard 2-step pretargeting procedure (Fig. 4B), this 3-step procedure can increase imaging contrast between the blood and target tissues up to 10-fold [146].

However, the aforementioned 3-step approach raises the question as to why it would be preferable to functionalize the mAb in vivo as opposed to prior to injection. First, the formation of mAb aggregates (see Fig. 11) is eliminated and thus tedious purification of the end product is avoided. Furthermore, the injected avidin can bind to endogenous biotin and clearing it from the system before the radiolabeled biotin is administered. This avoids any potential blocking of the streptavidin binding units at the target-site by endogenous biotin.

3.3.1.2.5. Application to nanomedicines. The (strept)avidin-biotin interaction has been applied to pretargeted imaging of a bifunctional multivalent phage in a murine prostate cancer model. Both the standard pretargeting strategy (without applying clearing agents) (Fig. 4B) and the modified strategy developed by Paganelli et al. (Fig. 13) were used in this study [147]. In the standard approach, a biotinylated phage was injected into SCID mice bearing PC-3 human prostate carcinoma tumors. After 4 h, an ^{111}In -labeled DTPA streptavidin conjugate was injected and imaging was performed after an additional 4 h. In the modified approach, mice were administered with avidin 4 h after the biotin-functionalized phage were injected and 24 h before ^{111}In -labeled biotin. The modified procedure resulted in a higher tumor uptake (4.34% ID/g) than the standard approach (0.67% ID/g).

3.3.1.2.6. Concluding remarks – (Strept)Avidin-biotin interaction. Although there are recent preclinical developments applying this strategy (Fig. 12C) [141,148], its use in clinical applications has seen a decline. This is evident by the lack of registered on-going clinical trials using this system for pretargeting (i.e. ClinicalTrials.gov). In a head-to-head comparison of this system and the bsAb-hapten pretargeting system, it was found that the latter was superior [132]. The reason for this was a better biodistribution profile, better therapeutic efficacy of a ^{90}Y -labeled hapten secondary agent, and reduced immunogenicity. Despite early promising clinical results,

this strategy suffers from a number of drawbacks. This includes development of an immunogenic response, difficulties in producing streptavidin conjugates, and influence on target uptake of the primary targeting agent due to the large size of streptavidin.

3.3.1.3. Hybridization of complementary oligonucleotides. The high affinity of the non-covalent interaction arriving from Watson-Crick base pairing can also be utilized for pretargeting strategies. In this instance, high numbers of base pairs are used to let oligonucleotides hybridize via hydrogen-bonding that occurs between two chains of complementary nucleotides. In DNA, adenine forms a base pair with thymine and guanine forms a base pair with cytosine (Fig. 14A). The same interaction is present in RNA except thymine is replaced by uracil [149,150]. The resulting hybridization gives second order rates in the range of $10^4 \text{ M}^{-1} \text{ s}^{-1}$ for complementary oligonucleotides. Reaction kinetics that make the system attractive for pretargeted imaging [151]. However, DNA- or RNA-based oligomers are both rapidly degraded in vivo by nucleases, which prevents its use for in vivo imaging strategies [152–154]. Phosphorodiamidate morpholino oligomers (PMOs), peptide nucleic acid (PNA) and phosphorothioates derivatives have been designed to overcome this problem (Fig. 14B and C) [155–157]. In the following, our discussion will focus on PMOs and PNAs since this strategy is by far more applied.

3.3.1.3.1. Phosphorodiamidate morpholino oligomers (PMOs). PMOs are oligonucleotide analogs comprised of DNA base pairs attached to an achiral, non-ionic backbone made up of morpholine groups linked through phosphorodiamidate groups (Fig. 14B). This backbone replaces the ribose/furanose phosphodiester-linked moieties present in DNA and RNA. An advantage of this modification is that water-soluble PMOs are resistant to both nucleases and proteases, while still able to bind to complimentary base pairs through Watson-Crick hydrogen bonding [156]. The first in vivo application of this strategy was carried out in nude mice bearing LS174T tumors [158]. For pretargeting, 50 μg of the PMO-modified anti-CEA antibody (MN14) was administered and after 48 h a $^{99\text{m}}\text{Tc}$ -labeled complimentary PMO (cMORF) was injected. Images and ex vivo biodistribution studies were performed 3 h and 24 h p.i. High tumor accumulation of 1.8% ID/g (3 h p.i.) and 1.7% ID/g (24 h p.i.) was observed in mice injected with anti-CEA mAb. Control animals showed only an uptake of 0.09% ID/g 3 h p.i. and 0.05% ID/g 24 h p.i.. Tumor visualization using a scintillation camera was challenging at 3 h p.i. due to high background radioactivity in the

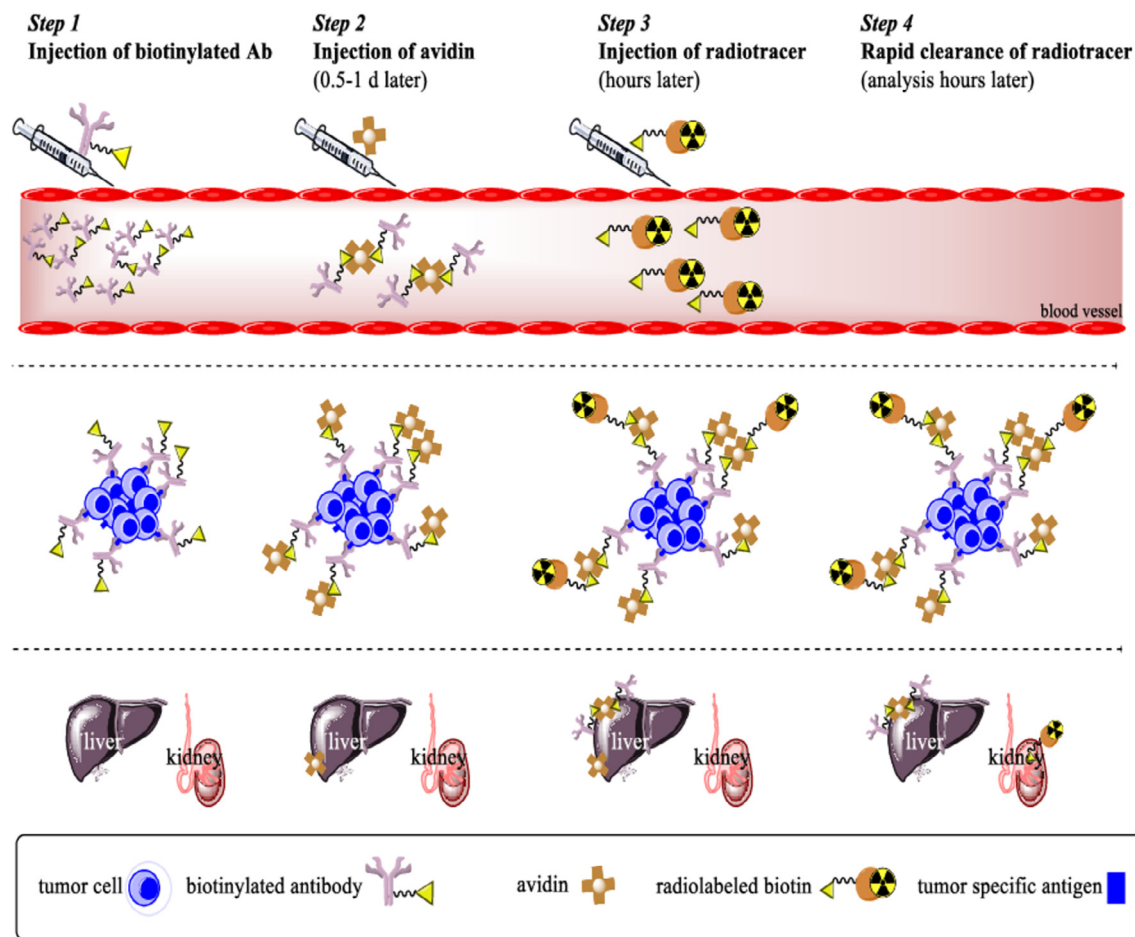


Fig. 13. Representation of the pretargeting system using biotin and avidin. In the first step the biotinylated mAb is injected i.v. and allowed to reach maximal tumor accumulation. In the second step avidin is injected as a clearing agent to clear any remaining biotinylated mAb through the liver and as a mean to functionalize the biotinylated mAb at the tumor-site. In the third step ^{111}In -labeled biotin is administered and accumulates at the tumor-target site. Finally, ^{111}In -labeled biotin rapidly clears through the kidneys and imaging can proceed.

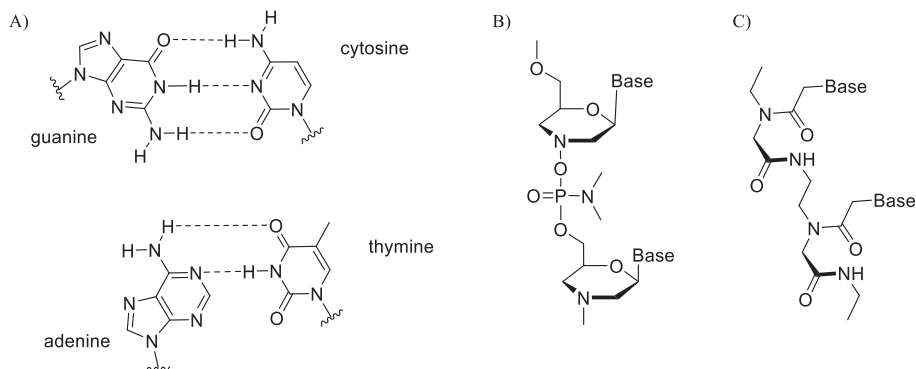


Fig. 14. (A) Watson-Crick base pairing in DNA between guanine and cytosine and adenine and thymine, respectively. (B) General structure of phosphorodiamidate morpholino oligomers (PMOs). (C) General structure of peptide nucleic acids (PNAs).

bladder (Fig. 15A). However, upon removal of the urine, good imaging contrast could be observed at 3 h p.i. (Fig. 15B). This imaging contrast was comparable with the one observed 24 h p.i. (Fig. 15C).

Since this report, a number of studies using PMOs have been reported with radionuclides for SPECT imaging [159–165] or radiotherapy [166,167]. However, there are no reports of PET imaging agents or clinical studies in the present literature.

3.3.1.3.2. Peptide nucleic acids (PNAs). Peptide nucleic acids

(PNAs), like PMOs, are oligonucleotide derivatives that have a modified backbone. In this case the sugar phosphate moieties of the DNA/RNA backbones have been replaced with a peptide backbone, typically made up of *N*-(2-amino-ethyl)-glycine units (Fig. 14C). Similar to the PMOs, the PNAs are achiral, non-ionic structures that are enzymatically stable, but still able to undergo Watson-Crick hydrogen bonding [157]. A pretargeting PNA-based approach was first reported in 1997 [168]. In this study mice bearing LS174T

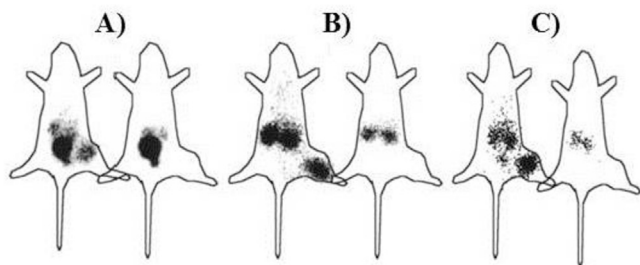


Fig. 15. Whole body gamma camera images of mice bearing LS174T tumors. Animals on the right were administered with the PMO-functionalized anti-CEA mAb and then 48 h later with the ^{99m}Tc -labeled cMORF. Animals on the left were only administered the ^{99m}Tc -labeled cMORF. (A) Images obtained 3 h p.i. (B) Images obtained 3 h p.i. after removing the urine. (C) Images obtained 24 h p.i. Figure modified from Ref. [158].

tumors were administered with streptavidin functionalized with PNA (150 μg) (streptavidin accumulates in tumors) [108]. After a 5 h lag time, a ^{99m}Tc -labeled complimentary PNA (cPNA) derivative was administered. SPECT imaging 4 h p.i. showed higher tumor uptake in the PNA pretreated group (0.29% ID/g) compared to those that did not receive PNA-functionalized streptavidin (0.10% ID/g). The same trend was observed for the tumor-to-muscle (thigh) ratio (3.5 vs 1.7). Overall the observed tumor uptake was low in this initial study, yet encouraging for further optimization [165,169,170]. Leonidova et al. were the first ones to demonstrate successful tumor targeting with this approach using an Ab conjugate [169]. In this study, mice bearing A431 tumor xenografts were administered a PNA-functionalized Ab (cetuximab), which targets the extracellular domain of the epidermal growth factor receptor (EGFR). A ^{99m}Tc -labeled complimentary PNA was 24 h afterwards injected. Tumor visualization was possible using SPECT/CT 1 h p.i. (Fig. 16A). In contrast, the control experiment, in which no Ab conjugate was injected, did not result in any tumor visualization (Fig. 16B). The tumor-to-muscle ratio achieved in the pretargeting study was 8.29. However, a low tumor-to-blood ratio was observed (0.48) due to incomplete elimination of the Ab from the blood. Despite promising preclinical studies, there are no current reports of this system being tested or used in a clinical setting.

3.3.1.3.3. Non-natural L-oligonucleotides. Recently, non-natural L-oligonucleotides (L-ONs), resistant to enzymatic degradation have been developed for pretargeted imaging. Schubert et al. reported the first study using L-ONs [171]. In this study, the EGFR specific mAb cetuximab (C225) and a ^{64}Cu -labeled 1,4,7-triazacyclononane-1,4,7-triacetic acid (NOTA) derivative were

both functionalized with L-ONs. The functionalized mAb (NOTA' 3 -C225-(c-L-DNA) $_{1.5}$, 4 nmol) was administered to FaDu tumor bearing mice and 4 h later the ^{64}Cu -labeled complementary L-ON (^{64}Cu]Cu-NOTA'-L-DNA-10 kDa-PEG) was injected. Tumor visualization with PET was possible 50 min p.i. (Standard Uptake Value (SUV_{mean}) = 0.7 ± 0.03), however, the highest tumor uptake was observed at 24 h p.i. (SUV_{mean} = 0.9 ± 0.2) (Fig. 17). A tumor-to-muscle-ratio of 10.59 ± 5.02 was determined following ex vivo biodistribution. These values were lower than what was found for the directly labeled mAb, where the SUV_{mean} for the tumor was 1.5 ± 0.1 at 23 h p.i. and the tumor-to-blood ratio was 14.6 ± 1.8 . Lower accumulation in the pretargeted case could be attributed to high liver accumulation of ^{64}Cu]Cu-NOTA'-L-DNA-10 kDa-PEG and internalization of the C225 mAb. Both incidents lower the possibility of pretargeting (less secondary imaging agent available and less accessible mAb since the primary imaging agent cannot cross cell membranes) [171].

In general, this pioneering work demonstrates the utility of this approach for in vivo imaging. However, optimization is required in order to incorporate short-lived radionuclides for clinical translation.

3.3.1.3.4. Concluding remarks – hybridization of complementary oligonucleotides. Despite promising preclinical experiments with mAbs and proteins/peptides, pretargeted imaging using

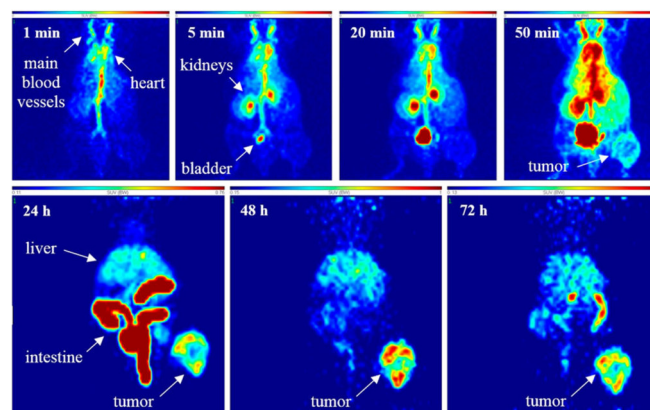


Fig. 17. PET images of FaDu tumor bearing mice administered with NOTA'^3 -C225-(c-L-DNA) $_{1.5}$ 24 h prior to administration of ^{64}Cu]Cu-NOTA'-L-DNA-10 kDa-PEG. Representative PET images (maximum intensity projection) at different time points after i.v. injection. Images were obtained 1 min, 5 min, 20 min, 50 min, 24 h, 48 h, and 72 h p.i. Figure modified from Ref. [171].

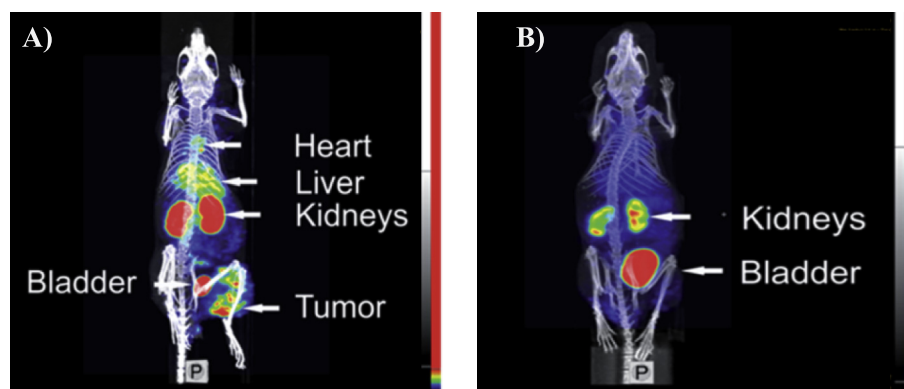


Fig. 16. SPECT/CT maximum intensity projections of mice bearing A431 tumor xenografts 1 h p.i. (A) Mouse was administered NOTA'^3 -C225-Cys-c-PNA 24 h prior to administration of ^{99m}Tc]Tc-Dpa)-(Cys-PEG10 kDa)-PNA. (B) Mouse was administered ^{99m}Tc]Tc-Dpa)-(Cys-PEG10 kDa)-PNA without pretargeting with NOTA'^3 -C225-Cys-c-PNA. Figure modified from Ref. [169].

hybridization of complementary oligonucleotides has not been applied to other systems, such as nanoparticles or polymers. No clinical studies have been reported so far.

3.3.2. Covalent bond formations via bioorthogonal chemistry

For a reaction to be classified as bioorthogonal, several requirements have to be fulfilled. First, the participating groups need to be inert towards other biological functionalities such as amino acid residues, nucleic acids, etc. Second, the groups have to be able to react with each other under biocompatible conditions. Finally, the reaction must be fast and specific. A number of bioorthogonal reactions have been described since the introduction of the term [172–177]. The first being the Staudinger ligation, in which an azide and a phosphine react to form an amide bond [172]. Later, a second version of the ligation was developed, the traceless Staudinger ligation. In comparison to the original Staudinger ligation, this reaction proceeds via an additional rearrangement that cleaves off the highly lipophilic phosphine adduct [173,174]. Both Staudinger ligations are limited by rather slow rate constants (for in vivo chemistry) and the tendency of phosphines to oxidize in vivo [178]. Nowadays, other bioorthogonal reactions have been shown to serve as better alternatives for in vivo applications, two of them, the strain-promoted azide-alkyne [3 + 2] cycloaddition (SPAAC) and the tetrazine ligation will be discussed in the following sections.

3.3.2.1. Strain-promoted azide-alkyne [3 + 2] cycloaddition (SPAAC).

In 2001 Kolb, Finn and Sharpless coined the term click chemistry. The aim of click chemistry was to easily connect fragments via a heteroatom linkage. The reactions should be fast and selective. In addition, few or no by-products should be formed, and the reaction should be carried out in water or benign solvents [179]. The reaction that launched the field of click chemistry was the Cu-catalyzed Huisgen [3 + 2] cycloaddition between azides and alkynes, also called the Cu-catalyzed azide-alkyne [3 + 2] cycloaddition (CuAAC) (Fig. 18). The reaction was reported by two independent research groups of Sharpless and Meldal in 2002 [180].

The [3 + 2] cycloaddition between azides and alkynes to form 1,2,3-triazoles was described previously in 1963 by Huisgen (Fig. 18), but the reaction required elevated temperatures and two

regioisomers (the 1,4- and 1,5-substituted triazole) were formed [181]. The introduction of a Cu-catalyst enabled a regioselective reaction yielding only in the 1,4-regioisomer. Moreover, the Cu-catalyst also allowed performing the reaction at lower temperatures [180,182]. On the other hand, the necessity of toxic Cu(I) prevents the use of the CuAAC for in vivo chemistry as Cu-ions can interact or chelate with biomolecules [183].

In order to circumvent the use of a metal catalyst, considerable efforts were directed towards finding a catalyst-free variant of the reaction. It was found that Cu was not necessary if the alkyne moiety could be activated by electron withdrawing groups (EWG). In this case, cycloadditions between ethyl 5-azidovalerate and both internal and terminal alkynes, e.g. methyl propiolate, ethyl but-2-ynoate and propargyl benzenesulfonate, could occur at room temperature and only the 1,4-regioisomer was formed [184]. However, these types of alkynes are not appropriate for in vivo chemistry, since they can also easily participate in Michael additions with nucleophiles [176]. In an attempt to increase reactivity of the alkynes, Bertozzi and co-workers started to study how the reaction was influenced by ring strain, an approach already pioneered by Wittig and Krebs with the smallest stable carbocyclic alkyne, cyclooctyne. This work resulted in a new bioorthogonal reaction; the SPAAC (Fig. 18) [176,185]. Here, the release of ring strain in the cyclooctyne upon reaction with the azide drives the reaction. No toxicity was observed when the authors applied the reaction in living cells (Fig. 18) [186]. The SPAAC was later successfully used for in vivo approaches in both zebrafish and mice [187,188].

The relationship between structural changes of the cyclooctyne and reaction kinetics for the SPAAC has been studied and an EWG, such as fluorine adjacent to the alkyne moiety is favorable for the rate of the reaction. Rate constants of approximately $0.1 \text{ M}^{-1} \text{ s}^{-1}$ can be reached [186,189]. In addition, cyclooctynes with fused ring system, e.g. dibenzocyclooctynes (DIBO), aza-dibenzocyclooctynes (DIBAC) and biarylazacyclooctynone (BARAC) show high rate constants, $0.17 \text{ M}^{-1} \text{ s}^{-1}$ (MeOH), $0.36 \text{ M}^{-1} \text{ s}^{-1}$ (D_2O) and $0.96 \text{ M}^{-1} \text{ s}^{-1}$ (MeCN), respectively [190–192]. However, the latter is reported to undergo spontaneous intramolecular rearrangement, which limits its use for in vivo applications [193].⁷

3.3.2.1.1. Preclinical pretargeting applications. To our knowledge, there are until now only three published studies, which use the SPAAC for pretargeting approaches in respect to nuclear imaging or radiotherapy [61,194]. For imaging purposes, a pretargeting PET approach was reported by Lee et al. in 2013, when mesoporous silica nanoparticles (NPs) were used to image U87 malignant glioma tumors in mice. PEG-linkers were attached to the NPs to increase biocompatibility and the size of the particles was set to be approx. 100–150 nm, a range in which NPs are reported to show EPR-mediated tumor targeting. Further modifications of the NPs were conducted in order to introduce the reactive tag (DIBAC) for the SPAAC. The PEG-linkers contained amine-functionalized end-groups that were coupled to NHS-functionalized DIBACs. After assessing tumor accumulation of the NPs by optical imaging, pretargeted imaging was performed with [^{18}F]fluoropentaethylene glycolic azide **4** as a secondary imaging agent (Fig. 19A). The time interval between administration of DIBAC-NPs and ^{18}F -labeled azide, respectively was set to 24 h [61]. A longer period of time was not selected because the used cyclooctyne moieties tend to undergo side reactions with biological nucleophiles, such as free thiol groups of cysteines during long-term in vivo exposure [195]. DIBAC-NPs (100 μg , 12 nmol of DIBAC) were injected i.v. into mice

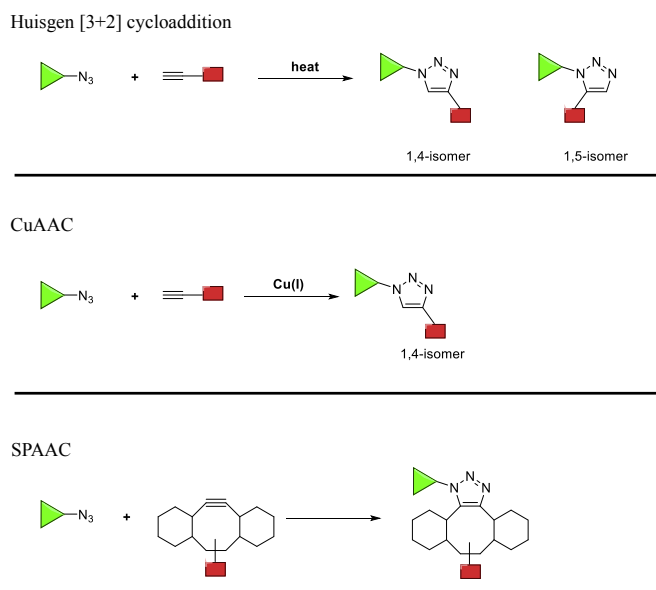


Fig. 18. Various azide-alkyne [3 + 2] cycloadditions; the Huisgen [3 + 2] cycloaddition, the CuAAC and the SPAAC.

⁷ It should also be stated that the SPAAC ($\sim 1 \text{ M}^{-1} \text{ s}^{-1}$) does not have as good reaction kinetics as the CuAAC ($10\text{--}100 \text{ M}^{-1} \text{ s}^{-1}$) [Rossin, R. et al., *Curr Opin Chem Biol*, 2014, 21: 161–9].

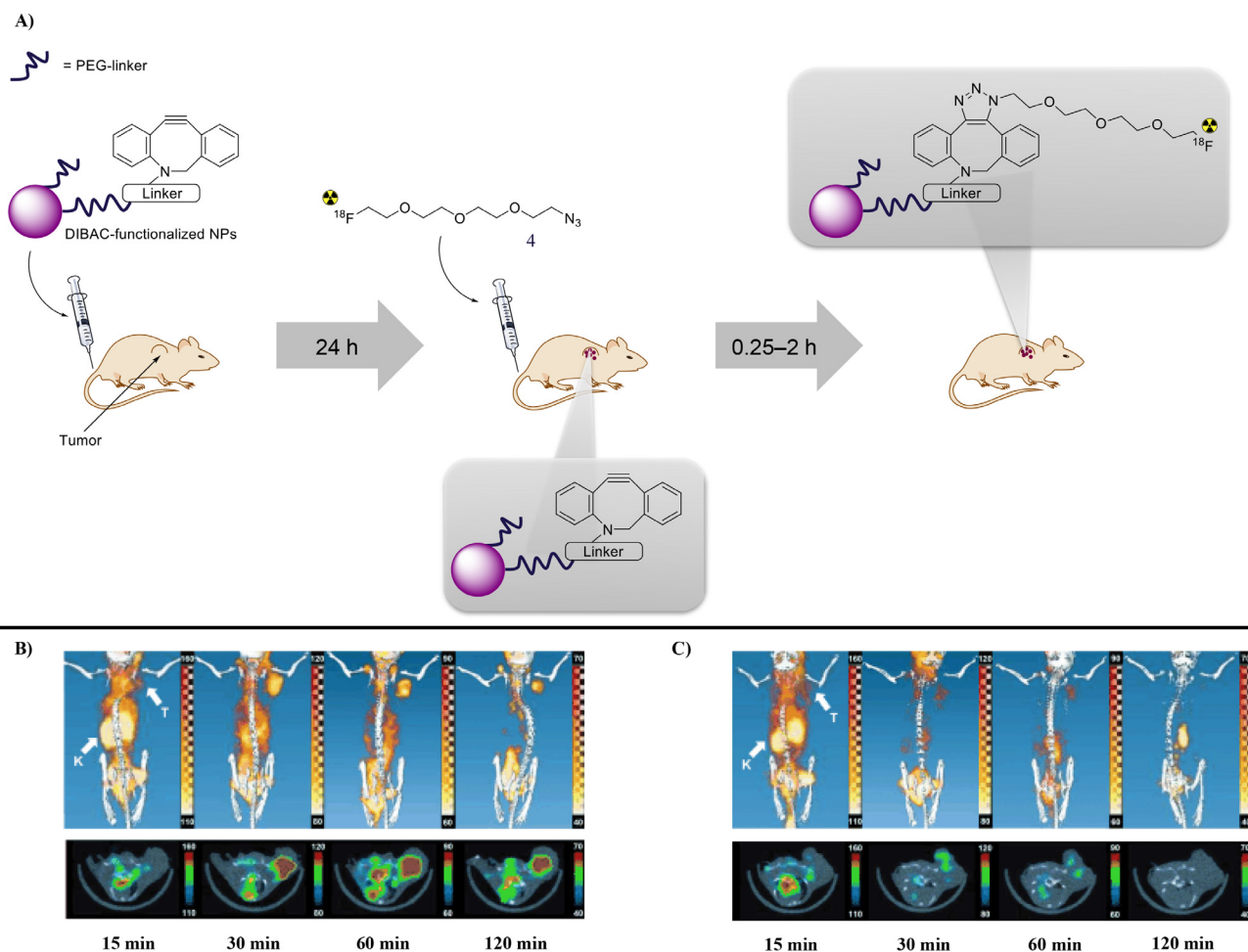


Fig. 19. (A) Pretargeted PET imaging with DIBAC-NPs and [^{18}F]fluoropentaethylene glycolic azide **4**. (B) PET/CT imaging of mice injected with DIBAC-NPs (250 μg) with a 24 h time interval before administration of secondary imaging agent, [^{18}F]fluoropentaethylene glycolic azide **4**. (C) PET/CT imaging of mice injected with only [^{18}F]fluoropentaethylene glycolic azide **4**. Abbreviations of organs: T = tumor; K = kidney. Figure modified from Ref. [105].

24 h prior to i.v. injection of the ^{18}F -labeled azide (2.6 MBq, with a A_m of 42 GBq/ μmol). Only a minor accumulation of radioactivity at the tumor-site was observed (1.1% ID/g). Nonetheless, increasing the dose of the DIBAC-NPs (250 μg , 30 nmol of DIBAC) resulted in a higher tumor uptake (1.4% ID/g). Specific tumor binding was verified by comparing the biodistribution of ^{18}F -labeled azide **4** in non-pretreated mice, in which no considerable accumulation of radioactivity in the tumors was observed (Fig. 19B and C) [105].

This study by Lee et al. was the first successful *in vivo* demonstration of the SPAAC in pretargeted nuclear imaging. Interestingly, in the same year van den Bosch et al. also evaluated the feasibility of the SPAAC *in vivo*, more specifically in the blood stream of mice. In this study a mAb targeting vector (rituximab) functionalized with azides was used in pair with different radiolabeled cyclooctynes as secondary imaging agents.⁸ The cycloaddition was demonstrated *in vitro* in PBS, yet it was unsuccessful *in vivo*. Based on these results, and in contrast to the results from Lee et al., van den Bosch and colleagues made the conclusion that the SPAAC is not appropriate for pretargeted nuclear imaging because of the low concentrations of both the secondary imaging agent as well as the tags attached to the targeting vector. The limited reaction kinetics of the

SPAAC and the serum interaction of the secondary imaging agent was used as an explanation for the observed results [194].

A possible explanation for the conflicting conclusions made could be the number of accessible reactive tags in each study. Indeed, a similar dose of reactive tags was administered in both studies. However, the number of accessible tags will most likely differ since different primary targeting agents with different pharmacokinetics were used as well as a different experimental set-up [103]. Van den Bosch et al. used the SPAAC in order to perform *in vivo* click chemistry in the blood stream at relatively low concentration of reactive tags (18.5 μM). The secondary imaging agent was administered shortly (5 min) after the injection of the azide-functionalized mAb [194]. In contrast, Lee et al. used the SPAAC to proceed at the tumor-site for pretargeted imaging 24 h after the administration of the functionalized NPs. As a consequence, the local concentration of reactive tags is probably higher in this approach. Unfortunately, the local tag concentration has not been determined by Lee and colleagues [105], therefore any conclusions are speculative. On the other hand, the NP dose-dependent tumor uptake reported by Lee et al. supports the theory that higher local concentration of reactive tags increases the probability for the SPAAC to occur in an *in vivo* setting [103]. However, a thorough investigation of this hypothesis has not been reported so far.

In 2018, the SPAAC was successfully used for another pretargeting strategy using a slightly different approach. A DIBO-

⁸ The applied approach is vice versa compared to the SPAAC used by Lee and colleagues.

functionalized anti-CD20 mAb (α -CD20) tumor-targeting component and a multi-azide functionalized dendrimer radiolabeled with yttrium-90 was used. The mAb was injected 24 h prior to the radiolabeled dendrimer. Interestingly, the second order rate constants for each single azide within the dendrimer ($k_2 = 232 \text{ M}^{-1} \text{ s}^{-1}$) was increased more than 100 times compared to its small molecule analog ($k_2 = 2.1 \text{ M}^{-1} \text{ s}^{-1}$). This rate constant increase as well as the increased concentration of azides could be responsible for the possibility to use the SPAAC for pretargeting approaches [196].

3.3.2.2. The tetrazine ligation. Another and even more powerful bioorthogonal reaction is the tetrazine ligation [177,197–199]. Compared to the SPAAC, the tetrazine ligation shows superior reaction kinetics, where impressive rate constants up to $10^{6-7} \text{ M}^{-1} \text{ s}^{-1}$ have been reported [200–202].

In addition, the high specificity, the small molecule character and the orthogonality towards biological moieties make this ligation highly interesting for pretargeting approaches *in vivo*. Mechanistically, the tetrazine ligation consists of two steps. The first step is an enthalpy driven inverse electron-demand Diels-Alder [4 + 2] cycloaddition (IEDDA) between a 1,2,4,5-tetrazine (Tz) and a dienophile (either alkene or alkyne). This cycloaddition is followed by an entropy driven retro Diels-Alder reaction (retro DA), in which nitrogen gas is eliminated and a dihydropyridazine or pyridazine adduct is formed (Fig. 20A) [177].

In contrast to the standard Diels-Alder reaction (DA) reaction, which is a [4 + 2] cycloaddition between an electron rich diene and an electron poor dienophile [203], the IEDDA has diene/dienophile

pairs with opposite electronic character, i.e. an electron poor diene, the Tz, and an electron rich dienophile. In the IEDDA, the Tz and the dienophile interact in a suprafacial fashion (Fig. 20A). The interaction occurs between the four π -electrons of the Tz and the two π -electrons of the dienophile. In accordance with frontier molecular orbital theory, the IEDDA is governed by the energy gap between the HOMO_{Dienophile} (Highest Occupied Molecular Orbital) and the LUMO_{Diene} (Lowest Unoccupied Molecular Orbital). The electron poverty of the diene results in a LUMO at a lower energy level compared to the diene in a normal DA. At the same time the electron richness of the dienophile places its HOMO at a higher energy level. As a consequence, in an IEDDA it is the HOMO of the dienophile that interacts with the LUMO of the diene (Fig. 20B). After the IEDDA, a strained bicyclic ring system is formed, which is rapidly deconstructed by a retro DA reaction driven by the release of nitrogen gas to form, depending on the dienophile used, either pyridazine (alkyne as dienophile) or 4,5-dihydropyridazine (alkene as dienophile) are formed. The latter is isomerized to 1,4-dihydropyridazines (two possible isomers) or oxidized to pyridazine (Fig. 20A) [201,204,205].

3.3.2.2.1. Influencing the reaction kinetics of the tetrazine ligation. The rate determining step of the tetrazine ligation is the actual IEDDA. By influencing the energy gap between the HOMO_{Dienophile} and the LUMO_{Diene}, the reaction kinetics for the ligation can be altered. The smaller the energy gap is the faster the IEDDA will be. Thus, when the Tz-scaffold is substituted with EWG, the LUMO_{Diene} will be at a lower energy level, which results in a more reactive compound and faster reaction rates in the cycloaddition with a dienophile [204–207]. However, with increasing reactivity towards

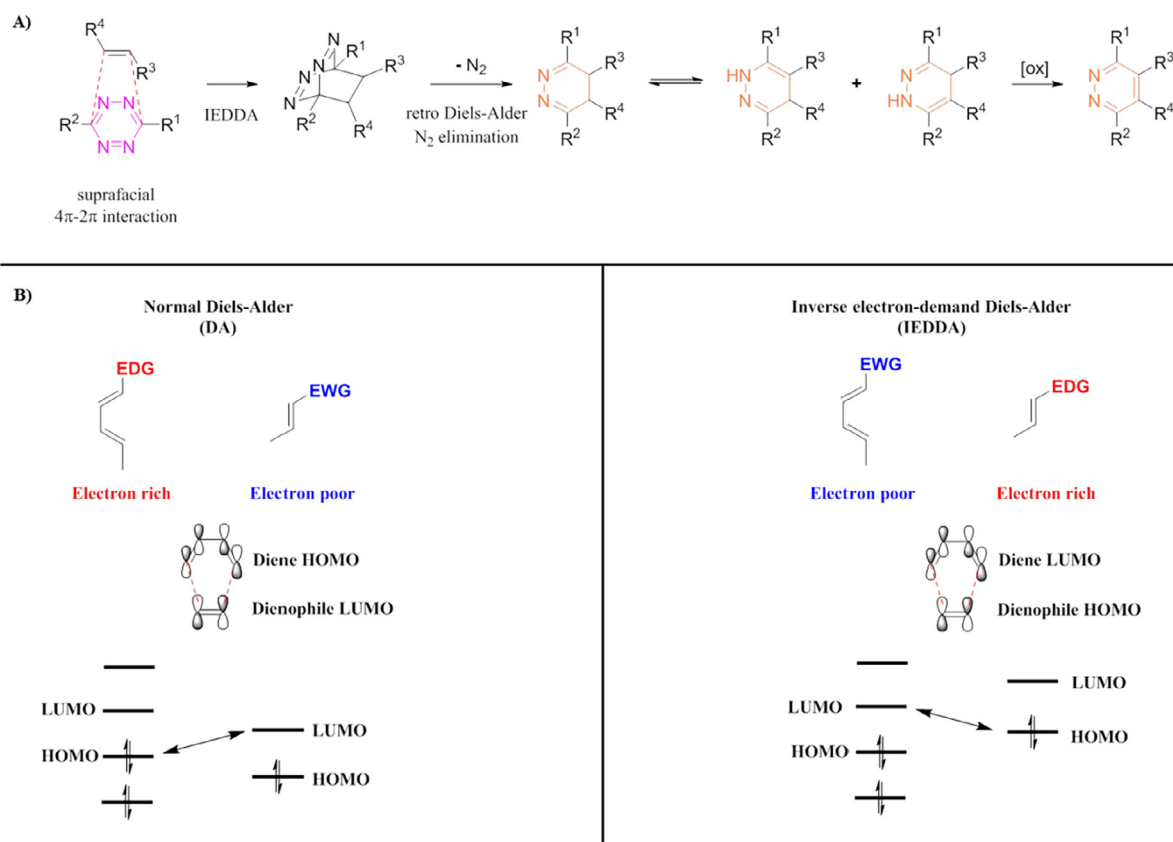


Fig. 20. (A) The tetrazine ligation, consisting of an inverse electron-demand Diels-Alder [4 + 2] cycloaddition (IEDDA) between a tetrazine (Tz) and a dienophile, followed by a second step consisting of a retro Diels-Alder reaction (retro-DA). (B) Frontier molecular orbital theory for a normal Diels-Alder reaction (DA) and the IEDDA. Abbreviations: EDG, electron donating group; EWG, electron withdrawing group. HOMO = Highest Occupied Molecular Orbital, LUMO (Lowest Unoccupied Molecular Orbital).

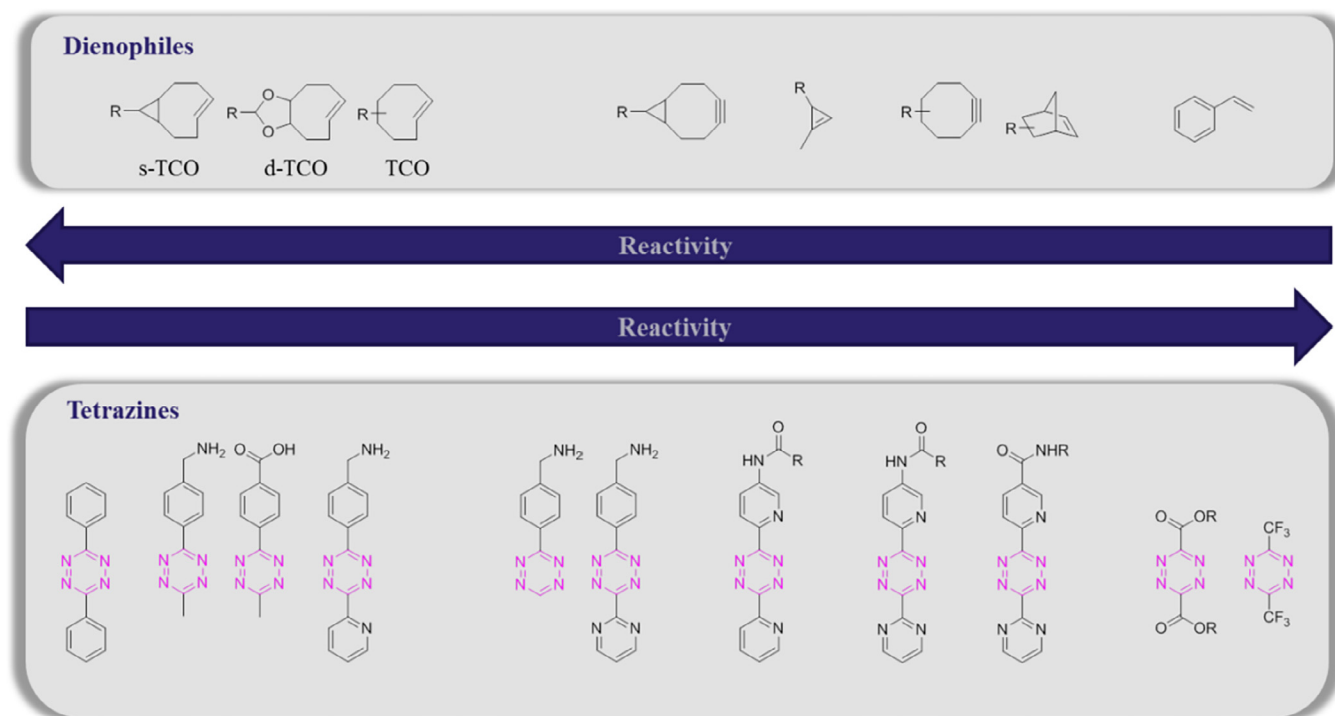


Fig. 21. General reactivity influence among TCOs and Tz-derivatives.

the dienophile a decrease in stability of the Tz is usually observed *in vivo*. The most reactive Tz-derivatives e.g. those bearing trifluoromethyl groups are too reactive to be used *in vivo*, whereas scaffolds bearing pyridyl substituents in the 3,6 positions, have shown high rate constants and still applicability for pretargeting strategies *in vivo* [100,201,208]. In addition to the electronic character, steric effects also play an important role, both for the Tz and the dienophile. For instance, a mono-substituted Tz is highly reactive due to less steric hindrance in the interaction with the dienophile [209].

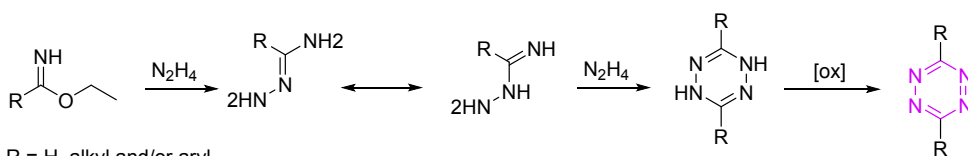
For the dienophile, electron donating groups (EDGs) raises both its HOMO and LUMO to a higher energy level, whereas EWGs will place them on a lower energy level, which tend to alter the reaction to a normal DA instead [198]. Nonetheless, dienophile ring strain appears to have the greatest influence on the reactivity and the most reactive and most frequently used dienophiles are based on *trans*-cyclooctenes (TCO) [177,200,210]. For instance, TCOs with a *cis*-ring fusion with cyclopropane (s-TCO, Fig. 21) are highly reactive, since the eight-membered ring is forced into a strained half-chair conformation [210]. A rate constant of $2.8 \times 10^6 \text{ M}^{-1} \text{ s}^{-1}$ (in PBS) determined with a bis-pyridyl Tz (radiolabeled with lutetium-177) has been reported for s-TCO. Unfortunately, derivatives based on this type of TCOs tend to isomerize to its less stable *cis*-isomer *in vivo* over time, which limits their applications for pretargeting approaches [97,211]. In response to this, Fox and co-workers developed a TCO fused with a dioxolane ring (d-TCO, Fig. 21), which showed better tolerance to physiological conditions and still impressive reaction kinetics with measured rate constants up to $10^5 \text{ M}^{-1} \text{ s}^{-1}$ with bis-pyridyl Tz-derivatives [200]. A general overview of structure – reactivity relationship among Tz-derivatives and various dienophiles is shown in Fig. 21.

3.3.2.2.2. Synthesis of tetrazines. The Tz-framework can be traced back till the end of the 19th century, when Pinner published a synthetic route starting from imidoesters and hydrazine. A subsequent oxidation of the dihydrotetrazine intermediate finally

resulted in the actual Tz-scaffold (Scheme 1A) [212]. Even though the Pinner reaction is still used, the chemistry involving Tz-frameworks has over the years been explored and additional synthetic procedures to access these heterocycles have been reported. For instance, a modified Pinner reaction or a so called “Pinner-like” reaction, in which two nitriles are condensed in the presence of hydrazine, serves as a good alternative to the original procedure (Scheme 1B). Metal- and sulfur mediated versions of this reaction have been reported [213,214]. For the metal-mediated approach, Zn(OTf)₂ and Ni(OTf)₂ have been used. So far, the mechanism of action of the metal ion is uncertain. It has been suggested that the metal ion promotes the reaction by either coordinating to the nitrile and then facilitating the nucleophilic attack by hydrazine, or by coordinating both the nitrile and hydrazine to form a reactive amidrazone intermediate [213]. The proposed mechanism for the sulfur-mediated version involves the formation of a more reactive nucleophile, NH₂NHSH, that later reacts with the nitriles to form an intermediate, which in turn eliminates H₂S while forming dihydrotetrazine [214]. Although, the aforementioned methods have been applied successfully to synthesize both symmetrical and asymmetrical Tz-derivatives, there is still a challenge with asymmetrical Tz-derivatives due to the statistical formation of products using the above described procedures. As such, a sequential synthetic approach was developed. In this approach, 1,2-dichloromethylene hydrazines are first synthesized, then condensed with hydrazine, and finally oxidized (Scheme 1C) [215].⁹ However, the synthetic procedure is not working for all kind of tetrazines. In summary, none of the aforementioned synthetic procedures is preferred over the other. Which procedure to choose depends on the nature of the substituents on the Tz-scaffold.

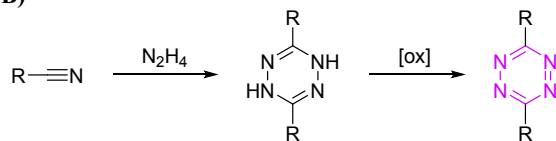
⁹ It is worthwhile to mention that a variety of substituted Tz-derivatives can also be produced via nucleophilic aromatic substitution (S_NAr) starting from an appropriate Tz-scaffold with a leaving group (Scheme 1D and E) [Boeger, D.L. et al. J Org Chem, 1998, 63: 6329–6337].

A)



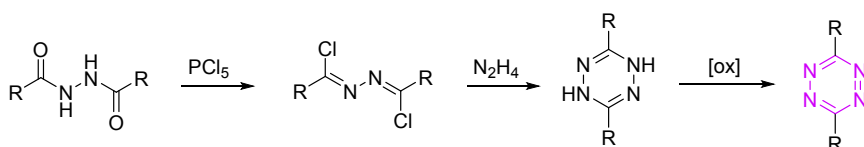
R = H, alkyl and/or aryl

B)

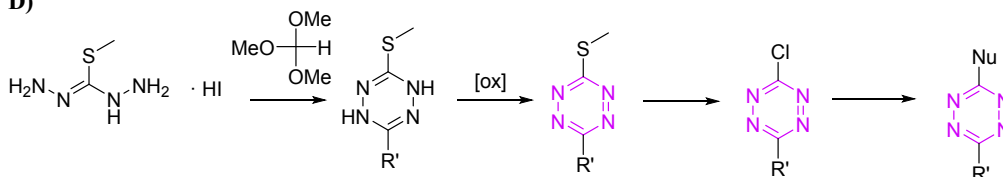


R = alkyl and/or aryl

C)

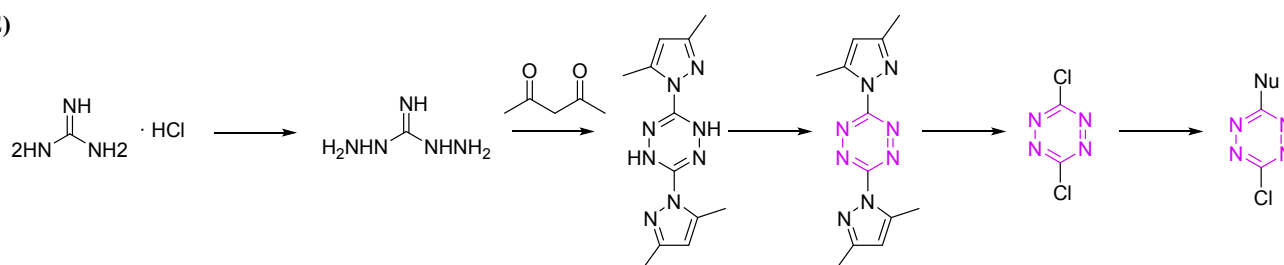


D)



R' = H-, alkyl or aryl

E)



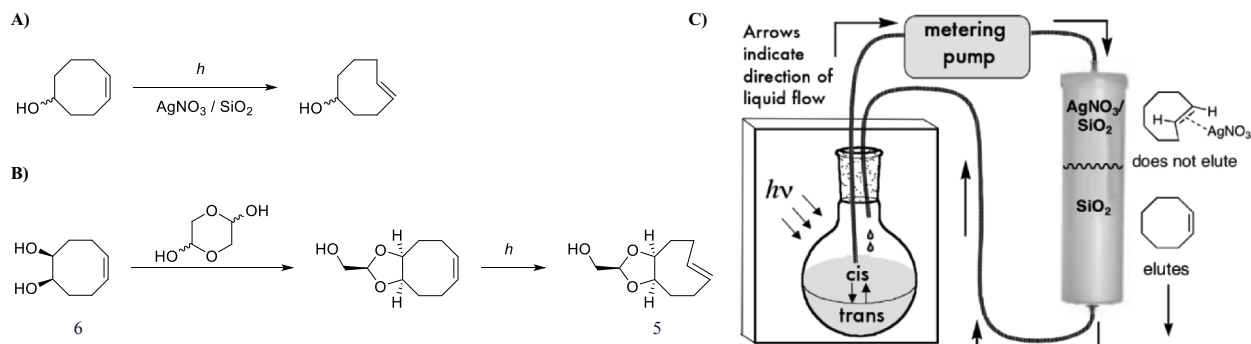
Scheme 1. Synthetic routes towards Tz-derivatives. (A) Pinner reaction. (B) “Pinner-like” reaction. (C) Sequential build-up approach. (D) Nucleophilic aromatic substitution (E) Nucleophilic aromatic substitution.

Finally, it is worthwhile to mention that all aforementioned methods form first a dihydrotetrazine intermediate, which has to be oxidized in order to form the Tz entity. Most commonly employed reagents for the oxidation are 2,3-dichloro-5,6-dicyano-1,4-benzoquinone, (diacetoxyiodo)benzene, chromium trioxide and nitrous reagents (e.g. sodium nitrite and isoamylnitrite) [177,205,216–219]. The latter is not good for Tz-scaffolds bearing sensitive functionalities, such as aromatic amines [177,217].

3.3.2.2.3. *Synthesis of trans-cyclooctenes.* The most frequently applied dienophiles in the tetrazine ligation and the most reactive ones are based on TCO. Fox and colleagues showed in 2008 that TCO can easily be prepared on a large scale from commercially available *cis*-cyclooctene via photoisomerization and continuously passing the mixture through a $\text{AgNO}_3/\text{SiO}_2$ column (Scheme 2A and C). The *trans*-isomer is retained on the column, whereas the *cis*-isomer is not. Instead it is eluted back to the reaction flask for further photoisomerization. Once full conversion to the *trans*-isomer is

achieved, the column is removed and the $\text{AgNO}_3/\text{SiO}_2$ is stirred in NH_4OH . Afterwards, the $\text{AgNO}_3/\text{SiO}_2 - \text{NH}_4\text{OH}$ suspension is extracted to isolate the TCO [220]. The more reactive d-TCO **5** can also be formed on a gram scale, by first reacting (1*R*,2*S*)cyclooct-5-ene-1,2-diol **6** with a glycolaldehyde dimer and subsequent photoisomerization (Scheme 2B) [200].

3.3.2.2.4. *From initial introduction of the tetrazine ligation as a bioorthogonal reaction to early applications and radiolabeling - a brief historical summary.* The tetrazine ligation was introduced as a potential bioorthogonal reaction almost simultaneously by two independent groups in 2008 [177,221]. Already in one of the initially published papers in 2008, the tetrazine ligation was utilized for pretargeted imaging (Fig. 22A). Selective fluorescent imaging of SKBR3 human breast cancer cells succeeded with a norbornene-functionalized trastuzumab mAb targeting the HER2 receptor [222] and a near-IR (near-IR) Tz imaging agent, namely Tz-VT680 **7**. Norbornene and Tz-frameworks undergo ligations with



Scheme 2. (A) Synthetic procedure towards 5-hydroxyl-TCO. (B) Synthetic procedure towards d-TCO. (C) Schematic overview of the photoisomerization set-up. Figure modified from Ref. [220].

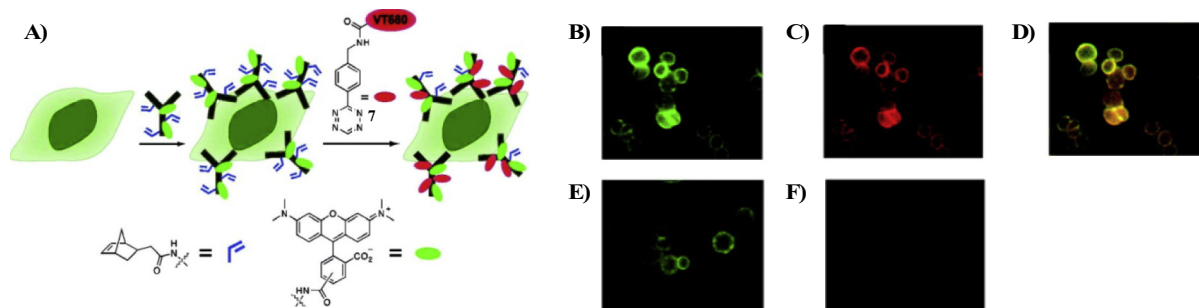


Fig. 22. (A) Pretargeted approach using norbornene- and rhodamine-functionalized trastuzumab and a Tz imaging agent bearing a near-IR probe (VT680). (B) Rhodamine channel (C) Near-IR channel (D) Merged image of both rhodamine and near-IR channel (E) Control experiment, in which trastuzumab functionalized with only rhodamine and no norberene was used (rhodamine channel is shown) (F) Control experiment, in which trastuzumab functionalized with only rhodamine and no norberene was used (near-IR channel is shown). Figure modified from Ref. [221].

rate constants (k_2) in the order of $1.9\text{M}^{-1}\text{s}^{-1}$ in aqueous buffer. Imaging showed perfect alignment between traditional fluorescent imaging of trastuzumab and the near-IR pretargeting approach (Fig. 22B–F) [221]. These promising results rapidly attracted interest in the field of radiopharmaceutical science. Only two years later, in 2010, the first successful pretargeted nuclear imaging with SPECT was reported by Rossin et al. [100]. This pioneering study paved the way for the design and development of various Tz/dienophile pairs for the use in pretargeted diagnostic imaging, but also for pretargeted radiotherapy.

3.3.2.2.5. Pretargeting strategies. In theory, either a Tz-derivative or a TCO moiety can be used to functionalize the targeting vector. The most frequently applied method in nuclear imaging is to functionalize the targeting vector with TCO and radiolabel the Tz counterpart. A reason for this is the differences in the *in vivo* stability of both the Tz and the TCO. The logical approach would be to functionalize the longer circulating primary agent with the most stable of the reactive pairs and use the least stable reactive pair for the faster clearing secondary agent. The stability and reactivity of TCO-functionalized primary targeting agents have been extensively explored. For instance, Rossin et al. have shown that the metabolically unstable TCO moiety [223] can be stabilized when attaching it in close proximity (shorter linkers) to the primary targeting vector. Biological half-lives of up to 6 days were reached using this approach. In contrast free TCO in mouse serum is completely isomerized to *cis*-cyclooctene within 8 h. The *cis*-isomer is not suitable for *in vivo* pretargeting strategies. Rossin et al. could show that the extended biological half-life in the first example comes as a result of shielding the TCO-moiety with the nano-sized targeting agent from Cu-containing enzymes [97]. This shielding

prevents *cis*-*trans*-isomerization that in turn is mediated by Cu-containing enzymes. A similar approach to prolong the biological half-life of Tz-frameworks has so far not been described. Furthermore, highly reactive Tz-derivatives are for example not stable towards cysteine residues. In this respect, we will focus our discussion solely on pretargeting systems that use TCO-functionalized primary targeting agents and Tz-derivatives as secondary imaging agents. Although it should be mentioned that a TCO has been radiolabeled with fluorine-18 [224] and also used in pretargeting strategies [223].

3.3.2.2.6. Preclinical applications

1) Proof-of-principle studies with SPECT

The first successful application of the tetrazine ligation in pretargeted nuclear imaging was published in 2010 by Rossin et al. In this work, a DOTA-functionalized bis-pyridyl Tz labeled with indium-111 (^{111}In]In-DOTA-PEG₁₁-Tz 1) was used as the secondary imaging agent. This probe was applied in combination with a non-internalizing TCO-modified mAb CC49 (CC49-TCO), targeting the tumor-associated glycoprotein 72 (TAG-72) that is expressed by human colon LS174T cancer cells. The CC49-TCO (100 μg , 7.4 TCOs/mAb) was injected *i.v.* into mice bearing LS174T tumors, and after a lag time of 24 h the ^{111}In -labeled Tz (21 μg , 3.4 equiv to TCO, 20–50 MBq) was administered. SPECT/CT imaging showed accumulation in the tumor 3 h after injection and a tumor-to-muscle ratio of 13:1 (Fig. 23A). Non-target tissues, such as liver and blood showed low levels of radioactivity. As negative controls, mice were injected with either CC49 without TCO or TCO-modified rituximab. The latter does not target TAG-72. In both cases, no radioactivity accumulated

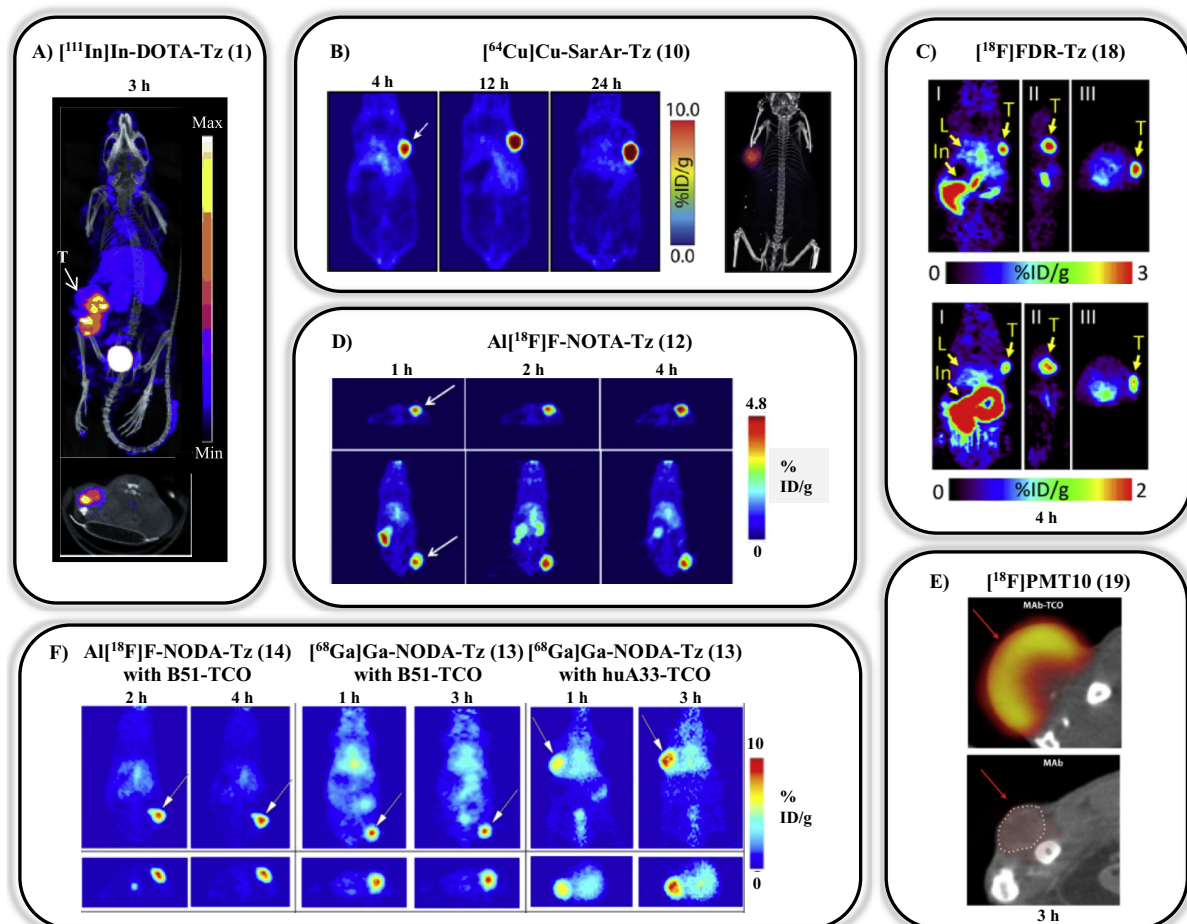


Fig. 23. Pretargeted tumor imaging with various pretargeting systems. (A) SPECT/CT image for CC49-TCO/[^{111}In]In-DOTA-PEG $_{11}$ -Tz **1** system. (B) PET images and PET/CT image for huA33-TCO/[^{64}Cu]Cu-SarAr-Tz **10** system. (C) PET images for Cetuximab-TCO/[^{18}F]FDR-Tz **18** system (top) and Trastuzumab-TCO/[^{18}F]FDR-Tz **18** system (bottom). (D) PET images for 5B1-TCO/Al[^{18}F]F-NOTA-Tz **12** system. (E) PET images for huA33-TCO/[^{18}F]PMT10 **19** system (top) and control experiments with mAb without TCOs and [^{18}F]PMT10 **19** (bottom). (F) PET images for 5B1-TCO with Al[^{18}F]F-NODA-Tz **14** and [^{68}Ga]Ga-NODA-Tz **13** systems, respectively and the huA33-TCO/[^{68}Ga]Ga-NODA-Tz **13** system. The tumors are indicated by an arrow with or without the letter T. Additional abbreviations of organs: In = intestines; L = liver. Figures modified from Refs. [100,106,208,221,225,226].

in the tumors [100].

These promising results encouraged Rossin and colleagues to further optimize the approach [97]. One challenge within any pretargeting strategy is the stability of the reactive tag, i.e. in this case the TCO on the targeting vector. In the pioneering work, the TCO attached to the mAb CC49 was slowly deactivated by *cis-trans*-isomerization with a biological half-life of approx. 3 days. However, a longer biological half-life would allow for longer circulation time of the targeting vector and consequently, for higher target accumulation and improved imaging contrast. In light of that, Rossin et al. investigated if the linker length between CC49 and the TCO was influencing the in vivo stability of the TCO. Shorter linker length improved the stability dramatically (see also section 3.2.6: Pretargeting strategies) [97,227]. Another important aspect of pretargeted imaging is the reactivity of the pretargeting pairs. In respect to this, Rossin and colleagues developed a TCO with improved reaction kinetics in the ligation with Tz-derivatives. Substitution of TCO in the axial position rather than the equatorial position with bulky linkers showed a 10-fold reactivity increase. These two improvements were implemented in the mAb-TCO

design. The optimized mAb¹⁰ was used in pretargeted imaging experiments with ^{111}In -labeled Tz **1** (Table 3). In this study, an increased lag time from 24 h to 72 h was used to reduce the amount of circulating mAbs compared to the original study, resulting in higher target-to-non-target ratios [97,100].

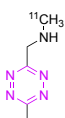
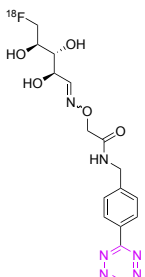
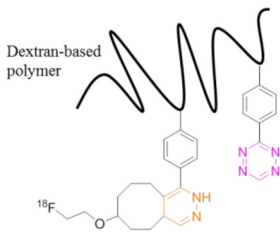
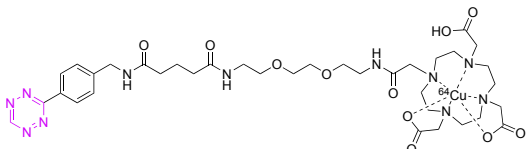
In order to further increase imaging contrast, a clearing agent was applied in the CC49-TCO/[^{111}In]In-DOTA-PEG $_{11}$ -Tz pretargeting strategy. In these experiments, a galactose-albumin construct was functionalized with Tz-derivatives (9–13 Tz-derivatives/albumin galactose) and used to clear free circulating TCO-functionalized mAbs from the blood to the liver [97]. This type of clearing agent has previously shown promise in pretargeting experiments based on the (strept)avidin-biotin interaction [228]. The clearing agent was administered to mice pretreated with CC49-TCO 30 h earlier. After 3 h ^{111}In -labeled Tz **1** (Table 3) was injected. This set-up resulted in more than a 100-fold higher imaging contrast compared to the results from the original study (Fig. 4C) [97].

2) Initial PET studies

After the landmark study by Rossin et al., Lewis et al. extended the pretargeted imaging approach based on the tetrazine ligation from SPECT to PET. His research group used a NOTA-functionalized Tz and labeled it with the PET radionuclide copper-64. This Tz was

¹⁰ The optimized mAb consisted of 10.6 TCOs/mAb. The original consisted of 7.4 TCOs/mAb [Rossin, R. et al., J Nucl Med, 2013, 54: 1989-95] [Rossin, R. et al., Angew Chem Int Ed Engl, 2010, 49: 3375-8].

Table 3 (continued)

Tz	Structure	Reference
16		[230]
17		[107]
18		[106]
19		[221]
20		[104]

applied in the pretargeted imaging of SW1222 human colorectal carcinoma xenografts using a TCO-modified mAb A33 (huA33-TCO, 5 TCOs/mAb) [229]. HuA33 is reported to be persistent towards internalization with a turnover half-life greater than 2 days in vitro [231]. After assessing the tumor accumulation time for the mAb, pretargeting experiments were performed, in which huA33-TCO (100 µg) was administered 24 h prior to i.v. injection of ^{64}Cu -labeled Tz **8** (Table 3) (10.2–12.0 MBq, 1.2–1.4 µg, $A_s = 8.9 \pm 1.2$ MBq/µg). Radioactivity accumulation in the tumor was already seen after 1 h with a value of approx. 4.1% ID/g. Increasing the dose of huA33-TCO to 300 µg resulted in a similar tumor uptake, but higher radioactivity levels in the blood. The latter is likely a result of tetrazine ligation occurring in the blood with the remaining circulating mAb. Even though the pretargeted imaging approach resulted in lower tumor uptake compared to the traditional imaging with directly ^{64}Cu - or ^{89}Zr -labeled huA33, a higher tumor-to-muscle ratio, as well as a lower absorbed radiation burden to non-target tissues were observed in the pretargeting experiments [229].

Unfortunately, the ^{64}Cu -labeled Tz applied in this study cleared through the intestines, which is not optimal when imaging colon cancer. In an attempt to alter the excretion pathway, two new Tz-derivatives were designed with the overall aim to increase polarity and obtain renal clearance. In comparison to the lead compound, the first Tz was designed with a long PEG-linker (7 units)

incorporated between the Tz-scaffold and the NOTA chelator (^{64}Cu]Cu-NOTA-PEG₇-Tz **9**). For the second derivative the NOTA chelator was replaced by a sarcophagine-based chelator (SarAr) (^{64}Cu]Cu-SarAr-Tz **10**, Table 3), which changed the overall charge of the radioligand from -1 to $+2$. Results from biodistribution studies of both Tz-derivatives showed that ^{64}Cu]Cu-SarAr-Tz **10** (Table 3) was the better tracer, with a superior pharmacokinetic profile and pure renal clearance. ^{64}Cu]Cu-NOTA-PEG₇-Tz **9** (Table 3) exhibited clearance via the gastrointestinal and urinary tracts. The reason for the different clearance pathways was suggested to be mainly due to the overall positive net charge of ^{64}Cu]Cu-SarAr-Tz **10** (Table 3) [225]. Despite different pharmacokinetic profiles, both ^{64}Cu]Cu-SarAr-Tz **10** (Table 3) and ^{64}Cu]Cu-NOTA-PEG₇-Tz **9** (Table 3) were successfully applied to pretargeting experiments, in which huA33-TCO (100 µg, 0.66 nmol) was administered 24 h before injection of the Tz-derivatives. Additional non-radioactive Tz was added to the injection solution to adjust the molar ratio to 1:1 with the amount of injected huA33. PET imaging was carried out at time points ranging from 1 to 24 h p.i. of Tz. For ^{64}Cu]Cu-SarAr-Tz **10** (Table 3) the tumor uptake increased over time (from $5.63 \pm 0.67\%$ ID/g 1 h p.i. to $7.38 \pm 2.02\%$ ID/g 24 h p.i.), whereas for ^{64}Cu]Cu-NOTA-PEG₇-Tz **9** (Table 3) the accumulation of radioactivity was roughly the same for all time points ($4.07 \pm 0.25\%$ ID/g 1 h p.i. and $3.94 \pm 0.92\%$ ID/g 24 h p.i.). Further experiments were performed with ^{64}Cu]Cu-SarAr-Tz **10** (Table 3)

allowing longer accumulation time for the mAb; 48 h and 120 h, respectively. However, the highest tumor uptake was observed with the initially used 24 h lag time. This could have been expected since TCOs tend to be deactivated over time by *cis-trans*-isomerization [225].

3) The first pretargeted imaging study using a short-lived radionuclide

As a next step, it was attempted to replace the medium-lived copper-64 with shorter-lived radionuclides in order to exploit the full potential of pretargeted imaging, i.e. maximizing imaging contrast while reducing radiation exposure to healthy tissue. In 2014, Evans et al. reported the radiolabeling of a Tz with gallium-68 (11) (Table 3) and its evaluation in pretargeted experiments [110,232]. For the pretargeted imaging studies cetuximab was modified with TCOs (17 TCOs/mAb) and used as primary targeting agent [110]. Mice bearing EGFR expressing A431 tumor xenografts were pretreated with TCO-modified cetuximab and 23 h later ⁶⁸Ga-labeled Tz 11 (Table 3) (approx. 1.85 MBq) was injected. This resulted in a tumor uptake of 3.48% ID/mL. Experiments with 3 h between injection of mAb and ⁶⁸Ga-labeled Tz 11 (Table 3) were also performed, but a tumor uptake of only 0.86% ID/mL was observed using this setup. Both in the biodistribution of directly radiolabeled mAb and in pretargeting experiments with the Tz, high liver uptakes were observed, which might be a consequence of the high TCO-loading/mAb.¹¹ Biodistribution studies of [⁶⁸Ga]GaCl₃ and ⁶⁸Ga-labeled Tz 11 (Table 3) were performed as negative controls to verify specific tumor uptake in pretargeted imaging experiments [110].

4) PET studies with short-lived, non-radiometal radionuclides

A major drawback with radiometal-based Tz-derivatives is that they are limited to extracellular targets. Current chelator-based structures cannot cross cell membranes. In addition, many nanomaterials and mAbs internalize to some degree, which limits or even in some cases prevents the use of radiometal-labeled Tz-derivatives. In this respect, efforts have been directed towards developing Tz-scaffolds labeled with carbon-11 and fluorine-18. These types of compounds would have the potential to be used for intracellular targets as well. Moreover, carbon-11 and fluorine-18 possess outstanding nuclear imaging properties that result in a relatively low radiation burden and good image contrast compared to standard applied radiometals (Table 1). Carbon-11 easily allows for test-retest experiments within one day with the same test subject. Fluorine-18 offers several advantages, e.g. due to its half-life of 110 min it is optimal for clinical routine applications and commercialization. The half-life also enables multi-step radiosyntheses¹² within business hours and productions as high as 300 GBq. Patient doses are typically 200–400 MBq. Furthermore, the half-life and the achievable fluorine-18 amount allows for centralized production with distribution to other facilities. A transportation range of 200–300 km is certainly possible. However, labeling Tz-derivatives with carbon-11 or fluorine-18 does not come without challenges. Whereas, radiometal-labeling normally proceeds under rather mild conditions, ¹¹C- and ¹⁸F-labeling

require more harsh reaction conditions, which tend to be tedious to apply on the sensitive Tz-framework. Despite these challenges, groups have reported various Tz-derivatives labeled with these radionuclides [106,107,208,216,224,226,230].

Carbon-11

In 2013, the first ¹¹C-labeled Tz 15 (Table 3) was reported [216]. Data from studies in pigs demonstrated that Tz 15 (Table 3) is metabolized rapidly in vivo (26% intact tracer after 10 min), but indication of brain-uptake was observed from PET imaging (summed 6–20 min p.i.). No pretargeted evaluation studies were reported [233]. In 2016, Denk et al. reported another ¹¹C-labeled Tz 16 (Table 3). This Tz was evaluated in female BALB/c mice using two different mesoporous silicon-based NPs modified with either standard TCO (116 μmol/g loading) or s-TCO (119 μmol/g loading). The NPs were labeled via ligation with the ¹¹C-labeled Tz and thereafter administered. Already 5 min p.i. a high uptake in the lungs (18–25 SUV) could be detected. The reason for more or less exclusive lung accumulation is most likely due to aggregation of the NPs (as a result of the high loading of the lipophilic TCOs). Nonetheless, these NPs offered a convenient system for evaluating the new Tz in a pretargeting approach. Hence, for pretargeting experiments, in which the NPs were injected 5 min before administration of the ¹¹C-labeled Tz (15.4 ± 6.0 MBq with a A_m of 10 ± 5.4 GBq/μmol), the accumulation of activity in the lungs turned out to be around 1.5 SUV for s-TCO-NPs and approx. 2.5 SUV for TCO-NPs after 40–60 min dynamic PET scanning. The lower uptake for the s-TCO-NPs might relate to the lower stability of s-TCOs in vivo. For both types of NPs, a similar molar amount of dienophile was injected, 59 nmol of s-TCO in a 0.5 mg portion of NPs and 58 nmol of standard TCO in a 0.5 mg portion of NPs, respectively [230].

Fluorine-18

Fluorine-18 is considered to be the gold standard among PET radionuclides for clinical routine studies [234]. As a result, a Tz labeled with fluorine-18 has attracted great interest among several research groups.

a) Direct labeling approaches

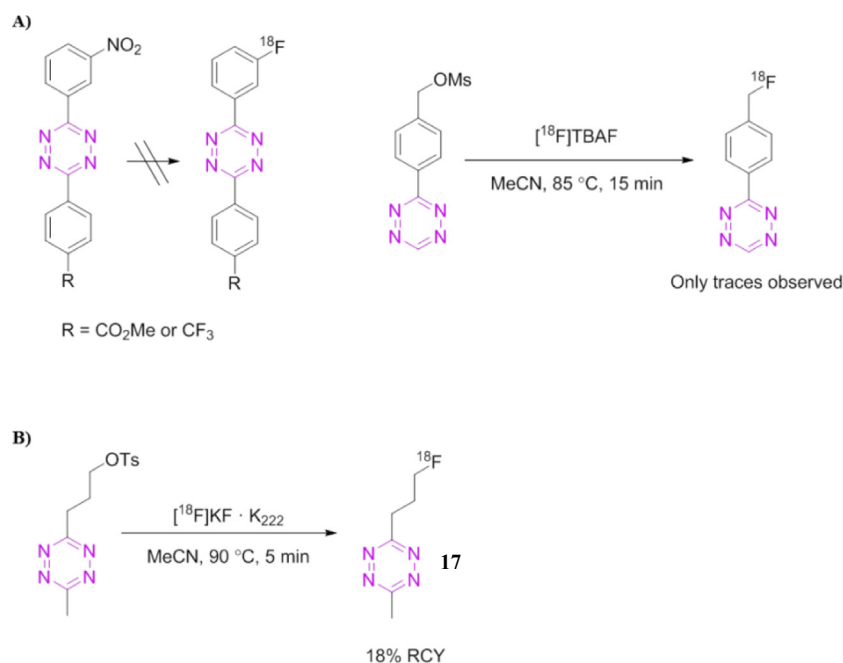
In 2010, Li et al. tried to radiolabel three different Tz-derivatives with fluorine-18 applying standard direct ¹⁸F-fluorination conditions (Scheme 3A). However, the Tz-framework decomposed and only traces of the ¹⁸F-labeled product could be observed. The use of nucleophilic bases and the relatively high temperatures applied for standard ¹⁸F-fluorination are not well-tolerated for sensitive Tz-scaffolds [224]. This was nicely shown by Denk et al., who found that the tolerance towards standard ¹⁸F-fluorination increased with decreasing reactivity of the Tz-scaffold. Accordingly, direct ¹⁸F-labeling of a less reactive (compared to the Tz-derivatives used by Li et al.) bis-alkyl substituted Tz 17 (Table 3) succeeded in a radiochemical yield (RCY) of 18% (Scheme 3B) [107].

Biodistribution studies of this ¹⁸F-labeled Tz in female BALB/c mice indicated blood-brain-barrier permeability and renal clearance of the tracer. No accumulation of radioactivity in the bones was observed, indicating in vivo defluorination did not occur. Moreover, in vivo stability assessments were performed from plasma collected 2 h p.i. of the Tz. These showed that the Tz exhibited a low degree of metabolic degradation, approx. 15%. No pretargeted imaging experiments were reported, but the ligation to a TCO was tested in vivo and analysis by radio-TLC showed more than 90% conversion to the ligation adduct after only 5 min. A promising result for future evaluation in pretargeted imaging studies [107].

b) Indirect labeling approaches

¹¹ The authors claim that the high levels of activity in the liver are characteristic with the pharmacokinetic profile of mAbs [Evans et al., Chem. Commun., 2014, 50: 9557–60].

¹² As a rule of thumb, the production of a PET tracer should not take longer than 4 h and the synthesis should be carried out within three half-lives of the respective nuclide.



Scheme 3. Direct ¹⁸F-fluorination of Tz-derivatives. (A) Early attempts by Li et al. (B) Successful ¹⁸F-fluorination of a bis-alkyl Tz.

To our knowledge, no direct ¹⁸F-fluorinations of highly reactive Tz derivatives, such as bis-pyridyl or mono-substituted scaffolds have been reported so far. Instead, indirect ¹⁸F-fluorination serves as a valuable labeling strategy for highly reactive Tz-frameworks. In such a strategy, a synthon is first labeled with fluorine-18 and thereafter attached to the Tz of interest. Thereby, the Tz is not exposed to the harsh conditions applied in standard ¹⁸F-fluorination. This type of approach was used in 2016 by Keinänen et al. In their work, an aminoxy-functionalized Tz precursor was coupled to 5-[¹⁸F]fluoro-5-deoxyribose ([¹⁸F]FDR)¹³ via oxime coupling. The product, ¹⁸F-labeled Tz **18** (Table 3) was highly hydrophilic and showed promising reaction kinetics in the ligation with TCO in plasma ($k_2 = 4500 \text{ M}^{-1} \text{ s}^{-1}$) [235]. In a follow-up study, this Tz was evaluated in healthy mice in pretargeted imaging of non-targeting TCO-NPs. In these experiments, TCO-NPs (0.2 mg with 1.42 nmol of TCO) were injected 15 min prior to i.v. injection of the Tz ($5.9 \pm 0.5 \text{ MBq}$, $0.17\text{--}0.19 \text{ nmol}$, $A_m = 22.2\text{--}40.2 \text{ GBq}/\mu\text{mol}$) [106]. The used non-targeting NPs are known to rapidly clear from the blood stream in healthy animals via the mononuclear phagocytic system, e.g. spleen and liver [236]. Therefore, a considerable amount of radioactivity in the pretargeting studies was observed in the spleen ($10.4 \pm 2.3 \text{ ID/g}$ 30 min p.i. of Tz) and in the liver ($15.8 \pm 4.6 \text{ ID/g}$ 30 min p.i. of Tz). Untreated mice (without prior injection of TCO-NPs) showed a Tz accumulation of only $1.9 \pm 0.4 \text{ ID/g}$ in the spleen at the same time point. In addition, high accumulation of radioactivity was observed in the lungs ($13.9 \pm 5.3 \text{ ID/g}$ 30 min p.i. of Tz) [106], probably due to aggregation of the NPs. A phenomenon also observed in previous studies with TCO-NPs [230]. Extending the lag time to 24 h in the pretargeting experiments did not result in any tetrazine ligation in vivo, which the authors suggest is due to the poor stability of the TCOs [106].

Encouraged by these results, ¹⁸F-labeled Tz **18** (Table 3) was evaluated in pretargeting experiments using the TCO-modified internalizing mAbs, cetuximab and trastuzumab. As previously

mentioned, cetuximab binds to the EGFR [237] and trastuzumab targets the HER2-receptor [222]. In order to determine the optimal imaging time-point for the pretargeting studies, both mAbs were radiolabeled with zirconium-89. Tumor accumulation occurred already after 24 h, but good clearance from non-target tissues was not detected until 72 h p.i. In this respect, 72 h was considered to be an appropriate period of time for target accumulation in the pretargeting imaging experiments. However, earlier time points were also investigated (24 h and 48 h for cetuximab, and 48 h for trastuzumab). The degree of functionalization was for the cetuximab $6.1 \pm 0.1 \text{ TCOs/mAb}$, whereas the trastuzumab was modified with $4.9 \pm 0.1 \text{ TCOs/mAb}$ [238].

In initial pretargeting studies with high molar activity (A_m) ($15\text{--}38 \text{ GBq}/\mu\text{mol}$), no significant tumor uptake was observed. This was suggested to be a result of tetrazine ligation occurring with remaining circulating mAbs and therefore, lower A_m was explored. Here, non-radioactive Tz was added to get a 1:1 M ratio with regard to the molar amount of TCO on the injected mAbs. Two different groups of mice were used. Group A was injected with ¹⁸F-labeled Tz diluted with the same molar amount of non-radioactive Tz, whereas Group B received the non-radioactive Tz (same amount used as for Group A) 5 min prior to injection of the ¹⁸F-labeled Tz (same A_m used as for Group A). The following conditions were used in this set-up. Trastuzumab-TCO ($20 \mu\text{g}$, 0.13 nmol , 0.65 nmol of TCO) was injected into BT474 tumor-bearing mice and cetuximab-TCO ($75 \mu\text{g}$, 0.5 nmol , 3.1 nmol of TCO) was administered into A431 tumor-bearing mice. In general, approx. 16–22 MBq was injected of the ¹⁸F-labeled Tz **18** (Table 3) and the molar ratio was adjusted with non-radioactive Tz. For experiments with cetuximab 1.39 equiv. of ¹⁸F-labeled Tz **18** (Table 3) were used in regard to the molar amount of injected TCO, whereas for trastuzumab approx. two equiv. of **18** (Table 3) were used. With this set-up tumor uptake was observed and PET imaging revealed that the tumor uptake remained constant over time for both mAbs, while the background decreased. No significant difference was observed for the tumor uptake between the two groups of mice (A and B) for both targets. The highest tumor uptake for cetuximab was observed with 72 h lag time between mAb and ¹⁸F-labeled Tz injection ($3.54 \pm 0.45 \%$

¹³ [¹⁸F]FDR can easily be labeled in RCY of 60% (d.c.) [Li et al., Nature protocols, 2014, 9: 138–145].

ID/g for group A and $3.70 \pm 0.13\%$ ID/g for group B). For trastuzumab, there was no observable difference in tumor uptake between the 48 h and 72 h lag time. PET images 4 h p.i. of Tz for both mAbs is shown in Fig. 23C. Controls with non-specific uptake were performed as well [238].

Even though, tumor uptake was observed for both cetuximab and trastuzumab, it was much lower than the uptake in corresponding conventional imaging experiments with zirconium-89. The reason for the low levels of radioactivity accumulation in the tumors for the pretargeting experiments might be explained by the fact that a non-internalizing Tz was used. It is likely that **18** (Table 3) can only react with the small number of mAbs that have not yet internalized [238]. Since, internalizing mAbs are an important class of vectors for diagnosis and therapy, the development of ^{18}F -labeled Tz-derivatives, that are able to cross cell membranes and can be used as a pretargeting pair, is still ongoing.

5) Miscellaneous

a) Radiometal-like labeling with $\text{Al}[^{18}\text{F}]\text{F}$

Another possibility to obtain ^{18}F -labeled Tz-derivatives in an efficient way, while avoiding basic labeling conditions, is to radiolabel with $\text{Al}[^{18}\text{F}]\text{F}$. Al^{3+} forms strong bonds to F^- , in fact stronger than to most other metal ions [239]. $\text{Al}[^{18}\text{F}]\text{F}$ -labeling can be performed with chelators such as NOTA, NODA, NODAGA and RESCA [226,240,241]. One drawback using this chelator labeling strategy is that the produced secondary imaging agent is most likely limited to extracellular targets. So far, almost all chelator-based structures cannot cross cell membranes.

In 2016, Lewis and co-workers reported the first $\text{Al}[^{18}\text{F}]\text{F}$ -NOTA-labeling of a Tz-scaffold **12** (Table 3). This Tz was evaluated with a TCO-modified mAb, 5B1 (5B1-TCO), that targets the carbohydrate antigen 19.9 (CA19.9), which is a biomarker for pancreatic ductal adenocarcinoma. The number of TCOs/mAb was not reported. For the pretargeted PET studies, 5B1-TCO (1.33 nmol) was administered, followed by a lag time of 72 h before an equimolar amount of Tz **12** (Table 3) (1.33 nmol, 18–20 MBq) was injected. PET/CT imaging was carried out at 1 h, 2 h and 4 h p.i., respectively. The tumor uptake increased over time (Fig. 23D) and at the 4 h time point the radioactivity levels in the tumor were 6.4% ID/g. The plasma half-life of the Tz was rather long (71.2 ± 5.40 min), which might be an explanation to the increasing tumor uptake over time [226]. Alternatively, still circulating 5B1-TCO that react with the radiolabeled Tz in the blood pool and then accumulate at the tumor-site might also explain the increasing tumor uptake.

b) The influence of charge and linker on the pharmacokinetic profile of Tz-derivatives

The straightforward approach using $\text{Al}[^{18}\text{F}]\text{F}$ to easily access ^{18}F -labeled Tz-derivatives and the possibility to radiolabel the same moieties with gallium-68 prompted, Lewis, Zeglis and co-workers to investigate the relationship between pharmacokinetics and Tz-structure in terms of different substituents, linkers and chelators (Fig. 24). In total, four different Tz-scaffolds were used to access 25 different Tz-derivatives radiolabeled with either fluorine-18 or gallium-68. Properties and parameters such as lipophilicity ($\log D_{7.4}$), in vivo stability, plasma half-life and biodistribution were determined. On the basis of these results, 15 Tz-derivatives were selected for pretargeting experiments. The selected group was thought to cover a wide range of diversity in structure and physicochemical properties of the compounds. However, attributes such as clearance (preferably renal) and plasma half-life had major

influence on the decision. The pretargeted imaging experiments were performed using the same procedure described earlier, with 5B1-TCO as a primary targeting agent (see section 5. Miscellaneous – Radiometal-like labeling with $\text{Al}[^{18}\text{F}]\text{F}$). A few trends in the relationship between structure and in vivo behavior among all the Tz-derivatives studied could be identified. Firstly, the overall net charge influenced its clearing pathway. A positive charge reduced the lipophilicity of the radioligand and induced clearance through the kidneys, whereas compounds with no charge were mainly excreted via the liver and intestines. This conclusion arose from the observation that the only structural difference between $[^{68}\text{Ga}]\text{Ga-NODA-Tz}$ **13** (Table 3) and $\text{Al}[^{18}\text{F}]\text{F-NODA-Tz}$ **14** (Table 3) arrived from the radionuclide used. $[^{68}\text{Ga}]\text{Ga-NODA-Tz}$ **13** resulted in a charge of +1 and $\text{Al}[^{18}\text{F}]\text{F-NODA-Tz}$ **14** (Table 3) in a charge of 0. Secondly, the choice of linker between the chelator and the Tz-scaffold had an impact. Amino acid linkers generally reduced the circulation time in the blood stream, as well as induced predominant clearance via the hepatic system. Finally, the plasma half-life of the Tz affected the tumor accumulation and was suggested to preferably exceed 10 min for good tumor accumulation in pretargeting experiments [208].

Two promising lead compounds could be identified in this study, namely $\text{Al}[^{18}\text{F}]\text{F-NODA-Tz}$ **14** (Table 3) and $[^{68}\text{Ga}]\text{Ga-NODA-Tz}$ **13** (Table 3). They showed good stability, sufficient plasma half-life (17.1 min and 15.1 min, respectively) and high tumor uptake. PET images with $\text{Al}[^{18}\text{F}]\text{F-NODA-Tz}$ **14** (Table 3), showed a tumor uptake of $7.6 \pm 1.8\%$ ID/g 2 h p.i. and imaging after 4 h showed an uptake of $8.8 \pm 1.7\%$ ID/g (Fig. 23F). The ^{68}Ga -labeled Tz **13** (Table 3) had a tumor uptake of $6.8 \pm 1.4\%$ ID/g 2 h p.i. and $7.1 \pm 1.8\%$ ID/g 4 h p.i. (Fig. 23F). The ratios between target and non-target tissues were promising for both **13** and **14** (Table 3) [208].

Based on ex vivo biodistribution, the whole-body effective doses of the pretargeting studies of the two new Tz-derivatives were compared with the doses of the conventional approach, in which the mAb was directly labeled with zirconium-89. The conventional approach resulted in a 70-fold higher radiation dose in healthy tissues. Finally, the clearance profile of both Tz was compared. The ^{68}Ga -labeled derivative **13** (Table 3) displayed a better clearance profile for imaging purposes, mainly renal, while $\text{Al}[^{18}\text{F}]\text{F-NODA-Tz}$ **14** (Table 3) showed excretion via the liver and intestines. As a result of this, only additional studies were performed with $[^{68}\text{Ga}]\text{Ga-NODA-Tz}$ **13** (Table 3) in mice with colorectal cancer xenografts using huA33-TCO as a targeting vector with a 48 h lag time before administration of Tz. In these experiments, **13** (Table 3) exhibited a tumor uptake of $7.7 \pm 1.1\%$ ID/g 4 h p.i. (Fig. 23F). [208].

c) Polymer-based labeling with fluorine-18 and gallium-68

In 2012, Devaraj et al. reported a Tz-coated polymer ($[^{18}\text{F}]\text{PMT10}$ **19**, (Table 3)), which could be radiolabeled with fluorine-18 and be used as a secondary imaging agent. The polymer was based on an amino-dextran (10 kDa) backbone functionalized with one fluorochrome and mono-substituted Tz-derivatives (approximately 2 Tz-derivatives/polymer). A larger polymer (40 kDa) with a higher degree of functionalization (11 Tz-derivatives/polymer) was also synthesized, but not used in pretargeting studies. Radiolabeling was achieved by indirect ^{18}F -fluorination via ligation to (*E*)-5-(2- $[^{18}\text{F}]\text{fluoroethoxy}$)cyclooct-1-ene in a RCY (decay corrected) of 89% [242]. Pretargeted imaging experiments with $[^{18}\text{F}]\text{PMT10}$ **19** (Table 3) were conducted in LS174T human colon cancer bearing mice using the mAb huA33 as a targeting vector, which was functionalized with TCOs (approx. 3 TCOs/mAb) and a near-IR probe (VT-680). The huA33-TCO-VT680 (30 μg) was administered 24 h prior to i.v. injection of $[^{18}\text{F}]\text{PMT10}$ **19** (Table 3) (30 μg , 5.55 MBq). PET/CT images 3 h p.i. of the Tz-coated polymer showed

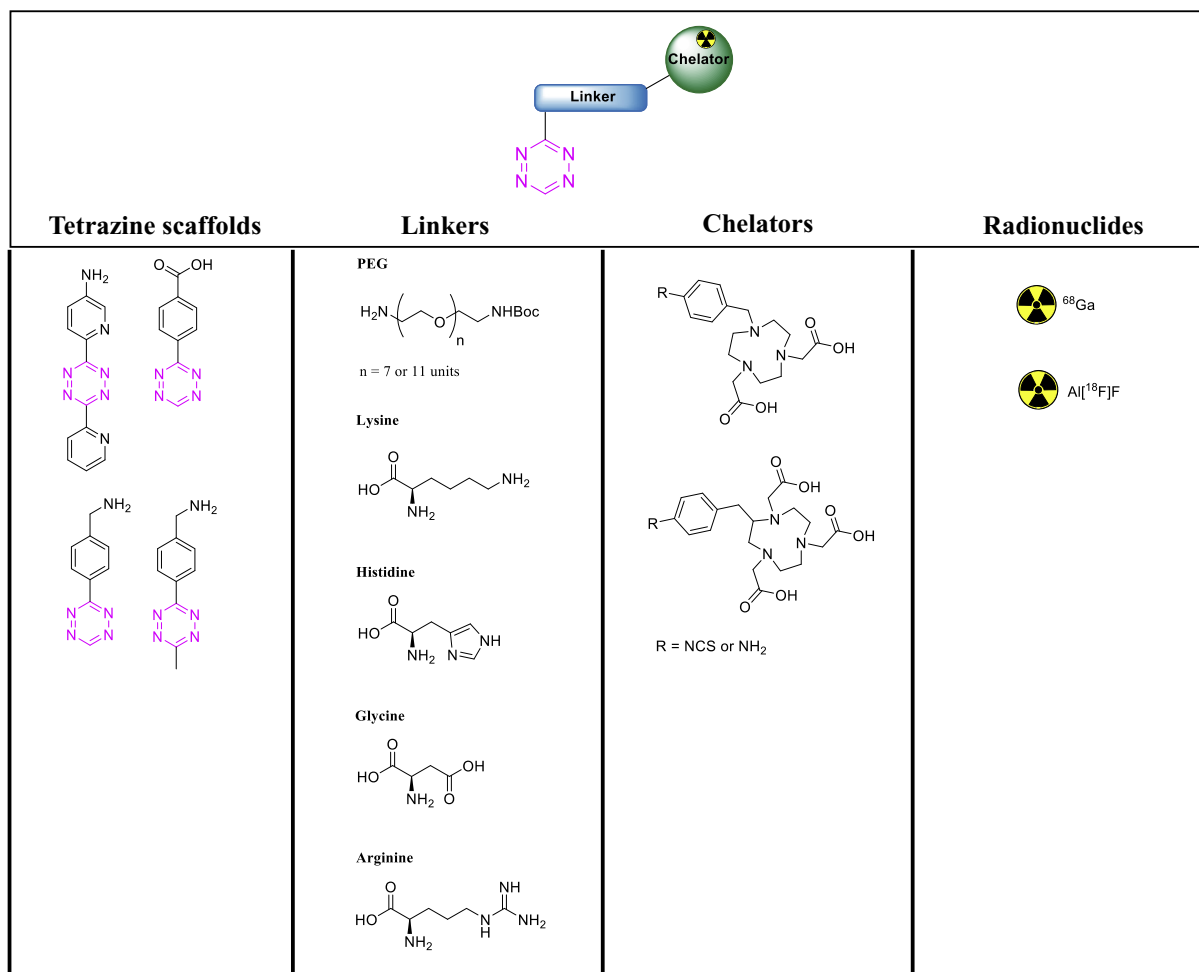


Fig. 24. Building blocks for the library of Tz-derivatives used to investigate the relationship between structure and in vivo behavior in pretargeting strategies. Abbreviations: NCS = N-Chlorosuccinimide.

accumulation of radioactivity in the tumor (Fig. 23E). Unfortunately, no values for the tumor uptake were given and no information about the distribution of the radioactivity in non-target tissues was reported. However, negative control experiments were performed, in which mice received mAb without any TCOs. In these controls, no accumulation of radioactivity was observed in the tumor (Fig. 23E) [242].

Two years later, in 2014, Devaraj and coworkers also reported a ^{68}Ga -labeled Tz-coated polymer based on the same amino-dextran backbone. Since ^{68}Ga -labeling requires chelating chemistry, the polymer was functionalized with the chelator DTPA before amide coupling to an NHS-functionalized Tz. The radiolabeled polymer was evaluated with a similar pretargeting procedure as the ^{18}F -version, although the huA33-TCO had a higher loading of TCOs (5.3 TCOs/mAb versus 3 TCOs/mAb in previous set-up). The tumor-to-muscle ratio was 3.9 ± 1.8 [243].

3.3.2.2.7. *Application to tumor-targeting nanomaterials in cancer.* To date, the only reported pretargeted tumor imaging applying the tetrazine ligation with other targeting vectors than mAbs is Lin and co-worker's strategy using supramolecular TCO-functionalized NPs along with ^{64}Cu -labeled DOTA-Tz **20** (Table 3). The NPs were formed by self-assembly of a TCO-grafted cyclodextrin-polyethyleneimine polymer, a cyclodextrin-polyethyleneimine polymer, an adamantane-grafted polyamidoamine and an adamantane-grafted polyethylene glycol. For pretargeting studies, the TCO-NPs

(100 μg , 1 nmol of TCO) with a size of 100 nm were injected i.v. into mice bearing U87 glioblastoma tumor xenografts. The TCO-NPs targeted the tumor via the EPR effect, and after a 24 h lag time ^{64}Cu -labeled Tz **20** (Table 3) (10 nmol of Tz, 11.0 MBq) was administered. PET/CT images 24 h p.i. of the Tz showed accumulation of radioactivity in the tumor (Fig. 25A) and the ex vivo biodistribution revealed a tumor uptake value of 16% ID/g (Fig. 22C). For non-target tissues (Fig. 25C and D), a high uptake in the liver (17% ID/g) was observed. Control experiments, including conventional imaging of the ^{64}Cu -labeled TCO-NPs showed the same result; high liver uptake (Fig. 25B, C and D). In contrast, the biodistribution of the [^{64}Cu]

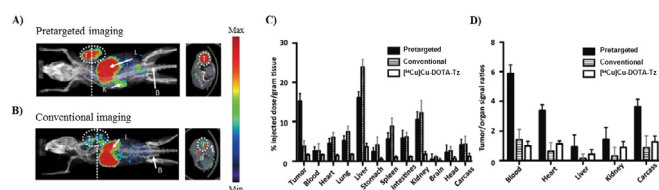


Fig. 25. (A) Pretargeted PET imaging using TCO-NPs injected 24 prior to administration of [^{64}Cu]Cu-DOTA-Tz **20**. (B) Conventional imaging of [^{64}Cu]Cu-TCO-NPs. (C) Ex vivo biodistribution from pretargeting experiments, the conventional approach (^{64}Cu -labeled TCO-NPs) and biodistribution of [^{64}Cu]Cu-DOTA-Tz **20**. (D) Ratios between tumor and non-target tissues for all three experiments. Figure modified from Ref. [104].

Cu-DOTA-Tz **20** (Table 3) did not show significant accumulation of radioactivity in the liver [104]. Since the amount of radioactivity in the blood was almost the same for all three experiments (pre-targeting approach, conventional approach and biodistribution of Tz), a reason for the high liver uptake in the pretargeting experiments might be that the tetrazine ligation occurred with TCO-NPs accumulated in the liver.

3.3.2.2.8. *Concluding remarks – tetrazine ligation.* To date, the tetrazine ligation is the most promising bioorthogonal reaction in rodents. So far, it has not been applied in clinical studies. Several promising Tz-based PET tracers have been developed. For instance, ⁶⁸Ga-labeled Tz **13** (Table 3) reported by Lewis and colleagues has shown applicability in imaging of pancreatic ductal adenocarcinoma as well as colorectal cancer in mice. Furthermore, among the Tz-derivatives radiolabeled with non-radiometals, ¹⁸F-labeled Tz **18** (Table 3) seems to be the most promising candidate at the moment. It is yet to be shown if one of these tracers will be successful in pretargeted imaging in patients.

4. The potential of pretargeting for radiotherapy based on non-targeted nanomedicines

Radionuclide therapy is a powerful tool in oncology and has shown promise in treating cancer patients with prostate cancer, lymphomas, leukaemias, non-Hodgkin's lymphomas or somatostatin-receptor expressing tumors [244]. It is based on the use of therapeutic radionuclides (typically emitting β^- or α -particles) that are attached to a tumor targeting vector. After accumulation at the target-site, high cytotoxic radiation levels are delivered, which ultimately kill the cancer cells [245]. One significant advantage of radionuclide therapy compared to conventional chemotherapy is the possibility to determine the optimal dose before therapy and to monitor therapy efficacy via molecular imaging techniques. Therefore, radionuclide therapy results in an increased precision and may reduce side effects in patients [244]. One highly selective and specific form of radiotherapy exploits mAbs as carriers for therapeutic radionuclides. It is called radioimmunotherapy (RIT) and has especially shown success in lymphomas and leukaemias [246]. However, therapeutic dose levels that can be applied in RIT are limited by the radionuclide dilemma (Fig. 3). Long-lived radionuclides have to be used to be compatible with the slow accumulation and excretion process of mAbs. Consequently, also healthy tissues are irradiated to a great extent, which is a major concern regarding organs that are sensitive to radiation, such as the bone marrow and the kidneys [245]. The same considerations are also valid for NP-based radionuclide therapies. Since pretargeting strategies circumvents the radionuclide dilemma, pretargeted radiotherapy (PRT) can be applied to increase radiation dose to diseased tissue and to reduce toxicity to

healthy tissue [247]. Not many studies applying PRT have been performed so far. In the following section, different strategies for PRT will be described and the potential of the tetrazine ligation for this purpose will be discussed.

4.1. Radionuclides for targeted radiotherapy

As for imaging purposes, there are a set of radionuclides accessible that can be used for pretargeted radiotherapy (Table 4). One key nuclear property is the maximum range of the emitted particle that is used for therapeutic purposes. Several reviews have been published discussing the therapeutic potential and use of these radionuclides [248].

4.2. Pretargeted radiotherapy (PRT)

4.2.1. Non-tetrazine ligation-based studies

Encouraged by the outstanding imaging contrast observed for mAb pretargeted imaging, most PRT strategies have focused on antibody conjugates. For example, PRT was applied clinically using an ¹³¹I-labeled hapten and a bsAb. The bsAb targeted the carcinoembryonic antigen in patients with non-medullary thyroid carcinoma (non-MTC) or medullary thyroid carcinoma (MTC). During the study 70% of the lesions were detected and treated, yet some liver toxicity was observed. After the study tumor stabilization was present in 9 out of 22 cases [253]. This is only one out of many PRT studies based on the interaction between bsAb and haptens that has been published or are in clinical trials. In general, when a pretargeting radiotherapeutic strategy is applied an increase of the overall survival rates has been observed [253,254]. However, as previously mentioned (see section 3.3.2), there are several challenges with this approach including immunogenic responses, which exclude very often repeated treatment.

Another approach, which has been applied for PRT is the biotin – streptavidin interaction. This system has been used in patients with glioblastoma. Patients were treated with ⁹⁰Y-labeled biotin as the therapeutic agent. An important finding from this study was that the tumor-to-bone marrow ratio was higher using the pretargeting technique compared to the conventional method (63:1 vs 6:1). Nevertheless, the approach also showed immunogenic responses in mice and humans [228].

A promising radionuclide for PRT is the alpha-emitter astatine-211. A number of biotin-derivatives have been ²¹¹As-labeled. To the best of our knowledge, these derivatives have only been evaluated using in vitro pretargeting [255], while, in vivo experiments are limited to pharmacokinetics studies [256–258]. Up to date, no clinical PRT studies using the hybridization of complimentary oligonucleotides have been reported in the literature. Proof-of-concept studies in mice bearing LS174T tumors showed tumor

Table 4
Selection of potential radionuclides for targeted radiotherapy [248].

Radionuclide	Decay	Half-life ^a	Maximum range in water (mm)	Gamma-photon energy ^b (MeV)	References
¹³¹ I	β^-	8.0 d	2.0 mm	0.364 (81%) and 0.606 (7%)	[249]
⁹⁰ Y	β^-	2.7 d	11.3 mm	1.7 (0.01%)	[250]
¹⁸⁸ Re	β^-	0.7 d	10.4 mm	0.155 (15%)	[251]
¹⁷⁷ Lu	β^-	6.7 d	1.8 mm	0.208 (11%)	[251]
⁶⁷ Cu	β^-	2.6 d	2.1 mm	0.185 (49%)	[251]
²¹³ Bi	α	0.8 h	55 – 85 μ m	0.440 (26%)	[251]
²¹¹ At	α	7.2 h		0.079 (21.3%)	[251]
²²⁵ Ac	α and β^- (decay chain)	10 d		0.099 (93%)	[251,252]
²¹² Pb	α and β^- (decay chain)	10.6 h	see Ref. [248]	see Ref. [248]	[252]

Notes:

^a Half-life is the time required for the activity to decrease to half of the original amount.

^b Energies of emitted gamma photons that can be used for imaging purposes.

recession when applying ^{90}Y - and ^{188}Re -derivatives. The ^{90}Y -derivative resulted in a higher tumor-to-non-tumor ratio, probably due to the longer half-life and thereby better dose accumulation in the tumor over time [166,167].

Finally, the SPAAC has also been evaluated in PRT with mAbs. At low azide:alkyne ratios, the reaction did not hold as a promising approach for targeted radionuclide therapy (see section 3.3.5) [194]. However, at higher azide:alkyne ratios the SPAAC could be applied to pretargeted therapy. In a recent study, the rituximab mAb targeting the CD20 antigen in lymphoma cells was functionalized with 10 DBCO groups and applied in PRT [196]. An ^{90}Y -labeled dendrimer functionalized with 29 azide groups was used as the therapeutic agent. In this case, *in vivo* pretargeting was achieved and a therapeutic effect was observed. Tumor regression was observed in all mice, with 67% of mice becoming tumor free, while the rest had tumor sizes below baseline. Here, the success of the pretargeting approach was attributed to the high degree of azide-functionalization of the dendrimer (i.e. number of azides present), which supposedly increases the rate of the SPAAC.

4.2.2. Tetrazine ligation-based studies

a) Lutetium-177

There have been several attempts to develop Tz-derivatives labeled with therapeutic radionuclides. For example, a number of ^{177}Lu -labeled Tz-frameworks have been developed and evaluated *in vivo* [259]. Noteworthy is the initial study by Rossin et al. where it was shown that a clearing step can increase the toxic tumor radiation dose compared to a directly labeled strategy [97]. In this study LS174T-tumor bearing mice were administered CC49-TCO (7 TCOs/mAb) followed by two doses of a galactose-albumin-based clearing agent (9–13 Tz/clearing agent) given 30 h and 48 h later. Two hours after the injection of clearing agent, [^{177}Lu]Lu-DOTA-PEG₁₁-Tz **21** (Table 5) was administered. To compare PRT with RIT, a second group of mice were treated with the directly labeled counterpart – [^{177}Lu]Lu-DOTA-CC49. *Ex vivo* biodistribution was used to calculate mouse and human dosimetry.

The use of a clearing agent lead to a 2-fold increase in tumor uptake and a 125-fold enhancement in the tumor-to-blood ratio compared to the approach without a clearing agent [97,100,194].

Moreover, the tumor uptake was persistent for at least 7 days, which is an indication of a sufficiently stable ligation adduct. This is an important fact since retention of radioactivity within the target region is necessary to guarantee the highest therapeutic effect and meanwhile the lowest level of radiotoxicity possible to healthy tissues. In contrast, a similar pretargeting approach using the streptavidin-biotin interaction and the same therapeutic radionuclide (^{177}Lu) resulted in a 10-fold decrease in tumor uptake after 7 days [260]. With regard to dosimetry [^{177}Lu]Lu-DOTA-PEG₁₁-Tz **21** (Table 5) showed high accumulation in the kidneys (1.58% ID/g at 3 h p.i.), however, in pretargeting experiments the bone marrow was estimated to be the dose limiting organ. Based on the limit for the maximum tolerated dose to the bone marrow, dosimetry calculations suggested that an 8-fold enhancement in tumor radiation dose should be possible in mice using the pretargeting system compared to using the conventional approach. In humans, a one to two order of magnitude reduction in radiation dose to non-targeted organs can be expected using PRT compared to RIT [100]. Encouraged by these results, several ^{177}Lu -labeled Tz-derivatives have been synthesized and evaluated by the same group in an attempt to reduce kidney uptake while retaining tumor uptake. Unfortunately, none of them showed improved properties. Either they resulted in poor tumor uptake or poor pharmacokinetics [259]. None of these ^{177}Lu -labeled Tz-derivatives have been reported to be evaluated for

therapeutic efficacy.

Another ^{177}Lu -labeled Tz, namely [^{177}Lu]Lu-DOTA-PEG₇-Tz **22** (Table 5), was developed and reported in 2017 [261]. Tz **22** (Table 5) was used in pancreatic BxPC3 tumor bearing mice pretreated with 5B1-TCO to explore if the radioligand could induce a dose-dependent therapeutic response. *Ex vivo* biodistribution showed a tumor uptake of 4.6% ID/g 4 h p.i. and 16.8% ID/g 120 h p.i. No clearing agent was used in this study. Although **22** was administered 72 h after the mAb, the enhanced tumor uptake was likely due to ligation in the blood followed by tumor uptake of the conjugate. Tumor regression or growth delay was observed at higher doses when compared to controls where saline or [^{177}Lu]Lu-DOTA-PEG₇-Tz **22** (Table 5) was administered without the TCO modified mAb (Fig. 26). Dosimetry estimations of the PRIT strategy using **22** (Table 5) supported that the bone marrow was the dose limiting organ. These estimations also indicated that the maximum tolerated dose (MTD) in humans (male, 70 kg) would be reached after a single administration of approx. 25.9 GBq (MTD 13.6/m² body size surface (BSA)). In comparison, conventional RIT studies with ^{177}Lu are reported to have a MTD between 1.7 and 2.6 GBq/m² BSA [262–264].

b) Copper-67

In 2017, Fujiki et al. reported ^{67}Cu -labeling of a DOTA-functionalized Tz **23** (Table 5) and its ligation to a TCO-functionalized anti-IGSF4 mAb. The biological affinity of the mAb remained intact following the ligation, based on ELISA analysis [265]. No pretargeting experiments were reported.

c) Lead-212

With the introduction of therapeutics such as the ^{223}Ra agent Xofigo [266] and the prostate cancer agent ^{212}Bi -PSMA-617 [267], there is an increasing interest in the utility of α -emitting radionuclides in targeted therapy. One of the advantages of α -emitters over β^- -emitting radionuclides is that they can deliver a much more toxic radiation dose while traveling a shorter distance. The ratio between the amount of energy emitted and the distance travelled in tissue is known as the linear energy transfer (LET). A higher LET value is advantageous because micrometastases can be targeted

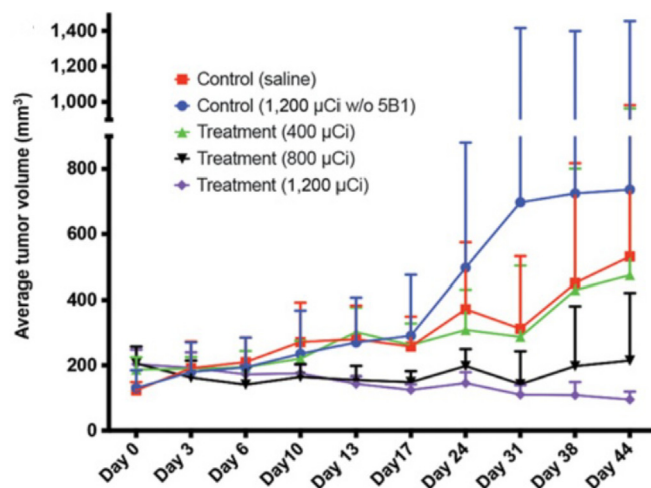


Fig. 26. Average tumor volume for each group of mice during the pretargeted radioimmunotherapy study. Tumor growth delayed with increasing amounts of [^{177}Lu]Lu-DOTA-PEG₇-Tz **22** when 5B1-TCO was administered compared to the controls. Figure modified from Ref. [261].

more efficiently while minimizing the radiation dose to surrounding healthy tissue [268].

The first reported Tz designed for α -therapy was labeled with lead-212 [269]. Lead-212 ($t_{1/2} = 10.6$ h) is an in vivo generator emitting alpha-particles within its decay chain. [^{212}Pb]Pb-DOTA-PEG₁₁-Tz **24** (Table 5) was evaluated in mice bearing LS174T tumors. TCO-functionalized CC49 and two doses of a clearing agent were applied before **24** (Table 5) was administered. The study was performed using the same protocol described above for [^{177}Lu]Lu-DOTA-PEG₁₁-Tz **21** (Table 5). In a control group, mice were given a TCO-functionalized mAb lacking affinity for the tumor antigen.

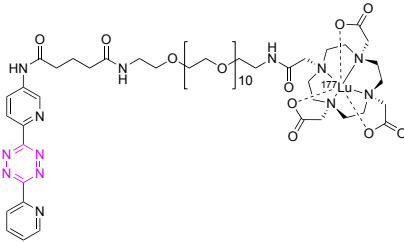
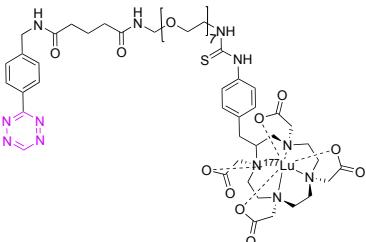
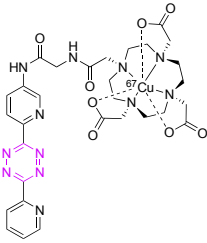
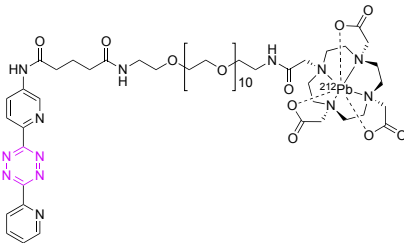
Ex vivo biodistribution revealed a tumor uptake of 0.94% ID/g at 3 h p.i., which declined to 0.66% ID/g 24 h p.i. This value is lower than what was observed for the ^{111}In - and ^{177}Lu -labeled variants of this Tz [97,100]. The reduced uptake can be attributed to the instability of the [^{212}Bi]Bi-DOTA complex, which is produced following [^{212}Pb]Pb-DOTA decay [252]. Nevertheless, therapeutic efficacy was observed, and the tumor growth rate was reduced with increasing dose of ^{212}Pb -labeled Tz **24** (Table 5) in the CC49-TCO pretreated mice compared to the mice given either directly labeled ^{212}Pb -TCMC-CC49 (RIT approach) or in mice pretreated with TCO-functionalized mAb lacking affinity for the tumor

antigen. Mice that were administered with only PBS or just CC49-TCO did not have any reduction in tumor growth rate. In addition, a high kidney uptake (2.5% ID/g 3 h p.i.) was observed, which prevents clinical translation of **24** (Table 5).

4.3. The use of pretargeting in theranostic approaches

The importance of a strategy for personalized medicine using passively targeting nanomedicines has been discussed in section 1.3 (see section 1.3, Fig. 2). Radiotherapeutic treatments with nanomedicines can result in strong radiotoxicity, therefore it is undoubtedly necessary to distinguish potential responders from likely non-responders before proceeding with EPR-based treatment forms [271]. The concept of theranostics in nuclear medicine combines diagnostic imaging and radiotherapy (Fig. 28A), typically by using “theranostic twins” – matched pairs of diagnostic and therapeutic radiopharmaceuticals, which differ negligibly from each other [272]. Ideally, the only difference is the radionuclide used [273]. The prostate cancer agent PSMA is a prominent example for which a theranostic approach has been applied. Here, PSMA radiolabeled with gallium-68, e.g. ^{68}Ga -PSMA-11, is used as a PET radiopharmaceutical for diagnosis, pre-therapeutic dosimetry and

Table 5
Various potential Tz-derivatives for pretargeted radiotherapy.

Tracer	Structure	Reference
21		[97,103,270]
22		[261]
23		[265]
24		[269]

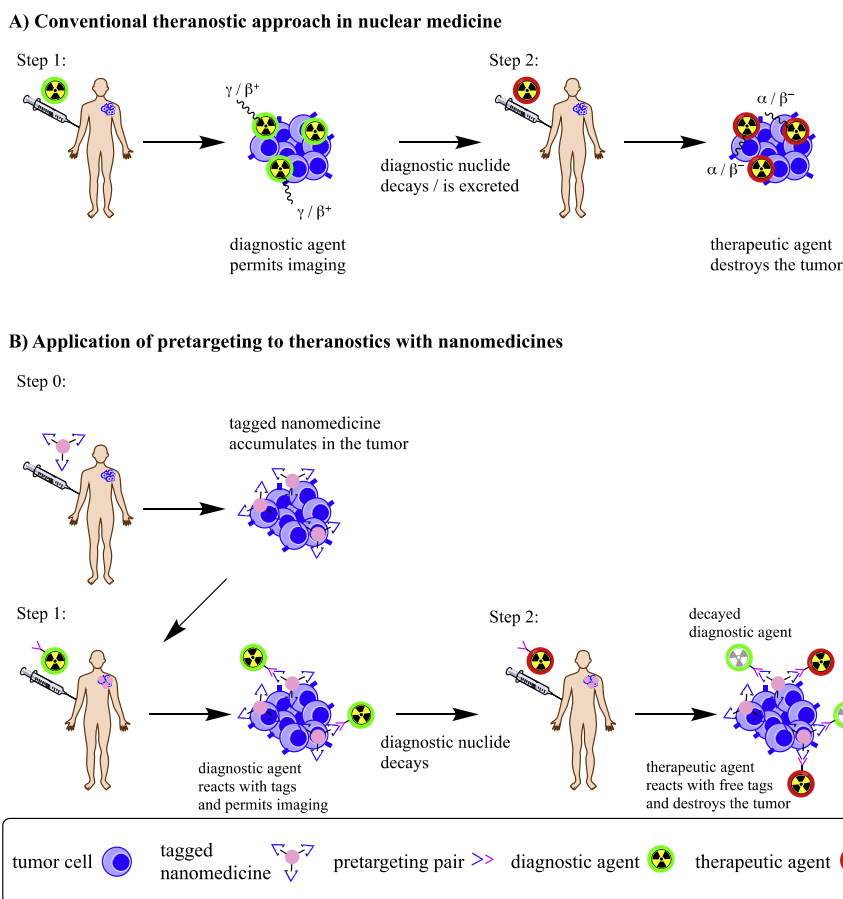


Fig. 28. Two types of theranostic approaches for nanomedicines in nuclear medicine. (A) Conventional approach. (B) Pretargeting approach.

dose finding, while a therapeutic analog, e.g. ^{177}Lu -PSMA-617, is applied for the actual treatment [274].

In summary, pretargeting strategies can contribute to the design and application of theranostic nanomedicines in two important ways. First, the modular design of pretargeting makes it possible to use the same tagged nanomedicine formulation for both diagnostic and therapeutic purposes (Fig. 28B). Second, the radiolabeled secondary agent in a pretargeting theranostic approach can be a fast-clearing small molecule, which can drastically reduce the radiation exposure of healthy tissues.

5. Comparison of pretargeting systems

The five pretargeting strategies discussed in this review have all shown success for use in *in vivo* imaging. However, more work is needed in order to achieve widespread use of pretargeting systems. Overall, the goal of pretargeting is to reach high target-to-non-target ratios at an earlier time point compared to the conventional approach with direct targeting. A number of criteria have to be fulfilled when choosing the ideal pretargeting strategy for a particular system. In addition to the factors that have to be considered for a direct targeting approach (e.g. properties of target and targeting vector), a pretargeting strategy also has to take into account the properties of the secondary agent. These criteria include (but are not limited to): (I) The secondary agent must bind to the primary agent with high affinity and fast reaction kinetics even at low concentrations. (II) The reactive pairs must show a high degree of stability and not be degraded too rapidly in prior to interacting or reacting with each other. (III) The pretargeting pairs

must interact or react specifically or selectively, such that there is no interference with endogenous biomolecules. (IV) Chemical and biochemical synthetic strategies should be in place so that (i) the primary targeting agent can be modified without disrupting its pharmacokinetic and pharmacodynamic properties, and (ii) the radioactive secondary agent can be efficiently produced in suitable quantities to perform the study. (V) The pretargeting pair should yield adequate target-to-non-target ratios *in vivo* at early time points, i.e. efficient clearance or deactivation of the primary targeting agent with or without clearing agents and fast clearance of the secondary agent after reaching maximum uptake at the target-site.

Throughout the previous sections, specific examples of pretargeted imaging have been discussed and the advantages and disadvantages of each have been outlined. The table below highlights some important evaluation criteria which serve as benchmarks to compare each pretargeting strategy (Table 6).

5.1. Binding of the pretargeting pair

Early pretargeting strategies were based on non-covalent high-affinity interactions. The recognition between bsAb and haptens has showed rate constants of $10^{3-5} \text{ M}^{-1} \text{ s}^{-1}$ [120]. However, the interaction is reversible, hence this strategy sometimes results in low tumor uptake [122]. The (strept)avidin-biotin interaction shows outstanding rate constants in the order of $10^7 \text{ M}^{-1} \text{ s}^{-1}$ (Table 6). In fact, the binding affinity between biotin and (strept)avidin is so strong ($K_d = 10^{-15} \text{ M}$) that it is often classified as irreversible binding [149]. Irreversible binding for a pretargeting pair is

Table 6
Comparison of pretargeting strategies [103,132,200,259,275–279].

Pretargeting system	Rate Constant ($M^{-1} s^{-1}$)	Temp. [$^{\circ}C$]	$t_{1/2}^a$ (1 μM)	In vivo stability of pretargeting pairs	Target-to-non-target ratios ^b	Clinical studies	Limitations
Bispecific antibodies and haptens recognition	10^{3-5}	38	6–41 min	High	Low without clearing agent	Yes	<ul style="list-style-type: none"> • Reversible binding between hapten and bsAb • Limited to Ab targeting vectors • Lower tumor uptake compared to other methods • Affinity between hapten and bsAb highly dependent on radiometal used
(Strept)Avidin- biotin interaction	10^7	37	ca. 0.3 s ^c	High	Moderate to high	Yes	<ul style="list-style-type: none"> • Susceptibility of radiolabeled biotin to biotinidase degradation • Immunogenic response to (strept)avidin • Competition with endogenous biotin
Hybridization of complementary oligonucleotides	10^4	37	ca. 1min	High	Moderate	No	<ul style="list-style-type: none"> • (PNA): Low tumor uptake when compared to other methods • Increased complexity to incorporate clearing agents • Challenging preparation
Strain-promoted azide-alkyne [3 + 2] cycloaddition	$10^{-1}-10^{-2}$	RT	1–9 months	Low	Low to moderate	No	<ul style="list-style-type: none"> • Only demonstrated in rodent models • Only a few successful in vivo applications reported • High molar ratio needed between pretargeting pairs
TCO-tetrazine ligation	10^{3-6}	37	0.4 s–2.8 min	Moderate	High	No	<ul style="list-style-type: none"> • Only demonstrated in rodent models so far • Tetrazine production is synthetically challenging

Notes:

^a Half-lives calculated from the k_2 , based on 1 μM concentrations for both tag and probe [103,120,275,276].

^b Reported levels are based on trends found in the literature of applied systems. All experiments were performed in various solvents at different concentrations and temperatures.

^c Own calculations. Abbreviations: RT = room temperature.

advantageous, to ensure high and persistent tumor uptake. Another pretargeting system that is based on non-covalent high-affinity interactions is the hybridization of complementary oligonucleotides. Rate constants in the order of $10^4 M^{-1} s^{-1}$ have been reported for this system. So far, no investigations have been addressed if the reversibility can influence the accumulation process [103,275]. The bioorthogonal reactions discussed in this review (SPAAC and the ligation between tetrazines and TCOs) are irreversible and the pretargeting pairs form strong covalent bonds between each other. Rate constants of $10^{-1} - 10^{-2} M^{-1} s^{-1}$ have been determined for the SPAAC. The tetrazine ligation has shown even higher values, in the order of $10^{3-7} M^{-1} s^{-1}$ [200,202].

In general terms, the interaction/reaction between pretargeting pairs usually occurs with pseudo-first order kinetics. Because of this, high rate constants are necessary. This becomes especially important when considering translation from small animals, such as rodents, to larger animals and eventually humans. Larger volumes decrease the probability of the interaction/reaction between the pretargeting pairs to occur. The success of the (strept)avidin-biotin interaction and the bsAbs-hapten recognition for in vivo pretargeting in humans indicate that rate constants of $10^{3-7} M^{-1} s^{-1}$ are suitable for clinical application. Given this, the rate constants of the SPAAC could be problematic for clinical translation. Only two successful preclinical studies have been reported using this system [105,196] and in both cases increased amounts of the strained alkyne or the azide were used for pretargeting to occur.

5.2. Immunogenicity

The bsAb-hapten recognition and the (strept)avidin-biotin interaction can induce an immunogenic response in humans [108,247]. No reports of an immunogenic response induced by

hybridization of complementary oligonucleotides or using bioorthogonal strategies have been reported.

5.3. In vivo stability of the secondary pretargeting agent

Stability of radiolabeled haptens has been demonstrated for in vivo pretargeting systems based on the bsAb-hapten recognition [280]. In contrast, the stability of biotin remains to be suspectable since biotin may be degraded via biotinases [141]. Oligonucleotides are usually very prone for metabolism. However, oligonucleotides that can be applied for pretargeting systems have been designed for enhanced stability and show in fact sufficient stability in vivo [151]. Tags for bioorthogonal chemistry used so far have only limited in vivo stability [200,259,281].

5.4. Concluding remarks

Considering all aforementioned evaluation criteria, we believe that the combination of fast reaction kinetics, high specificity, the small molecule character, synthetic accessibility, reaction irreversibility and bioorthogonality of the tetrazine ligation make it the most attractive system for many pretargeting approaches. Also, in contrast to other established pretargeting systems, such as the (strept)avidin-biotin interaction or the bsAb-hapten recognition, no concerns about immunogenicity have been reported so far. The reachable rate constants appear to be in the order of what is clinical relevant. In principle, the pharmacokinetic profile of the applied Tz can also be tailored using standard medicinal chemistry strategies. This could potentially be used for the development of cell membrane permeable Tz-derivatives. So far, pretargeted imaging and radiotherapy (including the tetrazine ligation) is limited to targets on the cell surface. Cell membrane-permeating fluorescent Tz-frameworks have already been developed and used to image

intracellular targets, but radiopharmaceutical counterparts are missing [282–288].

Finally, nano-sized targeting vectors such as polymers, liposomes or nanoparticles can be decorated with a high number of TCOs. A higher TCO-loading facilitates the likelihood of the tetrazine ligation to occur. In this respect, the tetrazine ligation appears to be especially suited to image nanomedicines or to conduct PRIT.

6. Summary and outlook

Strategies for pretargeted imaging and radiotherapy have been described since the late 1980s. Since then they have attracted considerable attention in nuclear medicine, drug discovery and drug development. Several pretargeting strategies have been developed over the years. The bsAbs and hapten recognition and the (strept)avidin-biotin interaction have already been applied in the clinic. Unfortunately, the bsAb-hapten recognition resulted in a relatively low imaging contrast and caused an immunogenic response. Likewise, the (strept)avidin-biotin interaction also resulted in an immunogenic response and because of that, other pretargeting strategies for in vivo chemistry have been developed. Lately, the tetrazine ligation has become the most highlighted approach for pretargeting strategies. In total 66 publications (PubMed search) have been published within the field of radiopharmaceutical chemistry since Rossin and colleagues [100] utilized the tetrazine ligation for nuclear imaging in 2010. This number is expected to continuously increase in the following years, especially if a clinical proof-of-principle study will emerge as a result of the great efforts worldwide to translate pretargeted imaging based on the tetrazine ligation from preclinical to clinical studies. The motivations for clinical translation are many. Firstly, high target accumulation and excellent image contrasts have been observed. Also, the pharmacokinetics of the secondary imaging agent, the radiolabeled tetrazine, can easily be altered, which makes the tetrazine ligation more versatile compared to other pretargeting strategies with similar reaction kinetics. In addition, the tetrazine ligation also allows the imaging of currently inaccessible targets, e.g. intracellular targets, since smaller and more lipophilic Tz-derivatives can be synthesized to cross cell membranes. Ultimately, the tetrazine ligation possesses several favorable characteristics for a pretargeting strategy to be applied not only for nuclear imaging and radiotherapy, but also for theranostic approaches. For the latter, diagnostic and therapeutic radionuclide pairs can straightforwardly be incorporated to Tz-derivatives and the same primary targeting vector can be used for both the diagnostic Tz and the therapeutic one (Fig. 28).

From a broader perspective, pretargeted imaging, in particular approaches based on the tetrazine ligation, is perfectly suited to translate nanomedicinal drug delivery from bench to bedside since it can circumvent the radionuclide dilemma (section 2.3, Figs. 3 and 4) and thereby facilitate personalized medicine (section 1.3, Fig. 2). Currently, the research community has focused mainly on mAbs as primary targeting agents in pretargeted imaging approaches. However, nanomedicines hold the advantage to be decorated with higher amounts of reactive tags (i.e. TCOs for the tetrazine ligation). As a result, the in vivo reaction between the secondary imaging agent and the targeting agent is more likely to occur. In our opinion pretargeting approaches will not only be highlighted as a method for identifying which patients are in fact responders to nanomedicinal treatment in the close future, but also improve current endoradiotherapy approaches and facilitate broader clinical use. Still, extensive work has to be done to find an ideal pretargeting set-up working in the clinic. Even though the tetrazine ligation shows great promise, it is not fully clarified if the ligation shows suitable in vivo characteristics to be translated from mice to humans.

Another challenge is to develop a suitable Tz for PET imaging, preferably radiolabeled with fluorine-18 and with the potential to image intracellular targets. Finally, there are not many reported Tz-derivatives radiolabeled with therapeutic radionuclides. It still has to be shown if one of them can be used in the clinic.

Acknowledgements

This project has received funding from the European Union's Horizon 2020 research and innovation programme under grant agreement No 668532: Click-it.

References

- [1] J. Shi, et al., Cancer nanomedicine: progress, challenges and opportunities, *Nat. Rev. Canc.* 17 (1) (2017) 20–37.
- [2] R. Duncan, M.J. Vicent, Polymer therapeutics-prospects for 21st century: the end of the beginning, *Adv. Drug Deliv. Rev.* 65 (1) (2013) 60–70.
- [3] C. Ayala-Orozco, et al., Sub-100nm gold nanomatryoshkas improve photothermal therapy efficacy in large and highly aggressive triple negative breast tumors, *J. Contr. Release* 191 (2014) 90–97.
- [4] K. Norregaard, et al., 18F-FDG PET/CT-based early treatment response evaluation of nanoparticle-assisted photothermal cancer therapy, *PLoS One* 12 (5) (2017) e0177997.
- [5] T. Lammers, et al., Drug targeting to tumors: principles, pitfalls and (pre-) clinical progress, *J. Contr. Release* 161 (2) (2012) 175–187.
- [6] N. Kamaly, et al., Degradable controlled-release Polymers and polymeric nanoparticles: Mechanisms of controlling drug release, *Chem. Rev.* 116 (4) (2016) 2602–2663.
- [7] A. Wicki, et al., Nanomedicine in cancer therapy: challenges, opportunities, and clinical applications, *J. Contr. Release* 200 (2015) 138–157.
- [8] R.K. Jain, T. Stylianopoulos, Delivering nanomedicine to solid tumors, *Nat. Rev. Clin. Oncol.* 7 (11) (2010) 653–664.
- [9] H. Lee, et al., (64)Cu-MM-302 positron emission tomography quantifies Variability of enhanced Permeability and Retention of Nanoparticles in Relation to treatment Response in Patients with metastatic breast cancer, *Clin. Canc. Res.* 23 (15) (2017) 4190–4202.
- [10] R.K. Ramanathan, et al., Correlation between ferumoxytol uptake in tumor lesions by MRI and response to nanoliposomal irinotecan in patients with advanced solid tumors: a pilot study, *Clin. Canc. Res.* 23 (14) (2017) 3638–3648.
- [11] C.M. Dawidczyk, et al., State-of-the-art in design rules for drug delivery platforms: lessons learned from FDA-approved nanomedicines, *J. Contr. Release* 187 (2014) 133–144.
- [12] Y. Matsumura, H. Maeda, A new concept for macromolecular therapeutics in cancer chemotherapy: mechanism of tumoritropic accumulation of proteins and the antitumor agent smancs, *Canc. Res.* 46 (12 Pt 1) (1986) 6387–6392.
- [13] D. Ribatti, et al., The structure of the vascular network of tumors, *Canc. Lett.* 248 (1) (2007) 18–23.
- [14] J. Fang, H. Nakamura, H. Maeda, The EPR effect: Unique features of tumor blood vessels for drug delivery, factors involved, and limitations and augmentation of the effect, *Adv. Drug Deliv. Rev.* 63 (3) (2011) 136–151.
- [15] M.W. Dewhirst, T.W. Secomb, Transport of drugs from blood vessels to tumour tissue, *Nat. Rev. Canc.* 17 (12) (2017) 738–750.
- [16] E. Blanco, H. Shen, M. Ferrari, Principles of nanoparticle design for overcoming biological barriers to drug delivery, *Nat. Biotechnol.* 33 (9) (2015) 941–951.
- [17] T. Stylianopoulos, R.K. Jain, Design considerations for nanotherapeutics in oncology, *Nanomedicine* 11 (8) (2015) 1893–1907.
- [18] H. Kobayashi, R. Watanabe, P.L. Choyke, Improving conventional enhanced permeability and retention (EPR) effects; what is the appropriate target? *Theranostics* 4 (1) (2013) 81–89.
- [19] U. Prabhakar, et al., Challenges and key considerations of the enhanced permeability and retention effect for nanomedicine drug delivery in oncology, *Canc. Res.* 73 (8) (2013) 2412–2417.
- [20] Y.H. Bae, K. Park, Targeted drug delivery to tumors: myths, reality and possibility, *J. Contr. Release* 153 (3) (2011) 198–205.
- [21] M. Allmeroth, et al., HPMA-LMA copolymer drug carriers in oncology: an in vivo PET study to assess the tumor line-specific polymer uptake and body distribution, *Biomacromolecules* 14 (9) (2013) 3091–3101.
- [22] A.E. Hansen, et al., Positron emission tomography based elucidation of the enhanced permeability and retention effect in dogs with cancer using Copper-64 liposomes, *ACS Nano* 9 (7) (2015) 6985–6995.
- [23] A.A. Natfji, et al., Parameters affecting the enhanced permeability and retention effect: the need for patient selection, *J. Pharmacol. Sci.* 106 (11) (2017) 3179–3187.
- [24] K.J. Harrington, et al., Effective targeting of solid tumors in patients with locally advanced cancers by radiolabeled pegylated liposomes, *Clin. Canc. Res.* 7 (2) (2001) 243–254.
- [25] B. Theek, et al., The theranostic path to personalized nanomedicine, *Clin*

- Transl Imaging 2 (1) (2014) 66–76.
- [26] J.L. Kristensen, M.M. Herth, Textbook of Drug Design and Discovery: In Vivo Imaging in Drug Discovery, fifth ed., 2017.
- [27] T.F. Massoud, S.S. Gambhir, Molecular imaging in living subjects: seeing fundamental biological processes in a new light, *Genes Dev.* 17 (5) (2003) 545–580.
- [28] O. Arrieta, et al., High liposomal doxorubicin tumour tissue distribution, as determined by radiopharmaceutical labelling with (99m)Tc-LD, is associated with the response and survival of patients with unresectable pleural mesothelioma treated with a combination of liposomal doxorubicin and cisplatin, *Canc. Chemother. Pharmacol.* 74 (1) (2014) 211–215.
- [29] J.L.J. Dearing, A.B. Packard, Molecular imaging in nanomedicine - a developmental tool and a clinical necessity, *J. Contr. Release* 261 (2017) 23–30.
- [30] C. Perez-Medina, et al., Nanoreporter PET predicts the efficacy of anti-cancer nanotherapy, *Nat. Commun.* 7 (2016) 11838.
- [31] S. Wilhelm, et al., Analysis of nanoparticle delivery to tumours, *Nat. Rev.* 1 (2016) 1–12.
- [32] D. Sun, Nanotheranostics: integration of imaging and targeted drug delivery, *Mol. Pharm.* 7 (6) (2010) 1879.
- [33] L.W. Seymour, et al., Hepatic drug targeting: phase I evaluation of polymer-bound doxorubicin, *J. Clin. Oncol.* 20 (6) (2002) 1668–1676.
- [34] H. Maeda, et al., Tumor vascular permeability and the EPR effect in macromolecular therapeutics: a review, *J. Contr. Release* 65 (1–2) (2000) 271–284.
- [35] S.M. Cheal, et al., Pairwise comparison of 89Zr- and 124I-labeled cG250 based on positron emission tomography imaging and nonlinear immunokinetic modeling: in vivo carbonic anhydrase IX receptor binding and internalization in mouse xenografts of clear-cell renal cell carcinoma, *Eur. J. Nucl. Med. Mol. Imag.* 41 (5) (2014) 985–994.
- [36] X. Yang, et al., cRGD-functionalized, DOX-conjugated, and (6)(4)Cu-labeled superparamagnetic iron oxide nanoparticles for targeted anticancer drug delivery and PET/MR imaging, *Biomaterials* 32 (17) (2011) 4151–4160.
- [37] G.L. Wolf, Handbook of Targeted Delivery of Imaging Agents, vol. 3, CRC Press, 1995.
- [38] A. Rahmim, H. Zaidi, PET versus SPECT: strengths, limitations and challenges, *Nucl. Med. Commun.* 29 (3) (2008) 193–207.
- [39] R.J. Hicks, M.S. Hofman, Is there still a role for SPECT-CT in oncology in the PET-CT era? *Nat. Rev. Clin. Oncol.* 9 (12) (2012) 712–720.
- [40] M. Conti, L. Eriksson, Physics of pure and non-pure positron emitters for PET: a review and a discussion, *EJNMMI Phys* 3 (1) (2016) 8.
- [41] J. Barbet, et al., Radiolabeled antibodies for cancer imaging and therapy, *Meth. Mol. Biol.* 907 (2012) 681–697.
- [42] T.L. Ross, Handb. Nucl. Chem.: 18F: Labeling Chemistry and Labeled Compounds, Springer, 2011.
- [43] S. Li, et al., Iodine-123-vascular endothelial growth factor-165 (123I-VEGF165). Biodistribution, safety and radiation dosimetry in patients with pancreatic carcinoma, *Q. J. Nucl. Med. Mol. Imaging* 48 (3) (2004) 198–206.
- [44] G.J. Forster, et al., Preliminary data on biodistribution and dosimetry for therapy planning of somatostatin receptor positive tumours: comparison of (86)Y-DOTATOC and (111)In-DTPA-octreotide, *Eur. J. Nucl. Med.* 28 (12) (2001) 1743–1750.
- [45] A. Pfeifer, et al., Clinical PET of neuroendocrine tumors using 64Cu-DOTA-TATE: first-in-humans study, *J. Nucl. Med.* 53 (8) (2012) 1207–1215.
- [46] P.K. Borjesson, et al., Radiation dosimetry of 89Zr-labeled chimeric monoclonal antibody U36 as used for immuno-PET in head and neck cancer patients, *J. Nucl. Med.* 50 (11) (2009) 1828–1836.
- [47] C.M. Zechmann, et al., Radiation dosimetry and first therapy results with a (124)I/(131)I-labeled small molecule (MIP-1095) targeting PSMA for prostate cancer therapy, *Eur. J. Nucl. Med. Mol. Imag.* 41 (7) (2014) 1280–1292.
- [48] G.J. Kemerink, et al., Patient dosimetry of intravenously administered 99mTc-annexin V, *J. Nucl. Med.* 42 (2) (2001) 382–387.
- [49] T. Tolvanen, et al., Biodistribution and radiation dosimetry of [(11)C]choline: a comparison between rat and human data, *Eur. J. Nucl. Med. Mol. Imag.* 37 (5) (2010) 874–883.
- [50] C. Pettinato, et al., 68Ga-DOTANOC: biodistribution and dosimetry in patients affected by neuroendocrine tumors, *Eur. J. Nucl. Med. Mol. Imag.* 35 (1) (2008) 72–79.
- [51] P106: radiation Dose to Patients from radiopharmaceuticals. A third amendment to ICRP publication 53, *Ann. ICRP* 38 (2008) 51–162.
- [52] K. Stockhofe, et al., Radiolabeling of nanoparticles and polymers for PET imaging, *Pharmaceuticals* 7 (4) (2014) 392–418.
- [53] K. Pant, et al., Radiolabelled polymeric materials for imaging and treatment of cancer: quo vadis? *Adv Healthc Mater* 6 (6) (2017).
- [54] J. Lamb, J.P. Holland, Advanced methods for radiolabeling multimodality nanomedicines for SPECT/MRI and PET/MRI, *J. Nucl. Med.* 59 (3) (2018) 382–389.
- [55] D.S. Abou, J.E. Pickett, D.L. Thorek, Nuclear molecular imaging with nanoparticles: radiochemistry, applications and translation, *Br. J. Radiol.* 88 (1054) (2015) 20150185.
- [56] Y. Liu, M.J. Welch, Nanoparticles labeled with positron emitting nuclides: advantages, methods, and applications, *Bioconjug Chem* 23 (4) (2012) 671–682.
- [57] E.W. Price, C. Orvig, Matching chelators to radiometals for radiopharmaceuticals, *Chem. Soc. Rev.* 43 (1) (2014) 260–290.
- [58] Z. Li, P.S. Conti, Radiopharmaceutical chemistry for positron emission tomography, *Adv. Drug Deliv. Rev.* 62 (11) (2010) 1031–1051.
- [59] G. Unak, et al., Gold nanoparticle probes: design and in vitro applications in cancer cell culture, *Colloids Surfaces B Biointerfaces* 90 (2012) 217–226.
- [60] R. Kumar, et al., In vivo biodistribution and clearance studies using multimodal organically modified silica nanoparticles, *ACS Nano* 4 (2) (2010) 699–708.
- [61] D.E. Lee, et al., Facile method to radiolabel glycol chitosan nanoparticles with (64)Cu via copper-free click chemistry for MicroPET imaging, *Mol. Pharm.* 10 (6) (2013) 2190–2198.
- [62] V. Biju, Chemical modifications and bioconjugate reactions of nanomaterials for sensing, imaging, drug delivery and therapy, *Chem. Soc. Rev.* 43 (3) (2014) 744–764.
- [63] D. Zeng, et al., The growing impact of bioorthogonal click chemistry on the development of radiopharmaceuticals, *J. Nucl. Med.* 54 (6) (2013) 829–832.
- [64] M.M. Herth, et al., 72/74As-labeling of HPMA based polymers for long-term in vivo PET imaging, *Bioorg. Med. Chem. Lett* 20 (18) (2010) 5454–5458.
- [65] A. Almutairi, et al., Biodegradable dendritic positron-emitting nanoprobes for the noninvasive imaging of angiogenesis, *Proc. Natl. Acad. Sci. U. S. A.* 106 (3) (2009) 685–690.
- [66] E.A. Simone, et al., Endothelial targeting of polymeric nanoparticles stably labeled with the PET imaging radioisotope iodine-124, *Biomaterials* 33 (21) (2012) 5406–5413.
- [67] M. Sarparanta, et al., (18)F-labeled modified porous silicon particles for investigation of drug delivery Carrier distribution in vivo with positron emission tomography, *Mol. Pharm.* 8 (5) (2011) 1799–1806.
- [68] S. Berke, et al., (18)F-Radiolabeling and in vivo Analysis of SiFA-derivatized polymeric core-shell nanoparticles, *Bioconjug Chem* 29 (1) (2018) 89–95.
- [69] X. Sun, et al., An assessment of the effects of shell cross-linked nanoparticle size, core composition, and surface PEGylation on in vivo biodistribution, *Biomacromolecules* 6 (5) (2005) 2541–2554.
- [70] M.R. McDevitt, et al., PET imaging of soluble yttrium-86-labeled carbon nanotubes in mice, *PLoS One* 2 (9) (2007) e907.
- [71] B. Hoang, et al., Noninvasive monitoring of the fate of 111In-labeled block copolymer micelles by high resolution and high sensitivity microSPECT/CT imaging, *Mol. Pharm.* 6 (2) (2009) 581–592.
- [72] Q. Liu, et al., 18F-Labeled magnetic-upconversion nanophosphors via rare-Earth cation-assisted ligand assembly, *ACS Nano* 5 (4) (2011) 3146–3157.
- [73] J. Zhou, et al., Fluorine-18-labeled Gd3+/Yb3+/Er3+ co-doped NaYF4 nanophosphors for multimodality PET/MR/UCL imaging, *Biomaterials* 32 (4) (2011) 1148–1156.
- [74] E. Boros, et al., Chelate-free metal ion binding and heat-induced radiolabeling of iron oxide nanoparticles, *Chem. Sci.* 6 (1) (2015) 225–236.
- [75] T.M. Shaffer, et al., Silica nanoparticles as substrates for chelator-free labeling of oxophilic radioisotopes, *Nano Lett.* 15 (2) (2015) 864–868.
- [76] D.S. Abou, et al., (89)Zr-labeled paramagnetic octreotide-liposomes for PET-MR imaging of cancer, *Pharm. Res. (N. Y.)* 30 (3) (2013) 878–888.
- [77] L. Stelter, et al., Modification of aminosilane superparamagnetic nanoparticles: feasibility of multimodal detection using 3T MRI, small animal PET, and fluorescence imaging, *Mol. Imag. Biol.* 12 (1) (2010) 25–34.
- [78] R. Sharma, et al., Carbon-11 radiolabeling of iron-oxide nanoparticles for dual-modality PET/MR imaging, *Nanoscale* 5 (16) (2013) 7476–7483.
- [79] S. Guerrero, et al., Synthesis and in vivo evaluation of the biodistribution of a 18F-labeled conjugate gold-nanoparticle-peptide with potential biomedical application, *Bioconjug Chem* 23 (3) (2012) 399–408.
- [80] S. Rojas, et al., Biodistribution of amino-functionalized diamond nanoparticles. In vivo studies based on 18F radionuclide emission, *ACS Nano* 5 (7) (2011) 5552–5559.
- [81] J. Zhu, et al., Rapid (18)F-labeling and loading of PEGylated gold nanoparticles for in vivo applications, *Bioconjug Chem* 25 (6) (2014) 1143–1150.
- [82] M.M. Herth, et al., Radioactive labeling of defined HPMA-based polymeric structures using [18F]FETos for in vivo imaging by positron emission tomography, *Biomacromolecules* 10 (7) (2009) 1697–1703.
- [83] X. Cui, et al., Aluminium hydroxide stabilised MnFe2O4 and Fe3O4 nanoparticles as dual-modality contrast agent for MRI and PET imaging, *Biomaterials* 35 (22) (2014) 5840–5846.
- [84] X. Cui, et al., Synthesis, characterization, and Application of core-shell Co0.16Fe2.84O4@NaYF4(Yb, Er) and Fe3O4@NaYF4(Yb, Tm) Nanoparticle as trimodal (MRI, PET/SPECT, and optical) imaging agents, *Bioconjug Chem* 27 (2) (2016) 319–328.
- [85] A.L. Petersen, et al., 64Cu loaded liposomes as positron emission tomography imaging agents, *Biomaterials* 32 (9) (2011) 2334–2341.
- [86] B.T. Cisneros, et al., Stable confinement of positron emission tomography and magnetic resonance agents within carbon nanotubes for bimodal imaging, *Nanomedicine* 9 (16) (2014) 2499–2509.
- [87] W.T. Phillips, et al., A simple method for producing a technetium-99m-labeled liposome which is stable in vivo, *Int J Rad Appl Instrum B* 19 (5) (1992) 539–547.
- [88] R.M. Wong, et al., Rapid size-controlled synthesis of dextran-coated, 64Cu-doped iron oxide nanoparticles, *ACS Nano* 6 (4) (2012) 3461–3467.
- [89] J. Pellico, et al., Fast synthesis and bioconjugation of (68) Ga core-doped extremely small iron oxide nanoparticles for PET/MR imaging, *Contrast Media Mol. Imaging* 11 (3) (2016) 203–210.
- [90] A.F. Frelsen, et al., Mouse positron emission tomography study of the bio-distribution of gold nanoparticles with different surface coatings using embedded Copper-64, *ACS Nano* 10 (11) (2016) 9887–9898.
- [91] C. Perez-Campana, et al., Tracing nanoparticles in vivo: a new general

- synthesis of positron emitting metal oxide nanoparticles by proton beam activation, *Analyst* 137 (21) (2012) 4902–4906.
- [92] C. Perez-Campana, et al., Biodistribution of different sized nanoparticles assessed by positron emission tomography: a general strategy for direct activation of metal oxide particles, *ACS Nano* 7 (4) (2013) 3498–3505.
- [93] K.C. Black, et al., Dual-radiolabeled nanoparticle SPECT probes for bio-imaging, *Nanoscale* 7 (2) (2015) 440–444.
- [94] W.G. Kreyling, et al., In vivo integrity of polymer-coated gold nanoparticles, *Nat. Nanotechnol.* 10 (7) (2015) 619–623.
- [95] J. Llop, et al., In vivo stability of protein coatings on poly lactic co glycolic nanoparticles, *MRS Advances* 1 (2016) 3767–3773.
- [96] P103: the 2007 Recommendations of the international Commission on radiological protection, *Ann. ICRP* 37 (2–4) (2007) 81–123.
- [97] R. Rossin, et al., Diels-Alder reaction for tumor pretargeting: in vivo chemistry can boost tumor radiation dose compared with directly labeled antibody, *J. Nucl. Med.* 54 (11) (2013) 1989–1995.
- [98] D.T. Reardan, et al., Antibodies against metal chelates, *Nature* 316 (6025) (1985) 265–268.
- [99] D.A. Goodwin, et al., Monoclonal antibody hapten radiopharmaceutical delivery, *Nucl. Med. Commun.* 7 (8) (1986) 569–580.
- [100] R. Rossin, et al., In vivo chemistry for pretargeted tumor imaging in live mice, *Angew Chem. Int. Ed. Engl.* 49 (19) (2010) 3375–3378.
- [101] L. Karmani, et al., Biodistribution of (125)I-labeled anti-endoglin antibody using SPECT/CT imaging: Impact of in vivo deiodination on tumor accumulation in mice, *Nucl. Med. Biol.* 43 (7) (2016) 415–423.
- [102] M. Patra, et al., New insights into the pretargeting approach to image and treat tumours, *Chem. Soc. Rev.* 45 (23) (2016) 6415–6431.
- [103] R. Rossin, M.S. Robillard, Pretargeted imaging using bioorthogonal chemistry in mice, *Curr. Opin. Chem. Biol.* 21 (2014) 161–169.
- [104] S. Hou, et al., Pretargeted positron emission tomography imaging that employs supramolecular nanoparticles with in vivo bioorthogonal chemistry, *ACS Nano* 10 (1) (2016) 1417–1424.
- [105] S.B. Lee, et al., Mesoporous silica nanoparticle pretargeting for PET imaging based on a rapid bioorthogonal reaction in a living body, *Angew Chem. Int. Ed. Engl.* 52 (40) (2013) 10549–10552.
- [106] O. Keinanen, et al., Pretargeted PET Imaging of trans-cyclooctene-modified porous silicon nanoparticles, *ACS Omega* 2 (1) (2017) 62–69.
- [107] C. Denk, et al., Development of a (18) F-labeled tetrazine with favorable pharmacokinetics for bioorthogonal PET imaging, *Angew Chem. Int. Ed. Engl.* 53 (36) (2014) 9655–9659.
- [108] H. Sakahara, T. Saga, Avidin-biotin system for delivery of diagnostic agents, *Adv. Drug Deliv. Rev.* 37 (1–3) (1999) 89–101.
- [109] M.K. Rahim, R. Kota, J.B. Haun, Enhancing reactivity for bioorthogonal pretargeting by unmasking antibody-conjugated trans-cyclooctenes, *Bioconjug Chem* 26 (2) (2015) 352–360.
- [110] H.L. Evans, et al., A bioorthogonal (68)Ga-labelling strategy for rapid in vivo imaging, *Chem Commun (Camb)* 50 (67) (2014) 9557–9560.
- [111] D. Schumacher, et al., Current status: site-specific antibody drug conjugates, *J. Clin. Immunol.* 36 (Suppl 1) (2016) 100–107.
- [112] P. Agarwal, C.R. Bertozzi, Site-specific antibody–drug conjugates: the nexus of bioorthogonal chemistry, protein engineering, and drug development, *Bioconjug Chem* 26 (2) (2015) 176–192.
- [113] J. Guo, et al., Characterization and higher-order structure Assessment of an interchain cysteine-based ADC: Impact of drug Loading and Distribution on the Mechanism of aggregation, *Bioconjug Chem* 27 (3) (2016) 604–615.
- [114] R.P. Lyon, et al., Reducing hydrophobicity of homogeneous antibody–drug conjugates improves pharmacokinetics and therapeutic index, *Nat. Biotechnol.* 33 (7) (2015) 733–735.
- [115] J.B. Haun, et al., Bioorthogonal chemistry amplifies nanoparticle binding and enhances the sensitivity of cell detection, *Nat. Nanotechnol.* 5 (9) (2010) 660–665.
- [116] D.H. Dube, C.R. Bertozzi, Metabolic oligosaccharide engineering as a tool for glycobiology, *Curr. Opin. Chem. Biol.* 7 (5) (2003) 616–625.
- [117] R.E. Kontermann, U. Brinkmann, Bispecific antibodies, *Drug Discov. Today* 20 (7) (2015) 838–847.
- [118] D.R. Stickney, et al., Bifunctional antibody: a binary radiopharmaceutical delivery system for imaging colorectal carcinoma, *Canc. Res.* 51 (24) (1991) 6650–6655.
- [119] D.A. Goodwin, et al., Pre-targeted immunoscintigraphy of murine tumors with indium-111-labeled bifunctional haptens, *J. Nucl. Med.* 29 (2) (1988) 226–234.
- [120] P.J. Yazaki, et al., A series of anti-CEA/anti-DOTA bispecific antibody formats evaluated for pre-targeting: comparison of tumor uptake and blood clearance, *Protein Eng. Des. Sel.* 26 (3) (2013) 187–193.
- [121] D.A. Goodwin, C.F. Meares, M. McTigue, Rapid localization of hapten in sites containing previously administered antibody for immunoscintigraphy with short half-life tracers, *J. Nucl. Med.* 27 (1986) 9959.
- [122] E. Gautherot, et al., Delivery of therapeutic doses of radioiodine using bispecific antibody-targeted bivalent haptens, *J. Nucl. Med.* 39 (11) (1998) 1937–1943.
- [123] R. Schoffelen, et al., Pretargeted immuno-positron emission tomography imaging of carcinoembryonic antigen-expressing tumors with a bispecific antibody and a 68Ga- and 18F-labeled hapten peptide in mice with human tumor xenografts, *Mol. Canc. Therapeut.* 9 (4) (2010) 1019–1027.
- [124] C. Bodet-Milin, et al., Immuno-pet using Anticarcinoembryonic antigen bispecific Antibody and 68Ga-labeled Peptide in metastatic medullary thyroid carcinoma: clinical Optimization of the pretargeting Parameters in a first-in-human trial, *J. Nucl. Med.* 57 (10) (2016) 1505–1511.
- [125] A. Rauscher, et al., Improvement of the targeting of radiolabeled and functionalized liposomes with a two-step system using a bispecific monoclonal antibody (Anti-CEA x anti-dtpa-in), *Front. Med.* 2 (2015) 83.
- [126] Bispecific Antibody in Finding Tumor Cells in Patients With Colorectal Cancer. Available from: <https://ClinicalTrials.gov/show/NCT00895323>.
- [127] Study of Pretargeted Radioimmunotherapy of an Anti-CEA Bispecific Antibody and Lu177-labeled Peptide in Colorectal Cancer. Available from: <https://ClinicalTrials.gov/show/NCT00860860>.
- [128] Imaging Colo-rectal Cancer Using a Two Step Antibody Technique in Nuclear Imaging. Available from: <https://ClinicalTrials.gov/show/NCT00185081>.
- [129] J.J. Panek, et al., Effects of tryptophan residue fluorination on streptavidin stability and biotin-streptavidin interactions via molecular dynamics simulations, *J. Mol. Model.* 15 (3) (2009) 257–266.
- [130] A. Taninaka, O. Takeuchi, H. Shigekawa, Hidden variety of biotin-streptavidin/avidin local interactions revealed by site-selective dynamic force spectroscopy, *Phys. Chem. Chem. Phys.* 12 (39) (2010) 12578–12583.
- [131] J. DeChancie, K.N. Houk, The origins of femtomolar protein–ligand binding: hydrogen-bond cooperativity and desolvation energetics in the biotin-(strept)avidin binding site, *J. Am. Chem. Soc.* 129 (17) (2007) 5419–5429.
- [132] D.J. Green, et al., Comparative analysis of bispecific antibody and streptavidin-targeted radioimmunotherapy for B-cell cancers, *Canc. Res.* 76 (22) (2016) 6669–6679.
- [133] E.P. Diamandis, T.K. Christopoulos, The biotin-(strept)avidin system: principles and applications in biotechnology, *Clin. Chem.* 37 (5) (1991) 625–636.
- [134] V.V. Sinityn, et al., Rapid blood clearance of biotinylated IgG after infusion of avidin, *J. Nucl. Med.* 30 (1) (1989) 66–69.
- [135] D.J. Hnatowich, F. Virzi, M. Ruscowski, Investigations of avidin and biotin for imaging applications, *J. Nucl. Med.* 28 (8) (1987) 1294–1302.
- [136] M.V. Pimm, et al., Iodine-131 and indium-111 labelled avidin and streptavidin for pre-targeted immunoscintigraphy with biotinylated anti-tumour monoclonal antibody, *Nucl. Med. Commun.* 9 (11) (1988) 931–941.
- [137] H.P. Kalofonos, et al., Imaging of tumor in patients with indium-111-labeled biotin and streptavidin-conjugated antibodies: preliminary communication, *J. Nucl. Med.* 31 (11) (1990) 1791–1796.
- [138] G. Paganelli, et al., Two-step tumour targeting in ovarian cancer patients using biotinylated monoclonal antibodies and radioactive streptavidin, *Eur. J. Nucl. Med.* 19 (5) (1992) 322–329.
- [139] M. Ruscowski, et al., Effect of endogenous biotin on the applications of streptavidin and biotin in mice, *Nucl. Med. Biol.* 24 (3) (1997) 263–268.
- [140] R.M. Sharkey, et al., Development of a streptavidin-anti-carcinoembryonic antigen antibody, radiolabeled biotin pretargeting method for radioimmunotherapy of colorectal cancer. Studies in a human colon cancer xenograft model, *Bioconjug Chem* 8 (4) (1997) 595–604.
- [141] S. Prakash, et al., Biotinidase resistant (68)Gallium-radioligand Based on biotin/avidin Interaction for pretargeting: Synthesis and preclinical evaluation, *Bioconjug Chem* 27 (11) (2016) 2780–2790.
- [142] C. Bailly, et al., Pretargeting for imaging and therapy in oncological nuclear medicine, *EJNMMI Radiopharmacy and Chemistry* 2 (1) (2017) 6, 2017. 2(1): p. 6.
- [143] G. Paganelli, et al., Intraperitoneal radio-localization of tumors pre-targeted by biotinylated monoclonal antibodies, *Int. J. Canc.* 45 (6) (1990) 1184–1189.
- [144] P. Casalini, et al., Tumor pretargeting: role of avidin/streptavidin on monoclonal antibody internalization, *J. Nucl. Med.* 38 (9) (1997) 1378–1381.
- [145] G. Paganelli, et al., Three-step monoclonal antibody tumor targeting in carcinoembryonic antigen-positive patients, *Canc. Res.* 51 (21) (1991) 5960–5966.
- [146] H. Kobayashi, et al., Improved clearance of radiolabeled biotinylated monoclonal antibody following the infusion of avidin as a "chase" without decreased accumulation in the target tumor, *J. Nucl. Med.* 35 (10) (1994) 1677–1684.
- [147] J.R. Newton-Northup, et al., Bifunctional phage-based pretargeted imaging of human prostate carcinoma, *Nucl. Med. Biol.* 36 (7) (2009) 789–800.
- [148] C. Dong, et al., SPECT/NIRF dual modality Imaging for Detection of intraperitoneal colon Tumor with an avidin/biotin pretargeting system, *Sci. Rep.* 6 (2016) 18905.
- [149] D.M. Goldenberg, et al., Cancer imaging and therapy with bispecific antibody pretargeting, *Update Canc. Therapeut.* 2 (1) (2007) 19–31.
- [150] M. Gargaud, et al., *Encyclopedia of Astrobiology*, Springer, 2011.
- [151] E.S. Bos, et al., In vitro evaluation of DNA-DNA hybridization as a two-step approach in radioimmunotherapy of cancer, *Canc. Res.* 54 (13) (1994) 3479–3486.
- [152] P. Dash, et al., Selective elimination of mRNAs in vivo: complementary oligodeoxynucleotides promote RNA degradation by an RNase H-like activity, *Proc. Natl. Acad. Sci. U. S. A.* 84 (22) (1987) 7896–7900.
- [153] E. Wickstrom, Oligodeoxynucleotide stability in subcellular extracts and culture media, *J. Biochem. Biophys. Methods* 13 (2) (1986) 97–102.
- [154] C. Cazenave, et al., Enzymatic amplification of translation inhibition of rabbit beta-globin mRNA mediated by anti-messenger oligodeoxynucleotides covalently linked to intercalating agents, *Nucleic Acids Res.* 15 (12) (1987) 4717–4736.
- [155] X. Li, et al., Novel DNA Polymer for amplification pretargeting, *ACS Med. Chem. Lett.* 6 (9) (2015) 972–976.

- [156] A. Amantana, P.L. Iversen, Pharmacokinetics and biodistribution of phosphorodiamidate morpholino antisense oligomers, *Curr. Opin. Pharmacol.* 5 (5) (2005) 550–555.
- [157] A. Ray, B. Norden, Peptide nucleic acid (PNA): its medical and biotechnical applications and promise for the future, *Faseb. J.* 14 (9) (2000) 1041–1060.
- [158] G. Liu, et al., Tumor pretargeting in mice using (99m)Tc-labeled morpholino, a DNA analog, *J. Nucl. Med.* 43 (3) (2002) 384–391.
- [159] G. Liu, et al., Human islet cell MORF/cMORF pretargeting in a xenogeneic murine transplant model, *Mol. Pharm.* 8 (3) (2011) 767–773.
- [160] J. He, et al., Affinity enhancement pretargeting: synthesis and testing of a 99mTc-labeled bivalent MORF, *Mol. Pharm.* 7 (4) (2010) 1118–1124.
- [161] G. Liu, et al., Investigations of 99mTc morpholino pretargeting in mice, *Nucl. Med. Commun.* 24 (6) (2003) 697–705.
- [162] G. Liu, et al., Replacing 99mTc with 111In improves MORF/cMORF pretargeting by reducing intestinal accumulation, *Mol. Imag. Biol.* 11 (5) (2009) 303–307.
- [163] G. Liu, et al., An experimental and theoretical evaluation of the influence of pretargeting antibody on the tumor accumulation of effector, *Mol. Canc. Therapeut.* 7 (5) (2008) 1025–1032.
- [164] J. He, et al., Amplification targeting: a modified pretargeting approach with potential for signal amplification-proof of a concept, *J. Nucl. Med.* 45 (6) (2004) 1087–1095.
- [165] Y. Wang, et al., Pretargeting with amplification using polymeric peptide nucleic acid, *Bioconjug Chem* 12 (5) (2001) 807–816.
- [166] G. Liu, et al., 90Y labeled phosphorodiamidate morpholino oligomer for pretargeting radiotherapy, *Bioconjug Chem* 22 (12) (2011) 2539–2545.
- [167] G. Liu, et al., A preclinical 188Re tumor therapeutic investigation using MORF/cMORF pretargeting and an antiTAG-72 antibody CC49, *Canc. Biol. Ther.* 10 (8) (2010) 767–774.
- [168] M. Rusckowski, et al., Pretargeting using peptide nucleic acid, *Cancer* 80 (12 Suppl) (1997) 2699–2705.
- [169] A. Leonidova, et al., In vivo demonstration of an active tumor pretargeting approach with peptide nucleic acid bioconjugates as complementary system, *Chem. Sci.* 5 (2015) 5601–5616.
- [170] M. Altai, et al., Evaluation of affibody molecule-based PNA-mediated radio-nuclide pretargeting: development of an optimized conjugation protocol and (177)Lu labeling, *Nucl. Med. Biol.* 54 (2017) 1–9.
- [171] M. Schubert, et al., Novel tumor pretargeting system based on complementary 1-configured oligonucleotides, *Bioconjug Chem* 28 (4) (2017) 1176–1188.
- [172] E. Saxon, C.R. Bertozzi, Cell surface engineering by a modified Staudinger reaction, *Science* 287 (5460) (2000) 2007–2010.
- [173] E. Saxon, J.I. Armstrong, C.R. Bertozzi, A “traceless” Staudinger ligation for the chemoselective synthesis of amide bonds, *Org. Lett.* 2 (14) (2000) 2141–2143.
- [174] B.L. Nilsson, L.L. Kiessling, R.T. Raines, Staudinger ligation: a peptide from a thioester and azide, *Org. Lett.* 2 (13) (2000) 1939–1941.
- [175] C.S. McKay, J. Moran, J.P. Pezacki, Nitrones as dipoles for rapid strain-promoted 1,3-dipolar cycloadditions with cyclooctynes, *Chem Commun (Camb)* 46 (6) (2010) 931–933.
- [176] N.J. Agard, J.A. Prescher, C.R. Bertozzi, A strain-promoted [3 + 2] azide-alkyne cycloaddition for covalent modification of biomolecules in living systems, *J. Am. Chem. Soc.* 126 (46) (2004) 15046–15047.
- [177] M.L. Blackman, M. Royzen, J.M. Fox, Tetrazine ligation: fast bioconjugation based on inverse-electron-demand Diels-Alder reactivity, *J. Am. Chem. Soc.* 130 (41) (2008) 13518–13519.
- [178] S.S. van Berkel, M.B. van Eldijk, J.C. van Hest, Staudinger ligation as a method for bioconjugation, *Angew Chem. Int. Ed. Engl.* 50 (38) (2011) 8806–8827.
- [179] H.C. Kolb, M.G. Finn, K.B. Sharpless, Click chemistry: diverse chemical function from a few good reactions, *Angew Chem. Int. Ed. Engl.* 40 (11) (2001) 2004–2021.
- [180] C.W. Tornøe, C. Christensen, M. Meldal, Peptidotriazoles on solid phase: [1,2,3]-triazoles by regioselective copper(i)-catalyzed 1,3-dipolar cycloadditions of terminal alkynes to azides, *J. Org. Chem.* 67 (9) (2002) 3057–3064.
- [181] R. Huisgen, 1,3-Dipolar cycloadditions. Past and future, *Angew Chem. Int. Ed. Engl.* 2 (1963) 565–598.
- [182] V.V. Rostovtsev, et al., A stepwise Huisgen cycloaddition process: copper(I)-catalyzed regioselective “ligation” of azides and terminal alkynes, *Angew Chem. Int. Ed. Engl.* 41 (14) (2002) 2596–2599.
- [183] L. Carroll, et al., Bioorthogonal chemistry for pre-targeted molecular imaging—progress and prospects, *Org. Biomol. Chem.* 11 (35) (2013) 5772–5781.
- [184] Z. Li, T.S. Seo, J. Jingyue Ju, 1,3-Dipolar cycloaddition of azides with electron-deficient alkynes under mild condition in water, *Tetrahedron Lett.* 45 (2004) 3143–3146.
- [185] G. Wittig, A. K. Zur existenz niedergliedriger cycloalkine, *Chem. Ber.* 94 (1961) 3260–3275.
- [186] J.M. Baskin, et al., Copper-free click chemistry for dynamic in vivo imaging, *Proc. Natl. Acad. Sci. U. S. A.* 104 (43) (2007) 16793–16797.
- [187] S.T. Laughlin, et al., In vivo imaging of membrane-associated glycans in developing zebrafish, *Science* 320 (5876) (2008) 664–667.
- [188] P.V. Chang, et al., Copper-free click chemistry in living animals, *Proc. Natl. Acad. Sci. U. S. A.* 107 (5) (2010) 1821–1826.
- [189] J.A. Codelli, et al., Second-generation difluorinated cyclooctynes for copper-free click chemistry, *J. Am. Chem. Soc.* 130 (34) (2008) 11486–11493.
- [190] X. Ning, et al., Visualizing metabolically labeled glycoconjugates of living cells by copper-free and fast Huisgen cycloadditions, *Angew Chem. Int. Ed. Engl.* 47 (12) (2008) 2253–2255.
- [191] M.F. Debets, et al., Aza-dibenzocyclooctynes for fast and efficient enzyme PEGylation via copper-free (3+2) cycloaddition, *Chem Commun (Camb)* 46 (1) (2010) 97–99.
- [192] J.C. Jewett, E.M. Sletten, C.R. Bertozzi, Rapid Cu-free click chemistry with readily synthesized biarylazacyclooctynes, *J. Am. Chem. Soc.* 132 (11) (2010) 3688–3690.
- [193] M. Chigrinova, et al., Rearrangements and addition reactions of biarylazacyclooctynes and the implications to copper-free click chemistry, *Org. Biomol. Chem.* 11 (21) (2013) 3436–3441.
- [194] S.M. van den Bosch, et al., Evaluation of strained alkynes for Cu-free click reaction in live mice, *Nucl. Med. Biol.* 40 (3) (2013) 415–423.
- [195] B. Amgarten, et al., Collagen labelling with an azide-proline chemical reporter in live cells, *Chem Commun (Camb)* 51 (25) (2015) 5250–5252.
- [196] K.M. Au, et al., Bespoke pretargeted nanoradioimmunotherapy for the treatment of non-hodgkin lymphoma, *ACS Nano* 12 (2) (2018) 1544–1563.
- [197] R.D. Row, J.A. Prescher, Tetrazine marks the spot, *ACS Cent. Sci.* 2 (8) (2016) 493–494.
- [198] B.L. Oliveira, Z. Guo, G.J.L. Bernardes, Inverse electron demand Diels-Alder reactions in chemical biology, *Chem. Soc. Rev.* 46 (16) (2017) 4895–4950.
- [199] S. Mayer, K. Lang, Tetrazines in inverse-electron-demand diels-alder Cyclo-additions and their Use in biology, *Synthesis-Stuttgart* 49 (4) (2017) 830–848.
- [200] A. Darko, et al., Conformationally Strained trans-Cyclooctene with improved Stability and excellent Reactivity in tetrazine ligation, *Chem. Sci.* 5 (10) (2014) 3770–3776.
- [201] A. Meier, J. Sauer, Donor-akzeptor substituierte dienophile bei diels-alder-reaktionen mit inversem elektronenbedarf, *Tetrahedron Lett.* 31 (47) (1990) 6855–6858.
- [202] Y. Fang, et al., Photochemical syntheses, transformations, and bioorthogonal chemistry of trans-cycloheptene and silyl trans-cycloheptene Ag(i) complexes, *Chem. Sci.* 9 (7) (2018) 1953–1963.
- [203] O. Diels, E. Alder, Synthesen in der hydroaromatischen Reihe, *Justus Liebigs Ann. Chem.* 460 (1928) 98–122.
- [204] J. Sauer, R. Sustmann, Mechanistic aspects of diels-alder reactions: a critical survey, *Angew Chem. Int. Ed. Engl.* 19 (10) (1980) 779–807.
- [205] J. Sauer, et al., 1,2,4,5-Tetrazine: Synthesis and Reactivity in [4+2] cycloadditions, *Eur. J. Org. Chem.* 12 (1998) 2885–2896.
- [206] D.L. Boger, R.P. Schaum, R.M. Garbaccio, Regioselective inverse electron demand diels-alder reactions of N-Acyl 6-Amino-3-(methylthio)-1,2,4,5-tetrazines, *J. Org. Chem.* 63 (18) (1998) 6329–6337.
- [207] D. Svatunek, C. Denk, H. Mikula, A computational model to predict the Diels-Alder reactivity of aryl/alkyl-substituted tetrazines. *Monatshefte für Chemie - Chemical Monthly*, 2017, pp. 1–5.
- [208] J.P. Meyer, et al., Exploring structural parameters for pretargeting radio-ligand optimization, *J. Med. Chem.* 60 (19) (2017) 8201–8217.
- [209] Y. Liang, et al., Control and design of mutual orthogonality in bioorthogonal cycloadditions, *J. Am. Chem. Soc.* 134 (43) (2012) 17904–17907.
- [210] M.T. Taylor, et al., Design and synthesis of highly reactive dienophiles for the tetrazine-trans-cyclooctene ligation, *J. Am. Chem. Soc.* 133 (25) (2011) 9646–9649.
- [211] K. Lang, et al., Genetic Encoding of bicyclonynes and trans-cyclooctenes for site-specific protein labeling in vitro and in live mammalian cells via rapid fluorogenic Diels-Alder reactions, *J. Am. Chem. Soc.* 134 (25) (2012) 10317–10320.
- [212] A. Pinner, Ueber die Einwirkung von Hydrazin auf Imidoäther, *Eur. J. Org. Chem.* 297 (3) (1897) 221–271.
- [213] J. Yang, et al., Metal-catalyzed one-pot synthesis of tetrazines directly from aliphatic nitriles and hydrazine, *Angew Chem. Int. Ed. Engl.* 51 (21) (2012) 5222–5225.
- [214] P. Audebert, et al., Synthesis of new substituted tetrazines: electrochemical and spectroscopic properties, *New J. Chem.* 28 (2004) 387–392.
- [215] D.S. Liu, et al., Diels-Alder cycloaddition for fluorophore targeting to specific proteins inside living cells, *J Am Chem Soc* 134 (2) (2012) 792–795.
- [216] M.M. Herth, et al., Development of a (11)C-labeled tetrazine for rapid tetrazine-trans-cyclooctene ligation, *Chem Commun (Camb)* 49 (36) (2013) 3805–3807.
- [217] R. Selvaraj, J.M. Fox, An efficient and mild oxidant for the synthesis of s-tetrazines, *Tetrahedron Lett.* 55 (34) (2014) 4795–4797.
- [218] W. Chen, et al., Clicking 1,2,4,5-tetrazine and cyclooctynes with tunable reaction rates, *Chem Commun (Camb)* 48 (12) (2012) 1736–1738.
- [219] H.S. Beckmann, et al., Preparation of carbohydrate arrays by using Diels-Alder reactions with inverse electron demand, *Chemistry* 18 (21) (2012) 6548–6554.
- [220] M. Royzen, G.P. Yap, J.M. Fox, A photochemical synthesis of functionalized trans-cyclooctenes driven by metal complexation, *J. Am. Chem. Soc.* 130 (12) (2008) 3760–3761.
- [221] N.K. Devaraj, R. Weissleder, S.A. Hilderbrand, Tetrazine-based cycloadditions: application to pretargeted live cell imaging, *Bioconjug Chem* 19 (12) (2008) 2297–2299.
- [222] C.L. Vogel, et al., Efficacy and safety of trastuzumab as a single agent in first-line treatment of HER2-overexpressing metastatic breast cancer, *J. Clin. Oncol.* 20 (3) (2002) 719–726.

- [223] L. Wyffels, et al., In vivo evaluation of (18)F-labeled TCO for pre-targeted PET imaging in the brain, *Nucl. Med. Biol.* 41 (6) (2014) 513–523.
- [224] Z. Li, et al., Tetrazine–trans-cyclooctene ligation for the rapid construction of 18F labeled probes, *Chem Commun (Camb)* 46 (42) (2010) 8043–8045.
- [225] B.M. Zeglis, et al., Optimization of a pretargeted strategy for the PET imaging of colorectal carcinoma via the modulation of radioligand pharmacokinetics, *Mol. Pharm.* 12 (10) (2015) 3575–3587.
- [226] J.P. Meyer, et al., (18)F-Based pretargeted PET imaging Based on bio-orthogonal diels-alder click chemistry, *Bioconjug Chem* 27 (2) (2016) 298–301.
- [227] F. Thalhammer, U. Wallfahrere, J. Sauer, Reaktivität einfacher offenkettiger und cyclischer dienophile bei Diels-Alder-reaktionen mit inversem elektronenbedarf, *Tetrahedron Lett.* 31 (47) (1990) 6851–6854, 31(47): pp. 6851–6854.
- [228] H.B. Breitz, et al., Clinical optimization of pretargeted radioimmunotherapy with antibody–streptavidin conjugate and 90Y-DOTA-biotin, *J. Nucl. Med.* 41 (1) (2000) 131–140.
- [229] B.M. Zeglis, et al., A pretargeted PET imaging strategy based on bio-orthogonal Diels-Alder click chemistry, *J. Nucl. Med.* 54 (8) (2013) 1389–1396.
- [230] C. Denk, et al., Design, synthesis, and Evaluation of a low-molecular-weight (11)C-labeled Tetrazine for pretargeted PET imaging applying Bioorthogonal in vivo click chemistry, *Bioconjug Chem* 27 (7) (2016) 1707–1712.
- [231] M.E. Ackerman, et al., A33 antigen displays persistent surface expression, *Cancer Immunol. Immunother.* 57 (7) (2008) 1017–1027.
- [232] H.L. Evans, et al., Bioorthogonal chemistry for (68) Ga radiolabelling of DOTA-containing compounds, *J. Labelled Comp Radiopharm* 57 (4) (2014) 291–297.
- [233] J. Steen, et al., Preliminary in vivo evaluation of a 11C-labeled tetrazine for bioorthogonal reaction within CNS, *J. Nucl. Med.* 57 (2016) 1051.
- [234] L. Cai, S. Lu, V.W. Pike, Chemistry with [18F]Fluoride ion, *Eur. J. Org. Chem.* 17 (2008) 2853–2873.
- [235] O. Keinanen, et al., A new highly reactive and low lipophilicity Fluorine-18 labeled tetrazine Derivative for pretargeted PET imaging, *ACS Med. Chem. Lett.* 7 (1) (2016) 62–66.
- [236] L.M. Bimbo, et al., Biocompatibility of thermally hydrocarbonized porous silicon nanoparticles and their biodistribution in rats, *ACS Nano* 4 (6) (2010) 3023–3032.
- [237] Y. Humblet, Cetuximab: an IgG(1) monoclonal antibody for the treatment of epidermal growth factor receptor-expressing tumours, *Expet Opin. Pharmacother.* 5 (7) (2004) 1621–1633.
- [238] O. Keinanen, et al., Pretargeting of internalizing trastuzumab and cetuximab with a (18)F-tetrazine tracer in xenograft models, *EJNMMI Res.* 7 (1) (2017) 95.
- [239] R.B. Martin, Ternary complexes of Al³⁺ and F[−] with a third ligand, *Coord. Chem. Rev.* 149 (1996) 23–32.
- [240] W.J. McBride, R.M. Sharkey, D.M. Goldenberg, Radiofluorination using aluminum-fluoride (Al¹⁸F), *EJNMMI Res.* 3 (1) (2013) 36.
- [241] F. Cleeren, et al., New chelators for low temperature Al(18)F-Labeling of biomolecules, *Bioconjug Chem* 27 (3) (2016) 790–798.
- [242] N.K. Devaraj, et al., Reactive polymer enables efficient in vivo bioorthogonal chemistry, *Proc. Natl. Acad. Sci. U. S. A.* 109 (13) (2012) 4762–4767.
- [243] B. Nichols, et al., 68Ga chelating bioorthogonal tetrazine polymers for the multistep labeling of cancer biomarkers, *Chem Commun (Camb)* 50 (40) (2014) 5215–5217.
- [244] F. Zoller, et al., Endoradiotherapy in cancer treatment—basic concepts and future trends, *Eur. J. Pharmacol.* 625 (1–3) (2009) 55–62.
- [245] J.P. Pouget, et al., Clinical radioimmunotherapy—the role of radiobiology, *Nat. Rev. Clin. Oncol.* 8 (12) (2011) 720–734.
- [246] S.M. Larson, et al., Radioimmunotherapy of human tumours, *Nat. Rev. Canc.* 15 (6) (2015) 347–360.
- [247] R.M. Reilly, Radioimmunotherapy of solid tumors: the promise of pre-targeting strategies using bispecific antibodies and radiolabeled haptens, *J. Nucl. Med.* 47 (2) (2006) 196–199.
- [248] R.P. Baum, *Therapeutic Nuclear Medicine*, Springer, 2014.
- [249] A.J. Worth, R.M. Zuber, M. Hocking, Radioiodide (131I) therapy for the treatment of canine thyroid carcinoma, *Aust. Vet. J.* 83 (4) (2005) 208–214.
- [250] C.L. Wright, et al., Theranostic imaging of Yttrium-90, *BioMed Res. Int.* 2015 (2015) 481279.
- [251] IAEA, Yttrium-90 and Rhenium-188 Radiopharmaceuticals for Radionuclide Therapy, International Atomic Energy Agency, 2015.
- [252] K. Yong, M.W. Brechbiel, Towards translation of 212Pb as a clinical therapeutic; getting the lead in!, *Dalton Trans.* 40 (23) (2011) 6068–6076.
- [253] F. Kraeber-Bodere, et al., Targeting, toxicity, and efficacy of 2-step, pretargeted radioimmunotherapy using a chimeric bispecific antibody and 131I-labeled bivalent hapten in a phase I optimization clinical trial, *J. Nucl. Med.* 47 (2) (2006) 247–255.
- [254] F. Kraeber-Bodere, et al., Pretargeted radioimmunotherapy (pRAIT) in medullary thyroid cancer (MTC), *Tumour Biol* 33 (3) (2012) 601–606.
- [255] S.H. Frost, H. Jensen, S. Lindgren, In vitro evaluation of avidin antibody pretargeting using 211At-labeled and biotinylated poly-L-lysine as effector molecule, *Cancer* 116 (4 Suppl) (2010) 1101–1110.
- [256] S. Lindgren, et al., Synthesis and biodistribution of 211At-labeled, biotinylated, and charge-modified poly-L-lysine: evaluation for use as an effector molecule in pretargeted intraperitoneal tumor therapy, *Bioconjug Chem* 13 (3) (2002) 502–509.
- [257] S. Lindgren, et al., (211)At-labeled and biotinylated effector molecules for pretargeted radioimmunotherapy using poly-L- and poly-D-lysine as multicarriers, *Clin. Canc. Res.* 9 (10 Pt 2) (2003) 3873S, 9S.
- [258] A. Gustafsson-Lutz, et al., Therapeutic efficacy of alpha-radioimmunotherapy with different activity levels of the (213)Bi-labeled monoclonal antibody MX35 in an ovarian cancer model, *EJNMMI Res.* 7 (1) (2017) 38.
- [259] T. Lappchen, et al., DOTA-tetrazine probes with modified linkers for tumor pretargeting, *Nucl. Med. Biol.* 55 (2017) 19–26.
- [260] M.R. Lewis, et al., Biological comparison of 149Pm-, 166Ho-, and 177Lu-DOTA-biotin pretargeted by CC49 scFv-streptavidin fusion protein in xenograft-bearing nude mice, *Nucl. Med. Biol.* 31 (2) (2004) 213–223.
- [261] J.L. Houghton, et al., Establishment of the in vivo efficacy of pretargeted radioimmunotherapy utilizing inverse electron demand diels-alder click chemistry, *Mol. Canc. Therapeut.* 16 (1) (2017) 124–133.
- [262] S. Vallabhajosula, et al., Radioimmunotherapy of metastatic prostate cancer with (177)Lu-DOTA-hu591 anti prostate specific membrane antigen specific monoclonal antibody, *Curr. Rad.* 9 (1) (2016) 44–53.
- [263] F. Forrer, et al., Is there need for radioimmunotherapy? results of a phase I/II study in patients with indolent B-cell lymphomas using lutetium-177-DOTA-rituximab, *Q. J. Nucl. Med. Mol. Imaging* 56 (6) (2012) 544–550.
- [264] M. Bourgeois, et al., Radioimmunotherapy for treating cancer: recent advances and current opportunities, *Expet Opin. Biol. Ther.* 17 (7) (2017) 813–819.
- [265] K. Fujiki, et al., A one-pot three-component double-click Method for Synthesis of [(67)Cu]-Labeled biomolecular radiotherapeutics, *Sci. Rep.* 7 (1) (2017) 1912.
- [266] H.A. Wieder, et al., Clinical use of bone-targeting radiopharmaceuticals with focus on alpha-emitters, *World J. Radiol.* 6 (7) (2014) 480–485.
- [267] C. Kratochwil, et al., Targeted Alpha Therapy of mCRPC with (225)Actinium-PSMA-617: swimmer-Plot analysis suggests efficacy regarding duration of tumor-control, *J. Nucl. Med.* 59 (5) (2018) 795–802.
- [268] P.E. Edem, et al., In vivo radionuclide generators for diagnostics and therapy, *Bioinorgan. Chem. Appl.* 2016 (2016) 6148357.
- [269] M.A. Shah, et al., Metal-free cycloaddition chemistry driven pretargeted radioimmunotherapy Using alpha-Particle radiation, *Bioconjug Chem* 28 (12) (2017) 3007–3015.
- [270] S.M. van Duijnhoven, et al., Diabody pretargeting with click chemistry in vivo, *J. Nucl. Med.* 56 (9) (2015) 1422–1428.
- [271] A. Yordanova, et al., Theranostics in nuclear medicine practice, *OncoTargets Ther.* 10 (2017) 4821–4828.
- [272] R.A. Werner, et al., 68Gallium- and 90Yttrium-177Lutetium: "theranostic twins" for diagnosis and treatment of NETs, *Ann. Nucl. Med.* 29 (1) (2015) 1–7.
- [273] F. Rösch, H.R. Herzog, S.M. Qaim, The beginning and development of the theranostic approach in nuclear medicine, as exemplified by the radionuclide pair 86Y and 90Y, *Pharmaceuticals* 10 (2) (2017) 56.
- [274] U. Haberkorn, et al., Future trends in prostate cancer theranostics with PSMA ligands, *Clin Transl Imaging* 4 (2016) 487–489.
- [275] K.O. Mang'era, et al., Initial investigations of 99mTc-labeled morpholinos for radiopharmaceutical applications, *Eur. J. Nucl. Med.* 28 (11) (2001) 1682–1689.
- [276] D.M. Patterson, L.A. Nazarova, J.A. Prescher, Finding the right (bioorthogonal) chemistry, *ACS Chem. Biol.* 9 (3) (2014) 592–605.
- [277] T.A. Aweda, et al., Rates and equilibria for probe capture by an antibody with infinite affinity, *Bioconjug Chem* 21 (4) (2010) 784–791.
- [278] R. Karlsson, A. Michaelsson, L. Mattsson, Kinetic analysis of monoclonal antibody-antigen interactions with a new biosensor based analytical system, *J. Immunol. Meth.* 145 (1–2) (1991) 229–240.
- [279] K.D. Orcutt, et al., Engineering an antibody with picomolar affinity to DOTA chelates of multiple radionuclides for pretargeted radioimmunotherapy and imaging, *Nucl. Med. Biol.* 38 (2) (2011) 223–233.
- [280] W.J. McBride, et al., A novel method of 18F radiolabeling for PET, *J. Nucl. Med.* 50 (6) (2009) 991–998.
- [281] J.C. Jewett, C.R. Bertozzi, Cu-free click cycloaddition reactions in chemical biology, *Chem. Soc. Rev.* 39 (4) (2010) 1272–1279.
- [282] N.K. Devaraj, et al., Bioorthogonal turn-on probes for imaging small molecules inside living cells, *Angew Chem. Int. Ed. Engl.* 49 (16) (2010) 2869–2872.
- [283] K.S. Yang, et al., Bioorthogonal approach to identify unsuspected drug targets in live cells, *Angew Chem. Int. Ed. Engl.* 52 (40) (2013) 10593–10597.
- [284] M.R. Karver, R. Weissleder, S.A. Hilderbrand, Bioorthogonal reaction pairs enable simultaneous, selective, multi-target imaging, *Angew Chem. Int. Ed. Engl.* 51 (4) (2012) 920–922.
- [285] L.G. Meimetis, et al., Ultrafluorogenic coumarin-tetrazine probes for real-time biological imaging, *Angew Chem. Int. Ed. Engl.* 53 (29) (2014) 7531–7534.
- [286] J.C. Carlson, et al., BODIPY-tetrazine derivatives as superbright bioorthogonal turn-on probes, *Angew Chem. Int. Ed. Engl.* 52 (27) (2013) 6917–6920.
- [287] G. Budin, et al., Bioorthogonal probes for polo-like kinase 1 imaging and quantification, *Angew Chem. Int. Ed. Engl.* 50 (40) (2011) 9378–9381.
- [288] H.J. Chung, et al., Ubiquitous detection of gram-positive bacteria with bio-orthogonal magnetofluorescent nanoparticles, *ACS Nano* 5 (11) (2011) 8834–8841.